**Optimization of Synthetic High-Density Lipoprotein Nanostructures
for Treatment of Inflammatory Diseases**

by

Sang Yeop Kim

A dissertation submitted in partial fulfillment
of the requirements for the degree of
Doctor of Philosophy
(Pharmaceutical Sciences)
in the University of Michigan
2019

Doctoral Committee:

Associate Professor Anna Schwendeman, Chair
Associate Professor James J. Moon
Professor Theodore J. Standiford
Professor Kathleen Stringer
Professor Duxin Sun

Sang Yeop Kim

kimsangy@umich.edu

ORCID iD: 0000-0002-5781-9039

Dedication

To my parents and to many friends

Without their support, this wouldn't have been possible

Acknowledgments

I would first like to thank my thesis advisor Anna Schwendeman, associate professor of the Pharmaceutical Sciences Department, College of Pharmacy at the University of Michigan. I am very fortunate and thankful to have had a great advisor over the past 5 years of graduate school. She has been very supportive of my career goals and has provided me with extensive personal and professional guidance to be a successful individual and scientist. She is the greatest advisor and mentor who has taught me a great deal about both science and life in general. I would also like to thank the rest of my committee Dr. James Moon, Dr. Theodore Standiford, Dr. Kathleen Stringer, and Dr. Duxin Sun who have given me great advice and guidance on my research.

I cannot imagine my 5 years of graduate school life without my amazing friends and colleagues in both Schwendeman labs; Dr. Jay Kang, Dr. Emily Morin, Maria Fawaz, Jenna Walker, Dr. Jia Zhou, Dr. Dan Li, Alex Benet, Minzhi Yu, Lindsay Scheetz, Dr. Jie Tang, Dr. Wenmin Yuan, Jason Albert, Justin Hong, Dr. Yayuan Liu, Dr. Lin Mei, Dr. Hongliang He, Dr. Lisha Liu, Dr. Avital Beig, Dr. Gergely Lautner, Dr. Nianqiu Shi, Dr. Rae Sung Chang, Dr. Morgan Giles, Dr. Max Mazzara, Kristen Hong, Jill Coghlan, Troy Halseth, Richard Schutzman, and Ziyun Xia. I had a pleasure working and playing with them. I would especially like to thank Dr. Wenmin Yuan for her awesome mentorship, Dr. Emily Morin for great biology discussions, and Jay Kang for our mutual support and reliance on each other in surviving graduate school. Also, my research would not have gone as smoothly without great help and support from Rose Ackermann and Karl Olsen.

I am grateful to have wonderful friends in Ann Arbor. I would like to thank Jay Kang, Yunsu Na, Kwangwoo Jeong, Sunghoon Hur, Jeonghyo Lee, Youngmin Kang, Jooae Cheon, Minwoo Hwang, Caroline Kim, Daniel Yang, David Lee, and Jihyang Gwak. They have made my time in Ann Arbor very special and unforgettable. I would also like to thank my old San Diego friends, Bongju Oh, Jin Oh, Steve Lee, Yonghee Lee, and Jin Chae for supporting me.

Finally, and foremost, I cannot express enough appreciation to my parents, Yungwon and Changkyung, and my sister Elaine. Although they are far away, they have constantly supported and encouraged me throughout my graduate school career. Thank you for helping me to shape my life with positivity and passion. Thank you for supporting and encouraging me whenever I went through struggle and pain. And thank you for providing unconditional love.

Table of Contents

List of Tables

x

Abstract

Biomimetic synthetic high-density lipoproteins (sHDLs) are nanoparticles that mimic the physical, chemical, and biological activity of endogenous HDL. A number of sHDL products have been investigated for the treatment of cardiovascular diseases (CVD) for the past three decades. sHDL is composed of apolipoprotein A-I (apoA-I) or apoA-I mimetic peptide complexed with phospholipids to form a discoidal nanoparticle. Infusions of sHDL in animals and humans have been shown to increase circulating HDL levels, improve plasma cholesterol efflux capacity, inhibit inflammation, and improve endothelial function. Phospholipid composition of sHDL appears to have a significant impact on its function by defining the plasma stability of and cholesterol and LPS binding to the nanoparticle. Thus, we proposed to optimize sHDL phospholipid composition to tailor nanoparticle functionality toward a specific therapeutic indication, such as atherosclerosis and sepsis.

In the first chapter, we optimized sHDL for the treatment of sepsis by comparing different fluidities of sHDL based on various fatty acid chain lengths and saturation of phospholipid compositions (POPC, DMPC, DPPC, and DSPC). We hypothesized that sHDL with a fluid liquid crystalline phase would improve anti-inflammatory activities by accelerating the efflux of exogenous molecules and improving accessibility to phospholipids for potential signal transductions compared to sHDL in a rigid gel phase. We demonstrated that treating cells with 22A-DMPC, sHDL with a fluid liquid crystalline phase, resulted in the most effective inhibition of NF-κB signaling, TLR4 signaling through regulation of TLR4 recruitment into lipid rafts, and

upregulation of activating transcription factor 3 (ATF-3) expression *in vitro*. Furthermore, 22A-DMPC effectively reduced mortality and protected organs in mice challenged with lethal doses of lipopolysaccharide (LPS) in a model of sepsis. In conclusion, we demonstrated that differences in sHDL phospholipid composition can impact sHDL's anti-inflammatory signaling and the effectiveness of sepsis therapy.

In the second study, we determined how phospholipid and peptide components of sHDL impacted the nanoparticle's pharmacokinetic and pharmacodynamic properties. We synthesized two different sets of sHDL with either identical phospholipids with variable peptide sequences of different plasma stability or identical peptide sequences with variable fatty acid chain length and saturation. We observed that proteolytically stabilized 22A-P-sHDL increased nanoparticle half-life by 2-fold compared to less stable 22A-sHDL. Nevertheless, increased half-life did not translate to higher cholesterol mobilization. In contrast, varying phospholipids significantly impacted the nanoparticle's pharmacokinetic profile whereby 22A-DSPC sHDL resulted in the longest half-life (6.0 h) compared to 22A-POPC sHDL (1.0 h). In addition, due to its increased half-life, 22A-DSPC sHDL notably impacted the nanoparticle's cholesterol mobilization capability, resulting in a 6.5-fold increase compared to 22A-POPC sHDL. Thus, we observed that the phospholipid component of sHDL plays a critical role in cholesterol mobilization *in vivo*.

In the final study, we formulated a new biomimetic nanomicelle called MiNano that is structurally similar to sHDL with a hydrophobic core, a hydrophilic exterior, and a particle size of 12 – 14 nm. We discovered that MiNano resulted in a similar functionality to sHDL, but with much more efficient suppression of the inflammatory response *in vitro*. Also, MiNano displayed robust inhibition of inflammatory cytokines in an LPS-induced endotoxin mice model.

In summary, this thesis thoroughly investigates the importance of the phospholipid component of sHDL and MiNano in the regulation of inflammation and cholesterol mobilization, allowing us to optimize nanoparticle composition for the treatment of sepsis and atherosclerosis.

Chapter 1

Introduction

1.1.   High-Density Lipoprotein

High-density lipoprotein (HDL) or generally known as "good" cholesterol is the smallest and densest plasma lipoprotein that circulates the body through the blood to mainly absorb cholesterol and carries back to the liver for elimination or recycling to extrahepatic tissues. This role is known as reverse cholesterol transport (RCT) which is one of the well-established protective mechanism of HDL in atherosclerosis as HDL accepts effluxed cholesterol from overloaded macrophages within the plaques and remove it from circulation (1). Likewise, HDL can also act as an anti-inflammatory agent. HDL preferentially binds to and neutralizes circulating endotoxin, returning it to the liver for elimination (2,3). HDL also promotes cellular membrane cholesterol depletion, compromising lipid raft integrity and leading to reduced TLR4 expression on the cell surface (4). Furthermore, HDL induces activating transcription factor 3 (ATF3) to suppress the expression of TLR-induced pro-inflammatory cytokines (5–7).

In several clinical investigations, profound changes in the concentration and composition of HDL have been established such as in cardiovascular diseases (CVD), sepsis, and systemic lupus erythematosus (SLE). Low levels of plasma HDL are observed in CVD patients (8–10), sepsis patients (11–13), and SLE patients (14–19). In addition, the plasma HDL level shows an inverse correlation with a clinical endpoint of diseases. Therefore, HDL has been investigated as

a promising potential therapy against CVD and sepsis, especially synthetic HDL (sHDL) due to ease of manufacture.

1.2.   Structure and Composition of HDL

HDL is constantly remodeled in the bloodstream through interactions with other lipoproteins, enzymes, and contact with target cells, resulting in significant particle heterogeneity. HDL consists of a core of hydrophobic lipids, including cholesteryl esters and triglycerides, and a surface monolayer containing phospholipid, free cholesterol, and apolipoproteins. The newly synthesized HDL (nascent HDL) is characterized in a discoidal shape with small unilamellar bilayers surrounded by apoA-I monomers, range from 8 – 10 nm in diameter, and 4.4 nm in thickness (20–22). Two discoidal models have been proposed as shown in **Figure 1.1**. One is called the 'belt' model which apoA-I forms continuous amphipathic α-helices that are parallel to the plane of the disc (23) and other is called 'picket-fence' model which amphipathic α-helical repeats of apoA-I form tandem anti-parallel helixes that are perpendicular to the plane of the disc (24).
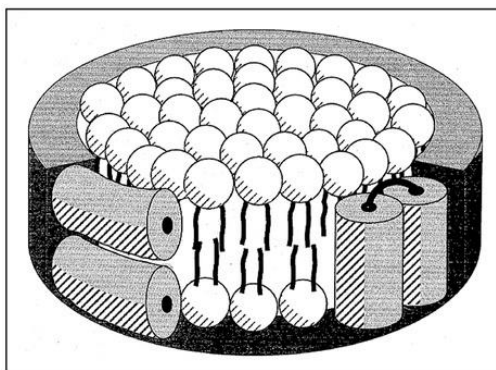
Figure 1.1. *Models of discoidal high-density lipoprotein. Possible orientations of amphipathic helixes relative to the edge of discoidal micelles formed between apolipoproteins and phospholipids. Left, belt model; right, picket fence model* (25)

HDL consists of a core of nonpolar polar lipid including cholesteryl ester (CE) and triglyceride (TG), surrounded by a surface monolayer of a phospholipid, free cholesterol, and apolipoproteins. Apolipoprotein A-I (apoA-I) is the most abundant protein associated with HDL, comprising 70% of the total HDL protein content (21). ApoA-I is a 28.1 kDa, highly α-helical and amphipathic scaffold protein consisting of 243 amino acids that interact with lipids to ultimately define the size and shape of HDL species (21). The amphipathic characteristic of apoA-I allows solubilization of lipoprotein complex and to interact with both hydrophobic and hydrophilic molecules. Therefore, it allows HDL to associate numerous metabolic processes that require interaction with other proteins and receptors, as well as transport and exchange of lipids, hormones, CE, and TG.

In addition to proteins, lipid species are another key component in HDL that provide the overall structure of HDL and serve as a substrate for many receptors and enzymes associated with HDL and its metabolic properties. More than half of the total HDL mass is accounted for by lipid components, the majority being phospholipids – accounting for 40-60% of the total lipid mass (26). Of these phospholipids, phosphatidylcholines (PC) are known to be the largest population of HDL lipids making up 33 – 45% of total lipids. These lipids play a critical role in particle stability, cholesterol efflux from macrophages, the ability to interact with lecithin cholesterol acyltransferase (LCAT), and cholesterol elimination (27–32).

HDL can be classified into different sub-populations using various techniques. An overview of HDL classification is summarized in **Table 1.1** based on the publication of Rosenson *et al.* (33). Briefly, the use of density gradient ultracentrifugation and nondenaturing gradient gel electrophoresis can distinguish HDL subpopulations on the basis of density and size, respectively; from smallest to largest, HDL3c, HDL3b, HDL3a, HDL2a, and HDL2b (33). ApoA-I containing

3

HDL subpopulations can also be defined on the basis of size and charge: pre-β-1 HDL (very small, discoidal HDL with apoA-I and phospholipid), α-4 HDL (very small, discoidal HDL with apoA-I, phospholipid, and free cholesterol), α-3 HDL (small, spherical HDL with apoA-I, apoA-II phospholipid, free cholesterol, cholesteryl ester, and triglyceride), α-2 HDL (medium-sized, spherical HDL with same constituents as α-3 HDL), and α-1 HDL (very large, spherical HDL with same constituents as α-3 HDL but nearly no apoA-II) (33). Using more sophisticated techniques, such as nuclear magnetic resonance (NMR), 26 different HDL subpopulations have been identified, but they are simply described as small, medium, and large due to limited measurement precision (33). Recently, an NMR-based clinical analyzer called the Vantera® was developed to measure total HDL particle number in clinical laboratory settings (34).

Table 1.1. Classification of HDL.

Separation	Analytical Method		Very Small	Small	Medium	Large	Very Large
Density	Ultracentrifugation	Classification	HDL3			HDL2	
		Range (F1.2)	0 - 3.5			3.5 - 9	
	Density gradient ultracentrifugation	Classification	HDL3c	HDL3b	HDL3a	HDL2a	HDL2b
		Range (g/mL)	1.15 - 1.17	1.13 - 1.15	1.11 - 1.13	1.09 - 1.11	1.06 - 1.09
Size	Nondenaturing gradient gel electrophoresis	Classification	HDL3c	HDL3b	HDL3a	HDL2a	HDL2b
		Range (nm)	7.2 - 7.8	7.8 - 8.2	8.2 - 8.8	8.8 - 9.7	9.7 - 12.9
	2-D gel electrophoresis	Classification	pre-β-1	α-4	α-3	α-2	α-1
		Range (nm)	5.0 - 6.0	7.0 -7.5	8.5 -8.5	9.0 - 9.4	10.8 - 11.2
	NMR	Classification	Small		Medium	Large	
		Range (nm)	7.3 - 8.2		8.2 - 9.4	9.4 - 14	

1.3. Biosynthesis of HDL

Biosynthesis of HDL initiates with apoA-I which is synthesized from hepatocytes and enterocytes of the liver and small intestine, respectively. ApoA-I is secreted in a lipid-poor form but readily sequesters phospholipids and free cholesterol. Acquisition of these molecular components results in nascent HDL that is wrapped with two antiparallel molecules of apoA-I in a belt-like fashion around a solubilized central core of phospholipid oriented as a bilayer (35–37). Nascent HDL is the smallest HDL which is mainly interdigitated in about 160 phospholipids present in the core of the disc (25). Nascent HDL is then matured through the interaction of apoA-I with ATP binding cassette receptor A1 (ABCA1), a transmembrane protein that mediates the transfer of phospholipids and free cholesterol to apoA-I. Free cholesterol transferred to HDL becomes esterified by LCAT. CE is then driven into the lipid bilayer, generating a core of hydrophobic CE surrounded by a monolayer of phospholipids. The transfer of CE into the core leads to the size increase of HDL that changes the disc-like structure into a maturing spherical structure while creating a gradient enabling more free cholesterol to move onto the particle surface. As HDL matures, it can interact with ATP-binding cassette receptor G1 (ABCG1) and scavenger receptor type B-1 (SR-BI) that participates in cellular cholesterol flux to HDL. Overall, the above processes increase the size of HDL and contribute to the heterogeneity of HDL (**Figure 1.2**).

preβ-1 HDL   **α-4 HDL**   **α-3 HDL**   **α-2 HDL**   **α-1 HDL**
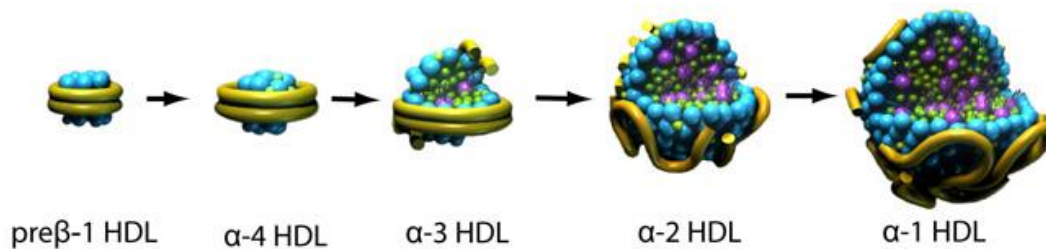
Figure 1.2. *Schematic representation of maturation of HDL* (38).

1.4. Biological Functions of HDL

HDL has been recognized with many biological functions including antioxidant, anti-inflammatory, endothelial cell maintenance functions, and RCT. For the purpose of the project, we specifically focused on RCT and the anti-inflammatory functions of HDL.

1.4.1. Reverse Cholesterol Transport

RCT allows translocating excess cholesterol and other lipids from lipid-laden macrophages in atherosclerotic lesions to the liver for elimination (**Figure 1.3**). This process is initiated by nascent HDL through interactions between apoA-I associated with HDL and ABCA1 on the peripheral cells (39). Free cholesterol and phospholipids are transferred from cells to nascent HDL, forming mature HDL particles (39). HDL further matures by esterifying cholesterol to CE by LCAT. LCAT catalyzes the esterification of free cholesterol associated with HDL and increases its hydrophobicity to maintain the concentration gradient of free cholesterol between cells and plasma to prevent net efflux of cholesterol from reaching equilibrium. The CE is then translocated within the hydrophobic core of HDL. Mature HDL particles can further remove cholesterol from peripheral cells through ABCG1 and SR-B1 (40,41). Cholesterol-rich HDL particles are then trafficked to the liver, delivering cholesterol cargo to hepatocytes through SR-BI in the apoA-I-dependent process. Finally, cholesterol is incorporated into bile and excreted in the feces. HDL can also transfer CE to low-density lipoprotein (LDL) in exchange for TG, a process favored by cholesteryl ester transfer protein (CETP). Cholesterol-loaded LDL is then taken up by hepatocytes through the LDL receptor, promoting reverse cholesterol transport. Removal of excess cholesterol from macrophages in the artery wall is recognized to be the key process of HDL for protection against atherosclerosis and improvement of cardiovascular outcomes (42).

6
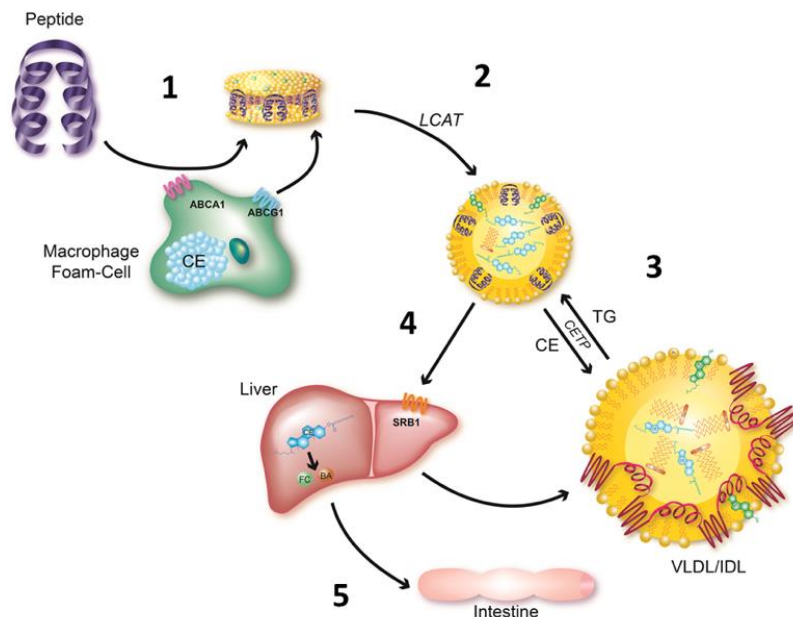
Figure 1.3. *Reverse Cholesterol Transport pathway. 1) Formation of discoidal nascent HDL, 2) Formation of cholesterol esters by LCAT,3) transfer of CE and TG between HDL and LDL/VLDL, 4) Delivery of cholesterol to the liver, and 5) Excretion of cholesterol into the bile* (43).

1.4.2. Anti-inflammatory Function

HDL exerts an array of anti-inflammatory activities through a number of mechanisms. HDL preferentially binds to and neutralizes circulating endotoxin, returning it to the liver for elimination (2,3). HDL also reduced TLR4 recruitment into lipid raft via cellular membrane cholesterol depletion (4). Furthermore, HDL induces activating transcription factor 3 (ATF3), a transcriptional modulator that act as a negative feedback on TLR signaling by inactivation target genes through reduction of histone acetylation, to modulate the TLR-induced pro-inflammatory cytokines, however, the exact mechanism remains unclear (5–7).

Microbial products such as lipopolysaccharides (LPS), an endotoxin component presented on the outer membrane of Gram-negative bacteria, are capable of triggering the inflammatory

response via Toll-like receptor 4 (TLR4) mediated recognition (44–46). Numerous studies have shown that HDL particles have the capability to bind and neutralize LPS in plasma, reducing the availability and the chance of LPS to bind TLR4. Although numbers of studies showed that LPS can also bind to and are neutralized by VLDL (47–51), LDL (48–52), HDL (48–52), apoA-I (53), apoB (53), and apoE (54), binding properties of HDL showed to be the most potent. During the transfer of LPS into lipoproteins, LPS-binding protein plays a critical role as it binds to LPS and it is associated with apoA-I containing particles that may explain the preferential binding of LPS to HDL (55,56). The mechanism of the neutralizing LPS is likely to occur due to the ability of HDL to absorb LPS in its phospholipid surface (**Figure 1.4**) (57–59). HDL could also facilitate the release of LPS that is already bound to macrophages to reduce macrophage activation (60). In addition, HDL promotes LPS neutralization and clearance by acting with the high-affinity HDL receptor, SR-BI (61–63). In the absence of either SR-BI or HDL in mice, the ability and capability to neutralize LPS in LPS- or cecal ligation and puncture (CLP)-induced model was critically impaired (61,62,64). These findings suggest that HDL can neutralize LPS and promote LPS clearance via SR-BI-mediated LPS uptake that would be a potentially more efficient and effective strategy for LPS clearance in comparison to neutralization via anti-LPS monoclonal antibodies.
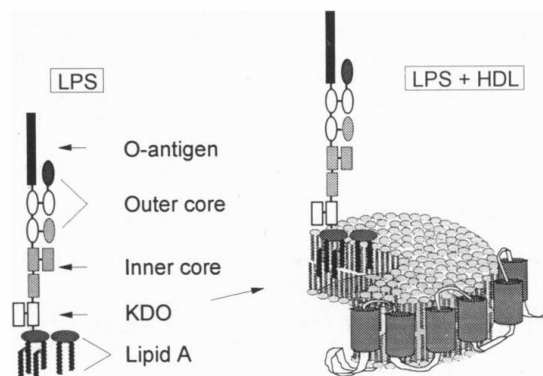
Figure 1.4. *Structural model of LPS binding and neutralization by HDL. HDL can absorb LPS via the insertion of membrane-anchoring (Lipid A) domain of LPS into the phospholipid layer of discoidal HDL (59).*

The primary barrier of macrophage activation is a physical binding of LPS where HDL scavenge LPS and prevent LPS-induced cytokine release. Nevertheless, numerous researches explained that HDL can also play as a pivotal modulator of the inflammatory response in macrophages. Lipid raft is a domain of plasma membrane of cells containing glycosphingolipids and protein receptors. The key difference between lipid raft and the plasma membrane is that it has a special lipid composition that is rich in cholesterol, sphingomyelin, and glycolipids (65). Of these, cholesterol is found to be 3 to 5 fold the amount of the surrounding bilayer (66). Whenever LPS is treated in macrophages, it has been reported that TLR4 is recruited to lipid raft faction and subsequently inducing tumor necrosis factor-alpha (TNF-α) (67). Therefore, as HDL promotes the efflux of cholesterol from macrophages via the process of RCT, it is believed that subsequent TLR activation might be inhibited via changes to lipid raft cholesterol content and reducing the TLR recruitment (4,67).

In addition, a recent study showed HDL can upregulate the expression of transcriptional regulator named activating transcription factor 3 (ATF3) (5). Activation of ATF3 leads to recruitment of histone deacetylase 1 to the promoter region of pro-inflammatory cytokine gene and assists in deacetylating to limit transcriptional binding (68,69). In addition, a recent study demonstrated that ATF3 can directly interact with the p65 subunit of nuclear factor kappa-light-chain-enhancer of activated B cells (NF-κB) to attenuate the NF-κB activity, thus, modulate the inflammatory response, rather than via indirect histone deacetylase 1 pathway (70). ATF3 has been recently identified as an HDL-inducible negative regulator of macrophage activation. A study revealed that HDL can inhibit the ability of TLRs to induce the expression of pro-inflammatory cytokines on the transcriptional level and it was fully dependent on expression of ATF3 both *in vitro* and *in vivo* (5).

1.5. Sepsis

1.5.1. Introduction

Sepsis is a life-threatening organ dysfunction caused by a dysregulated host response to infection (71). Sepsis is known to be the second most frequent cause of mortality in non-coronary intensive care units (ICU) which mortality rate accounts as much as 50% and the tenth overall cause of death in high-income countries (72,73). Sepsis is responsible for over 1,000,000 cases and more than 250,000 deaths in the United States annually (74,75). Moreover, sepsis represents a significant economic burden which total hospital cost in 2011 was over $20 billion (76). Globally, sepsis is estimated to account for 19 million cases per year, however, true incidences are presumed to be far higher (77). Sepsis affects all ages, sex, and race. Infants and elderly people are more vulnerable than other age groups, males than females, and blacks than whites (78,79). Despite its worldwide importance, public awareness of sepsis is very poor and reported incidences is keep increasing (75,80,81).

Sepsis can occur as a result of community-acquired and healthcare-associated infections. Among various causes, pneumonia is the most common cause responsible for about 50% of all cases. Intra-abdominal and urinary tract infections rank second and third respectively (82–85). A recent study from 14,000 ICU patients in 75 countries, Gram-negative bacteria were isolated in 62% of patients, Gram-positive bacteria in 47%, and fungi in 19% (85). The most common Gram-positive isolates are *Staphylococcus aureus* and *Streptococcus pneumoniae* whereas *Escherichia coli*, *Klebsiella species*, *Pseudomonas aeruginosa* are the most frequently isolated Gram-negative bacteria in sepsis (84,86).

The clinical features of patients with sepsis are varied depending upon the initial site of infection, type of organisms, and health status of patients. However, most patients typically exhibit

10

signs and symptoms such as fever, anorexia, tachycardia, systemic hypotension, low calculated systemic vascular resistance, abnormal sensorium, leukocytosis, thrombocytopenia, impaired blood coagulation, and elevated blood lactate concentration (87). Many times, the function of key organs such as heart, lung, kidney, and liver is impaired.

1.5.2. Pathophysiology

The pathophysiology of sepsis is extraordinarily complex and still remains poorly understood due to multiple subsequent and concurrent processes involving both excessive inflammation and immune suppression. Immune cells exhibit receptors known as pattern-recognition receptors (PRRs) that recognize invading bacteria, danger or harmful signals to the body, and activate immune response (88–90). PRRs can recognize conserved motifs expressed by microorganisms which are known as pathogen-associated molecular patterns (PAMPs) such as LPS. In the presence of microbial infection, PAMPs induce up-regulation of inflammatory gene transcription and rapid initiation of innate host defense responses by engaging with key receptors known as TLRs, a subfamily of PRRs, on the cell surface or intracellular within monocytes, macrophages, and polymorphonuclear leukocytes (PMNLs) as well as many other cell types, including pulmonary epithelial cells and vascular endothelial cells (87). PRRs can additionally recognize endogenous danger signals of intracellular proteins or mediators released from dying or injured cells during inflammatory stress. These proteins, called alarmins or danger-associated molecular patterns (DAMPs) such as heat shock proteins, fibrinogen, S100 proteins, hyaluronic acid, and high-mobility group box-1 protein (HMGB1), cause further amplification of the pro-inflammatory response through TLRs resulting in a positive-feedback loop promoting further amplification of dysregulated systemic inflammatory response (91–93). Thus, TLRs have emerged

11

as an essential receptor for the recognition of PAMPs and DAMPs, early detection of pathogens, and initiation of the innate immune response.

In the setting of sepsis, TLR4 mediated recognition of LPS is thought to be an important trigger of the inflammatory response in sepsis (**Figure 1.5**) (44–46). LPS binds to LPS-binding protein in serum and becomes solubilized (94). LPS is then transferred to an extrinsic glycosylphosphatidylinositol-anchored membrane protein on leukocytes called a cluster of differentiation 14 (CD14) (95). CD14 transfers LPS to an extracellular protein known as myeloid differentiation protein-2 (MD2), which binds to TLR4 to form the TLR4-MD2 receptor complex and triggers LPS recognition (95). LPS-MD2-TLR4 complex recruits cytoplasmic adaptor molecules via interaction with the Toll-interleukin-1 receptor (TIR) domains (45). Once TLR4 is activated via LPS recognition, TLR4-mediated signaling can further proceed through two major routes: the myeloid differentiation primary response gene 88 (MyD88) dependent and the TIR-domain-containing adapter-inducing interferon-β (TRIF)-dependent pathway (also known as the MyD88-independent pathway). MyD88-dependent pathway induces the activation of NF-κB and mitogen-activated protein kinase (MAPK) genes leading to the release of pro-inflammatory cytokines while TRIF-dependent pathway activates Type-1 interferon-inducible genes followed by NF-κB production (96).

Once immune cells are activated due to the engagement of PAMP and PRR, they secrete a variety of mediators, including cytokines, chemokines, nitric oxide (NO), and reactive oxygen species (ROS) (87). For example, activated NF-κB induces the transcription of cytokines such as TNF-α and interleukin-1β (IL-1β), both of which are capable of activating target cells, promoting the production of more inflammatory mediators, and causing both direct and indirect host injury

12

(97). IL-6, IL-10, IL-8, IL-12, interferon-γ (INF-γ), and granulocyte-colony stimulating factor (G-CSF) also play crucial roles in regulating the septic host response (97).

These cytokines (TNF-α and IL-1β in particular) increase the activity of inducible nitric oxide synthase (iNOS), which up-regulates the expression of inducible NO, a potent vasodilator, in endothelial cells. These vasoactive mediators cause vasodilation and septic shock. Moreover, TNF-α, IL-1β, INF-γ, and HMGB1 can activate endothelial cells by inducing adhesion molecules and injuring endothelial cells by inducing neutrophils, monocytes, macrophages, and platelets to bind to endothelium. These effector cells release mediators such as proteases, oxidants, prostaglandins, and leukotrienes. The major roles of the endothelium are selective permeability, vasoregulation, and provision of an anticoagulant surface. However, the release of proteases, oxidants, prostaglandins, and leukotrienes injure endothelial cells, leading to increased permeability, further vasodilation, alteration of the procoagulant–anticoagulant balance, and activation of the coagulation cascade.
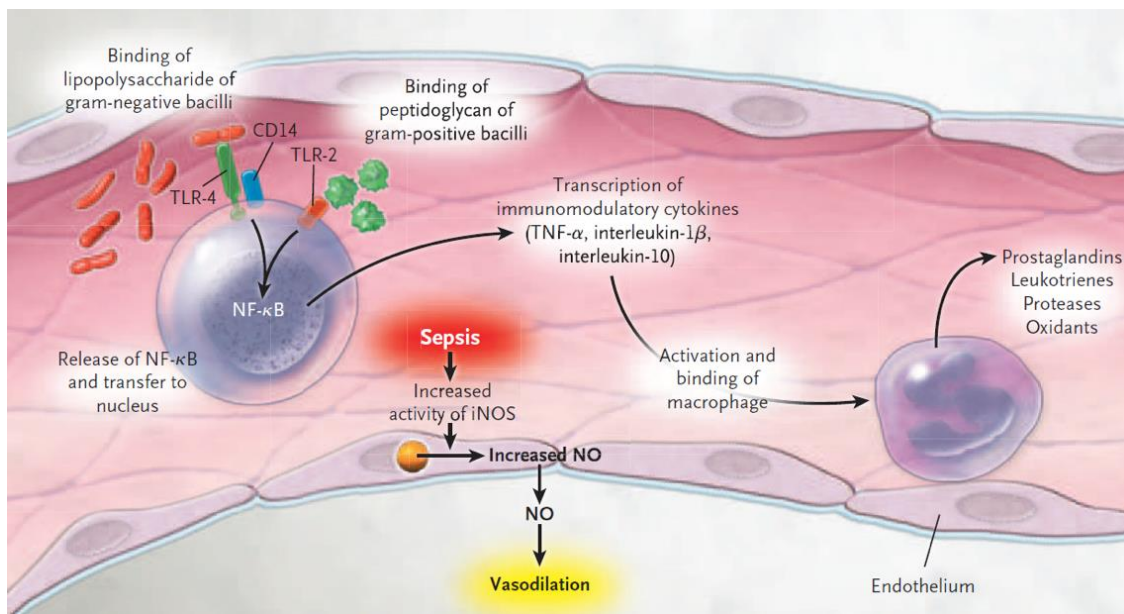
Figure 1.5. *Schematic representation of inflammatory response to sepsis* (98).

13

Another critical aspect of sepsis is the alteration of the procoagulant and anticoagulant balance, including induction of procoagulant factors and suppression of anticoagulant factors. Sepsis activates coagulation by upregulating the expression of tissue factor from endothelial cells. Activation of the coagulation cascade leads to a formation of thrombin-α that converts fibrinogen into fibrin. Platelets bind to fibrin and promote adherence to endothelial cells forming microvascular thrombi. Microvascular thrombi can release mediators and cause a microvascular obstruction which further amplifies the injury. Activation of the coagulation cascade caused by sepsis subsequently leads to increased levels of disseminated intravascular coagulation and multiple organ dysfunction.

1.5.3. *Current Therapeutic Approaches and Limitations*

One of the greatest disappointments during the past few decades is a failure to show significant benefits to patients with sepsis regardless of the advanced understanding and research in the pathogenesis of sepsis. In 1982, the first clinical trial in patients with septic shock was initiated with polyclonal antibodies that were directed against LPS. Since then, over 80 Phase II and III randomized controlled trials of pharmacological agents for sepsis have been conducted. Unfortunately, nearly all of these clinical trials have failed to provide efficacy.

One of the earliest sepsis drug development efforts began in 1982. Based on studies that showed passive immunization of mice with LPS-specific antibodies can protect the animals against lethality caused by injection of either LPS or viable Gram-negative bacteria (99), Ziegler and colleagues (100) conducted a clinical trial with a polyclonal antibody that was directed against LPS from the J5 mutant strain of *Escherichia coli* which have yielded positive result. However, a larger study has not shown to provide any therapeutic benefits, thus targeting of LPS has been

abandoned (101). The failure of this drug in clinical trials could be attributed to the apparent inability of the antibodies to inhibit LPS-induced cytokine production in human monocytes *in vitro* (102,103) and the fact that it partially sequesters LPS, thus only delaying rather than facilitating LPS clearance (104).

Eritoran (E5564) (105) and TAK-242 (106) are TLR4 antagonists developed based on a mechanism that LPS-mediated activation of immune cells requires interaction between LPS and TLR4. Anti-TNF agents such as afelimomab (107), a F(ab')2 fragment of a murine TNF-specific monoclonal anti-body, and IL-1 receptor antagonist (IL-1RA) such as anakinra (recombinant human IL-1RA) (108), were also developed owing to a pathophysiology that TNF and IL-1β are key alarm-phase cytokines that are secreted early in the inflammatory response. Although their initial clinical results displayed improved survival, all have failed to validate such results in their later clinical trials (87,109,110). In a different approach, Eli Lilly developed Xigris (drotrecogin alfa (activated)), a recombinant human form of activated protein C, to inhibit excessive activation coagulation system in order to improve survival in sepsis. Likewise, the initial Phase III trial yielded a positive result (111) which led to regulatory approval in North America and Europe. However, subsequent clinical results were disappointing (84,112,113) thus the product was withdrawn from the market in 2012. Furthermore, drugs such as filgrastim and sargramostim – to enhance the immune response, and 546C88 – to inhibit NOS (114), have been failed to show any significant benefit in sepsis (87).

There are numerous reasons for the inability to develop successful treatments for sepsis. One of the main concerns is that heterogeneous groups of patients are enrolled for clinical trials. Over the past few decades, systemic inflammatory response syndrome (SIRS) criteria were extensively used as a basis for the enrollment of participants for clinical trials which were often

difficult to distinguish from sepsis and SIRS thus resulting in a heterogeneous set of patients. Therefore, recent international consensus recommended using Sequential Organ Failure Assessment (SOFA) scoring system instead of SIRS scoring system to clinically define sepsis patients (71). Another reason for failure is that some drug compounds are found not to be biologically active. For example, two LPS-specific monoclonal antibodies, HA-1A and E5, completely lack to show efficacy to neutralize the pro-inflammatory effect of LPS in Phase III clinical trials.

As of today, the only drug that shows a positive effect is a relatively low dose of hydrocortisone (200 mg per day up to 7 days) (115). Because it has been broadly used for treatments involving excessive inflammation such as asthma or rheumatoid arthritis, it has been investigated as well as in sepsis. Nevertheless, the use of hydrocortisone is only supported by meta-analysis, whereas the two largest studies had conflicting results and other clinical trials are currently ongoing (74).

1.5.4. HDL Alteration in Sepsis

Profound changes in the concentration and composition of HDL have been established in patients with sepsis (11,116–118). Multiple studies revealed that a marked decline in serum HDL levels was observed during infection and inflammation (11,116,117,119,120). Patients with sepsis had reductions in HDL-cholesterol (HDL-C) levels of 40 – 70% compared to healthy subjects and inflammation induced major changes in HDL levels and composition (11–13). Mediators of inflammation such as TNF-α and IL-6 induce expression of serum amyloid A (SAA) (121) and group IIA secretory phospholipase A_2 (sPLA$_2$-IIA) (122), which dramatically alter HDL apolipoprotein content and levels, respectively. During infection and inflammation, acute-phase

16

SAA in the plasma associated with HDL displacing apoA-I and becoming the predominant apolipoprotein of HDL (acute-phase HDL) resulting in a reduction in normal HDL but not total HDL (11). Also, SAA can stimulate the catabolism of HDL (121) and can activate sPLA$_2$-IIA to modify the role of HDL (123). In addition, cytokines have been shown to reduce the synthesis and secretion of apolipoproteins in liver cells *in vitro* which would result in low apoA-I during inflammation (124). Moreover, a study suggest that a decreased activity of LCAT during inflammation may contribute to decreased level of HDL-C due to impaired CE formation and HDL maturation (125). Further, a low level of HDL-C upon the initiation of sepsis significantly contributed to an increase in mortality and clinical outcomes (12).

1.6.   Synthetic HDL

1.6.1. ApoA-I Mimetic Peptides

Native HDL displays complex synthesis and remodeling pathways that result in a significant structural variability between individual particles which leads to a myriad of different HDL functions. Therefore, isolation and purification of this native HDL from human plasma under current good manufacturing practice (cGMP) is very costly and laborious for laboratories and pharmaceutical uses. Moreover, safety concerns and manufacturing issues cannot be overlooked. To address these issues, various recombinant apoA-I proteins and apoA-I mimetic peptides have been developed over the past few years. These are designed to be homologous to the native apoA-I and optimized to maximize the different functional outcomes as described in **Table 1.2**. HDL complexed with such apoA-I mimetic peptides are known as reconstituted HDL (rHDL) or synthetic HDL (sHDL) systems which mimic *in vivo* characteristics of native HDL can be manufactured at a large scale. sHDL can facilitate clinical development of HDL-based therapeutics

17

cost-effectively with promising peptides and lipids that have been well documented in numerous clinical trials (126,127). sHDL is composed of apoA-I mimetic peptides to form HDL and mimics the physical, chemical, and biological activity of HDL. ApoA-I mimetic peptides are reported to be cost-effective and easy to be scaled up and quality controlled. Most apoA-I mimetics peptides are 18 to 22 amino acids long and designed based on sequences homologous to the native protein (128). Similar to endogenous apoA-I, the structure of mimetic peptides is the amphipathic α-helices. Based on *in vivo* and *in vitro* studies, apoA-I mimetic peptides showed abilities to bind to phospholipids and associate with native HDL particles (128,129). Moreover, mimetic peptides reproduced the effect of native HDL in terms of cholesterol efflux (130,131), interaction with HDL receptors (ABCA1, ABCG1, and SR-BI) (130), interaction with HDL-associated enzymes (LCAT) (129,132,133), and binding to LPS (8,134).

Table 1.2. Mimetic apoA-I peptides: Sequences and clinical applications.

Peptide	Sequence	Company	Optimized Functional Output	Ref
ESP24218	P-V-L-D-L-F-R-E-L-L-N-E-L-L-E-A-L-K-Q-K-L-K	Esperion	• Lipid binding • LCAT activation • RCT	(135)
D4F	Ac-D-W-F-K-A-F-Y-D-K-V-A-E-K-F-K-E-A-F-NH$_2$	Novartis	• Same as L4F Chemical stability	(136)
L4F	Ac-D-W-F-K-A-F-Y-D-K-V-A-E-K-F-K-E-A-F-NH$_2$	Novartis	• RCT • Lipid binding • Inflammation reduction	(137)
Reverse 4F	K-L-K-Q-K-L-A-E-L-L-E-N-L-L-E-R-F-L-D-L-V-Inp Ac-F-A-E-K-F-K-E-A-V-K-D-Y-F-A-K-F-W-D-NH$_2$	Kos pharmaceuticals	• Lipid binding • Cholesterol mobilization	(138)
5A	D-W-L-K-A-F-Y-D-K-V-A-E-K-L-K-E-A-F-P-D-W-A-K-A-A-Y-D-K-A-A-E-K-A-K-E-A-A	KineMed Inc.	• ABCA1 activation • Low hemolysis • Lipid binding	(131)
18A	Ac-E-W-L-E-A-F-Y-K-K-V-L-E-K-L-K-E-L-F-NH$_2$	N/A	• RCT	(139)
ATI-5261	Ac-E-V-R-S-K-L-E-E-W-F-A-A-F-R-E-F-A-E-E-F-L-A-R-L-K-S-NH$_2$	Roche	• Anti-oxidant properties • Promote ABCA1 dependent cholesterol efflux	(140)

1.6.2. Method of Synthesis

Traditionally, the preparation of synthetic HDL in the laboratory setting was done by using a cholate dialysis method. It uses the plasma-purified human apoA-I which is then reconstituted with phospholipids and cholesterol to synthesize reconstituted HDL (rHDL) (141). Unfortunately, several drawbacks exist in the cholate dialysis method. It requires the addition of detergents that may result in incomplete detergent removal during the later stage of synthesis, is time-consuming, has the possibility of endotoxin contamination of ApoA-I, and leads to particle heterogeneity. Sonication of peptide and lipid mixture is another HDL synthesis method, but this also displayed similar drawbacks resulting in highly heterogeneous particles (141). A patented technique called co-lyophilization from Esperion Therapeutics, can, however, conveniently prepare sHDL without the previously described concerns (141). Concisely, the process involves co-dissolving peptide and lipid constituents in an organic solvent, freeze-drying, and subsequent hydration with an isotonic, neutral buffer that can be easily scaled up and results in high homogeneous sHDL particles.

1.6.3. sHDL as Potential Therapeutics in sepsis

Accordingly, several studies have been conducted to investigate the protective ability of administered rHDL against endotoxemia (**Table 1.3**). To further investigate whether low HDL levels promote septic death, apoA-I-null mice were used to mimic a model of low circulating HDL. As a result, a deficiency in HDL caused greater susceptibility to CLP-induced septic death with attenuated LPS neutralization and LPS clearance, whereas overexpression of apoA-I resulted in improved survival rate in both CLP and LPS-induced sepsis models (64,142). It is worth noting that HDL, rather than lipid alone, serves more efficacious in septic shock (59).

Bacterial infections are the major cause of sepsis. *in vivo* studies revealed binding of LPS to lipoproteins protected animals from LPS-induced fever and hypotension, as well as the infusion of rHDL suppressed the inflammatory response to injected LPS in humans and animals (143,144). Also, transgenic mice having twice the amount of HDL in plasma compared to wild-type mice displayed significantly decreased levels of TNF-α and lethality induced by LPS (59). Subsequently, study found that the administration of rHDL to blood from healthy volunteers inhibited TNF- α stimulation from LPS *ex vivo* (145).

As sepsis is almost invariably associated with altered coagulation, frequently leading to DIC, several studies addressed the mechanism by which that HDL exhibited protective mechanism against altered coagulation. Administration of rHDL resulted in downregulation of tissue factor expression (146) and inhibition of platelet aggregation (147). Infusion of rHDL in a rabbit model of atherosclerosis showed increased expression of thrombomodulin, a coagulant factor supporting the activation of protein C and suppression of thrombin generation, in atherosclerotic lesion (148). In addition, rHDL has been shown to attenuate MOD (149), hemorrhagic shock (150), and ischemia-reperfusion injury (151,152). Furthermore, while patients with sepsis continuously have reduced HDL-C levels, one study revealed that a direct infusion of sHDL showed a successful elevation of the plasma HDL *in vivo* (153).

Table 1.3. Experimental HDL therapies in animal models of sepsis and their outcomes (154).

HDL	Dose & Administration	Sepsis Model	Main Findings	Ref.
18A:Egg PC (1:2 wt/wt) sHDL	80 mg/kg; prophylactic tail vein IV infusion	Swiss Webster mice; LPS (salmonella) 10 mg/kg; IP injection; within 15 min of HDL	3-4 fold increase in 48-hour survival rate vs control (p<0.05)	(59)
L-4F Peptide	25 mg/kg, IP, concurrently with LPS	Sprague-Dawley rats; 10 mg/kg LPS; IP injection	Reduction in VCAM-1 expression in excised aortae	(134)
4F Peptide	10 mg/kg; IP injection post-LPS challenge	Sprague-Dawley rats; LPS 10 mg/kg or 30 mg/kg; IP injection	**10 mg/kg LPS:** 4F slowed LPS plasma clearance; reduced hypotension at 6 hr; **30 mg/kg LPS**: 4F increased plasma HDL levels; increased 24-hr survival	(155)

4F Peptide	10 mg/kg, IP, 6 hours post-CLP	Sprague-Dawley rats; CLP	Reduced IL-6; restored CO, right atrial pressure, and plasma volume; improved 2-day survival rate; reversed sepsis-induced changes in lipoprotein profile	(156)
4F Peptide	10 mg/kg; IP injection 6 hr post-CLP	Wistar Rats; CLP	Restored renal, hepatic, and cardiac functions; reduced renal tubule damage; restored expression levels of Slit2, Robo4, and eNOS; increased plasma HDL; improved 4-day survival; no change in MAP	(157)
D-4F Peptide	20 µg daily for 9 days; IP injection	C57BL/6J mice; nasally inoculated with 10^5 PFU influenza virus A/WSN/33	Prevented lymphoid hyperplasia; increased PON activity; prevented drop in core body temperature; suppressed plasma IL-6 levels; increased plasma HDL and inhibited lipoprotein alteration; reduced viral titers by > 50% at all-time points	(133)
ApoA1	10 mg/kg; IP injection 1 hr post-LPS challenge	Wistar rats; LPS 1 mg/kg (TNF analysis) or 5 mg/kg (survival study); IP injection	Reduced plasma TNF-α levels in rats given 1 mg/kg LPS; increased 5-day survival rate from 0 to 90% in rats given 5 mg/kg LPS	(158)
ApoA1, human plasma purified	100 mg/kg; IV infusion post-LPS challenge	Balb/c mice; LPS 5 mg/kg; IP injection	Increased both survival rate and average survival time over 3 days	(159)
ApoA1 Milano ApoA1:Soy PC (1:3.35 mol/mol) rHDL	40 mg/kg; prophylactic IV injection	Wistar rats; 400 EU/kg Gram-negative bacterial endotoxin; IV injection	Increase in HDL-C; improved renal and hepatic function; inhibition of cytokines TNF-α, IL-1β, IL-6; reduced expression of ICAM-1	(160)
ApoA1:Soy PC (1:200 mol/mol) rHDL	75 mg/kg ApoA1; prophylactic continuous IV infusion over 25 min	NZW rabbits; LPS 25 µg/kg continuous IV infusion over 6 hr; start 20 min post-rHDL treatment	Complete inhibition of TNF-α; prevented LPS-induced hypotension; reduced metabolic acidosis; no significant effect on serum LPS levels	(161)
ApoA1:Egg PC (1:2 w/w) rHDL	500 mg/kg ApoA1; IV infusion at 0.1 g/kg/hr; split into 3 doses: 0.3, 0.1, and 0.1 g/kg administered at 0.5, 8, and 16 hr post-infection, respectively	2-year old Beagles surgically implanted with E. coli-infected fibrin clot	Reduced plasma endotoxin levels; decreased plasma TNF-α; decreased liver function; decreased 2-day survival and average survival time	(162)
CSL-111 ApoA1:Soy PC (1:150 mol/mol) rHDL	75 mg/kg ApoA1; **a)** Prophylactic IV infusion over 40 min **b)** Treatment by IV infusion over 20 min, 1 hr post-bacterial challenge	NZW Rabbits **1)** Gram (-) Sepsis: 4 x 10^9 CFU/kg E. coli; IV infusion over 2 hr **2)** Gram (+) Sepsis: 2 x 10^9 CFU/kg; IV infusion over 2 hr	**1. a)** Prophylactic rHDL: reduced plasma LPS and TNF-α; reduction in metabolic acidosis; no effect on hypotension or blood bacterial levels **1. b)** rHDL Treatment: reduction in LPS after 4 hours; reduced metabolic acidosis and creatinine; no effect on blood bacterial counts or TNF-α; no effect on hypotension **2.** No effect in Gram (+) sepsis	(163)
CSL-111 ApoA1:Soy PC (1:150 mol/mol) rHDL	25 mg/kg or 50 mg/kg ApoA1; Prophylactic IV infusion over 40 min	NZW rabbits; LPS 10 µg/kg; continuous IV infusion over 2 hr; start 15 min post-rHDL completion	Reduced TNF-α levels and increased TNF-α clearance for both rHDL doses; rHDL 50 mg/kg reduced hypotension at t=3-4 hr; no effect on plasma LPS levels; no effect on blood leukocyte count	(164)
CSL-111 ApoA1:Soy PC (1:150 mol/mol) rHDL	40 mg/kg; prophylactic IV infusion over 4 hr	Healthy male volunteers (20-28 yrs); Endotoxin 4 ng/kg IV bolus; given 3.5 hrs post-rHDL start	Elevated HDL levels; reduced endotoxin-induced clinical symptoms, i.e. chills, myalgia, backache, nausea, and vomiting; reduced plasma cytokine levels of TNF-α, IL-6, and IL-8; inhibited early leukopenia, monopenia, and neutropenia; reduced monocyte CD14 expression	(144)

21

1.7.   Research Scope

The promising anti-inflammatory activities of HDL and correlation between HDL-C levels and outcomes in various diseases (i.e. sepsis and CVD) motivated many nonclinical and clinical investigations implementing rHDL or sHDL. While a significant emphasis has been put on investigating the protein or peptide composition of HDL such as apoA-I, apoA-I mutants, and mimetic peptides, the importance of the phospholipid component of HDL has been neglected. In addition, many developments of rHDL or sHDL have been focused on maximizing cholesterol efflux capacity while other functional aspects, such as anti-inflammatory activities, have been overlooked.

Lipids are a key component in HDL that provide the overall structure of HDL and serve as a substrate for many receptors and enzymes associated with HDL. The phospholipid composition of HDL can potentially have an impact on the size, net charge, rigidity, functionality, pharmacokinetics, and pharmacodynamics properties of sHDL (153). Therefore, the work presented here will demonstrate the impact of phospholipids on sHDL, particularly focusing on anti-inflammatory activities.

1.8.   Thesis Overview

The overall goal of this thesis is to investigate the impact of phospholipid composition of sHDL on its anti-inflammatory activities and reverse cholesterol transport. This study can provide a potential approach to improve the specific functionality of sHDL for a disease-specific therapeutic strategy by altering the phospholipid composition.

In chapter 2 of this thesis, we studied how sHDL phospholipid composition can influence the protective mechanisms against sepsis. We discuss the clinical relationship between plasma

HDL levels and septic mortality, and therefore why HDL therapy would be a potential therapeutic strategy against sepsis. We designed multiple formulations of sHDL by varying phospholipid compositions and extensively investigated these *in vitro* and *in vivo* to validate the anti-inflammatory activities of each sHDL formulation and to understand the key mechanistic contributions of sHDL in a laboratory sepsis model. We demonstrated the optimal composition of sHDL to maximize the therapeutic effect in sepsis.

In chapter 3, we investigated how sHDL phospholipid composition can impact pharmacokinetic and pharmacodynamic profiles. sHDL has been proposed as a treatment of CVD. Significant research has been performed to optimized apoA-I mimetic peptides to improve the cholesterol efflux capacity and LCAT activation both *in vitro* and *in vivo*, however, the majority of studies were optimized as "naked" peptide and only a few studies were investigated in rHDL or sHDL. In addition, a few studies examined the effect of phospholipid composition on the activity of sHDL *in vitro*, yet *in vivo* effects have not been evaluated. Therefore, we systematically evaluated the effect of both peptide sequence and phospholipid composition of sHDL to observe the impact on cholesterol mobilization and cholesterol esterification *in vitro* and *in vivo*.

In chapter 4, we designed a new nano-mimetic sHDL known as nano-micelle (MiNano) to overcome the limitation of HDL therapeutics that may arise in the near future. Since the majority of HDL therapeutics that are in clinical trials heavily depend on human plasma purified apoA-I, problems may arise when the protein reaches its supply limitation due to human blood supply as well as expensive and laborious manufacturing and purification processes. Therefore, we investigated MiNano that mimics the structure of sHDL with small particle size and a hydrophobic core and hydrophilic exterior, but without any functional protein such as apoA-I. We compared biological functions of MiNano to sHDL, including the capability to efflux cholesterol from

macrophages and anti-inflammatory abilities *in vitro* and *in vivo*, as well as observed the effectiveness in animal models of atherosclerosis.

Finally, in chapter 5, we draw the final conclusions of the thesis work and discuss future studies. Chapter 2 will be submitted to *Journal of Lipid Research*, Chapter 3 is submitted in *Journal of Pharmacology and Experimental Therapeutics*, and Chapter 4 will be submitted for publication once the manuscript is completed. Each research chapter is written in manuscript format.

Chapter 2

Phospholipid Composition of Synthetic HDL Influence the Protection Against

Lipopolysaccharide-Induced Inflammation

2.1.   Abstract

Sepsis is a major health issue and there is no Food and Drug Administration (FDA) approved drugs. Recent studies suggest that reconstituted HDL (rHDL) is a potentially effective therapy for sepsis. While most of the studies focus on proteins or peptides, in this study, we hypothesize that changes in the phospholipid components in rHDL improve the therapeutic effect. To test our hypothesis, we synthesized different fluidity of rHDL by complexing a 22-amino acid peptide and different phosphatidylcholines (22A-1-palmitoyl-2-oleoyl-glycero-3phosphocholine, 22A-POPC; 22A-1,2-dimyristoyl-sn-glycero-3-phosphocholine, 22A-DMPC; 22A-1,2-dipalmitoyl-sn-glycero-3-phosphocholine, 22A-DPPC; 22A-1,2-distearoyl-sn-glycero-3-phosphocholine, 22A-DSPC) and examined their effects *in vitro* and in the LPS-induced endotoxemia model. We found that, among four rHDLs, fluid liquid crystalline phase 22A-DMPC most effectively suppresses NF-κB signaling, TLR4 signaling through regulating TLR4 recruitment into lipid rafts, and promotes activating transcription factor 3 (ATF-3) expression which significantly attenuated inflammatory activity. Consistent with the regulation of inflammatory signaling, 22A-DMPC most effectively improved mortality and protected organs in mice challenged with lethal doses of LPS. In conclusion, we demonstrate that changes in phospholipid composition markedly improve its capability of suppression of inflammatory

signaling and efficacy of sepsis therapy. 22A-DMPC displayed the best therapeutic effects against LPS-induced sepsis via multifaceted mechanisms including LPS neutralization, reduced TLR4 recruitment into lipid raft, and ATF3 promotion.

2.2. Introduction

Sepsis, a life-threatening organ dysfunction caused by a dysregulated host response to infection, remains a major health challenge and is responsible for high morbidity, mortality, and cost. This is, at least in part, a consequence of a limited understandings of the extremely complex mechanisms that regulate the inflammatory response. Numerous advances have been made in anti-inflammatory and anti-microbial treatments, yet, no effective treatments for sepsis have been yet commercially available. Lipopolysaccharides (LPS), an endotoxin component present on the outer membrane of Gram-negative bacteria, is recognized as the most potent initiator of inflammation, capable of inducing sepsis (71). LPS can trigger the inflammatory response in sepsis via Toll-like receptor 4 (TLR4) mediated recognition (44–46). Upon LPS-induced TLR4 activation, TLR4-mediated signaling activates the nuclear factor kappa-light-chain-enhancer of activated B cells (NF-κB) leading to the release of pro-inflammatory mediators (96) causing a severe immune response, potentially leading to septic shock and multiple organ dysfunction.

HDL is the smallest and densest of the plasma lipoproteins consisting of apolipoprotein A-I (apoA-I) and phospholipids. HDL exerts a number of physiological functions, including cholesterol mobilization via reverse cholesterol transport. Additionally, HDL exerts an array of anti-inflammatory activities through a number of mechanisms. HDL preferentially binds to and neutralizes circulating endotoxin, returning it to the liver for elimination (2,3). HDL also reduces TLR4 recruitment into lipid raft via cellular membrane cholesterol depletion (4). Furthermore,

HDL induces activating transcription factor 3 (ATF3) expression to modulate TLR-induced pro-inflammatory cytokines (5–7).

Profound changes in the concentration and composition of HDL have been established in patients with sepsis (11,116–118). Multiple studies revealed that a marked decline in serum HDL levels was observed during infection and inflammation (11,116,117,119,120). Patients with sepsis have reductions in HDL-cholesterol (HDL-C) levels of 40 – 70% compared to healthy subjects and inflammation induced major changes in HDL composition (11–13). Further, a low level of HDL-C upon initiation of sepsis are associated with an increase in mortality and clinical outcomes (12, Morin unpublished work 2019).

The promising anti-inflammatory properties of HDL and inverse correlation between HDL-C level and mortality in sepsis fueled many nonclinical and clinical investigations assessing the role of HDL in sepsis via administration of reconstituted HDL (rHDL) (154). A majority of these studies utilized HDL protein or peptide, as the efficacy of naked apoA-I, apoA-I mutant, and apoA-I mimetic peptides have been reported (134,155–160). Nevertheless, the importance of HDL phospholipid composition has been largely neglected despite its role in intracellular signaling and receptor interactions (165). For instance, HDL sequesters LPS within its phospholipid layer to promote LPS neutralization and anti-inflammatory activity (57–59). Moreover, the protective mechanisms of HDL in sepsis remain poorly understood and treatment of sepsis via HDL infusion has yet to garner significant attention despite the important relationship between HDL and sepsis.

In this study, we investigated the impact of phospholipid on the anti-inflammatory activities of HDL. Several studies emphasized the importance of the physical state of phospholipid on HDL that can potentially impact the functionality in cholesterol efflux but not in anti-inflammatory activities. Notably, liquid crystalline unsaturated phospholipids promote more

efficient cholesterol acceptor than gel phase saturated phospholipids due to more fluid liquid crystalline lipids are capable of greater exogenous lipid molecule (e.g. cholesterol) insertion in contrast to relatively rigid gel phase phospholipids (31). To this extent, we hypothesize that HDL with a fluid liquid crystalline lipid phase would also result in enhanced anti-inflammatory activities by accelerating the efflux of exogenous molecules (e.g. LPS and cholesterol) and accessibility to phospholipid.

To investigate our hypothesis, we prepared rHDLs by complexing apoA-I mimetic peptide, 22A, with different phosphatidylcholines (PC). 22A peptide was chosen as it retains the biological activity of endogenous apolipoprotein A-I and has shown favorable safety and pharmacokinetics in human clinical trials (127,166). PC is the largest class of phospholipids, comprising 33 – 45% of total HDL lipid mass (26) and is recognized to contribute to the potent anti-inflammatory effect of HDL (165). Thus, we selected PC as our HDL phospholipid composition with variations in fatty acid chain length and saturation to produce different fluidity of PC phase on rHDL due to distinct phase transition temperature (T_m) of each phospholipid (1-palmitoyl-2-oleoyl-phosphatidylcholine, POPC; 1,2-dimyristoyl-sn-glycero-3-phosphatidylcholine, DMPC; 1,2-dipalmitoyl-sn-glycero-3-phosphatidylcholine, DPPC; and 1,2-distearoyl-sn-glycero-3-phosphatidylcholine, DSPC) and examined the impact of fluidity of rHDL on its anti-inflammatory activities against LPS-induced inflammation *in vitro* and *in vivo*.

Here, we demonstrated that changes in phospholipid composition of rHDL significantly enhance the anti-inflammatory activities due to different fluidity of rHDL. Fluid liquid crystalline phase rHDLs, particularly 22A-DMPC, most effectively modulated NF-κB signaling and pro-inflammatory mediators via TLR4 signaling as compared to rigid gel phase rHDL. Interestingly, only 22A-DMPC further reduced TLR4 recruitment into lipid rafts and promoted ATF3 expression

which significantly modulated inflammatory activity with rHDL pre-treatment. Accordingly, 22A-DMPC improved mortality and protected organs from inflammatory injury in mice challenged with a lethal dose of LPS.

2.3. Materials and Methods

2.3.1. Animals and reagents

7 – 9 week old male and female C57BL/6 mice were purchased from Jackson Laboratories. All protocols were approved by the Institutional Animal Care & Use Committee (IACUC) at the University of Michigan, Ann Arbor.

22A (PVLDLFRELLNELLEALKQKLK) peptide was synthesized by GenScript (Piscataway, NJ) and purity was approximately 85% as determined by HPLC. 1-palmitoyl-2-oleoyl-glycero-3phosphocholine (POPC), 1,2-dimyristoyl-sn-glycero-3-phosphocholine (DMPC), 1,2-dipalmitoyl-sn-glycero-3-phosphocholine (DPPC), and 1,2-distearoyl-sn-glycero-3-phosphocholine (DSPC) were purchased from Nippon Oil and Fat (Osaka, Japan). LPS conjugated with Alexa Fluor™ 488 was purchased from Thermo Fisher Scientific (Waltham, MA). All LPS (from E. coli O111:B4) were purchased from Sigma Aldrich (St. Louis, MO). LPS purified by ion-exchange chromatography (L3024) was used throughout the entire experiment, except for the survival study in which LPS purified by phenol extraction (L2630) was used. Alexa Fluor 488-conjugated anti-mouse TLR4 (Clone: UT41) and Alexa Fluor 488-conjugated cholera toxin subunit B (CT-B) were obtained from Thermo Fisher Scientific (Waltham, MA). ATF-3 Antibody (C-19) (sc-188, 1:800 dilution) was purchased from Santa Cruz Biotechnology (Dallas, TX). GAPDH (D16H11) XP® Rabbit Monoclonal Antibody (5174, 1:4000 dilution) and Anti-rabbit

IgG, HRP-linked Antibody (7074, 1:5000 dilution) were purchased from Cell Signaling Technologies (Danvers, MA).

2.3.2. Cell culture

RAW 264.7 and J774A.1 macrophages were cultured in Dulbecco's Modified Eagle Medium (DMEM) containing 10% fetal bovine serum (FBS), 1% Penicillin-Streptomycin (10,000 U/mL), and 100 μg/mL Normocin™. HEK-Blue™ hTLR4, which stably expresses CD14, MD2, NF-κB reporter and human TLR4, was purchased from InvivoGen (San Diego, CA) and grown in DMEM containing 10% FBS. HEK-Blue hTLR4 express the secreted embryonic alkaline phosphatase (SEAP) reporter gene under the control of the NF-κB promotor, which enables the quantification of cell activation by measuring SEAP activity in medium containing specific enzyme substrates. All cell lines were cultured at 37 °C in a humidified 5% CO_2 incubator.

2.3.3. Preparation of rHDL

rHDL were prepared via co-lyophilization procedure that we have previously developed in our lab (153). Briefly, 22A (PVLDLFRELLNELLEALKQKLK) and phosphatidylcholines (POPC, DMPC, DPPC, or DSPC) were mixed at 1:2 weight ratio in acetic acid. The resulting solution was then flash frozen in liquid nitrogen and placed on a freeze-dryer for at least 2 days to remove organic solvents. The lyophilized powder was rehydrated with phosphate buffered saline (PBS) and thermal-cycled above and below the transition temperature of each phospholipid to facilitate peptide-lipid binding. Finally, the pH of rHDL solutions was adjusted to 7.4 using NaOH and filtered with a 0.2 μm sterile filter. All rHDL concentrations are expressed in terms of 22A peptide concentration.

2.3.4. Characterization of rHDL

The quality of the resulting rHDL was analyzed by the following analytical techniques. The purity of rHDL was determined by gel permeation chromatography (GPC), with UV detection at 220 nm, using a Tosoh TSKgel G3000SWxl column (King of Prussia, PA). The particle size of rHDL was determined by dynamic light scattering (DLS) on Malvern Zetasizer Nano ZSP (Westborough, MA) and the volume intensity average values were reported. The morphology of rHDL was assessed by transmission electron microscopy (TEM). rHDL samples were loaded on a carbon film-coated 400 mesh copper grid from Electron Microscopy Sciences (Hatfield, PA) that were negatively stained with 1% (w/v) uranyl formate and dried before TEM observation. All specimens were imaged with 100kV Morgagni TEM equipped with a Gatan Orius CCD. Transition temperature (T_m) of rHDL was analyzed by two state modeling using TA Nano Differential Scanning Calorimetry (DSC) (New Castle, DE).

2.3.5. Analysis of fluorescent-LPS binding to rHDL

LPS conjugated with Alexa Fluor™ 488 (10 µg/mL) was pre-incubated for 1 h at 37 °C, then mixed with different formulations of rHDL (1 mg/mL) and incubated for 1 hour at 37 °C. Samples were centrifugated at 15000 rpm for 10 min. 25 µL of samples were injected into the Shimazu Nexera-I LC 2040d Plus system connected with RF-20A prominence fluorescence detector (Kyoto, Japan) and separated with a Tosoh Bioscience TSKgel G3000Wxl (7.8 mm X 30 cm, 5 µm). PBS (pH 7.4) was chosen for the mobile phase with a flow rate of 0.5 mL/min. The signal was detected at 220 nm and at an excitation wavelength of 495 nm and an emission wavelength of 519 nm.

2.3.6. Analysis of LPS-induced NF-κB expression

The HEK-Blue cell system from InvivoGen was used to analyze the neutralization of the LPS-induced inflammatory response. HEK-Blue hTLR4 cells stably express reporter-linked human TLR4, CD14, MD2, and NF-κB that are designed for studying the stimulation of human TLR4. Briefly, HEK-Blue hTLR4 cells were cultured in DMEM containing 10% low endotoxin FBS and selective antibiotics according to the manufacturer's instructions. The growth medium was discarded, and cells were resuspended in the HEK-Blue Detection medium. Cells were seeded at 25,000 cells per well. Cells were treated with various formulations of rHDL at a peptide concentration of 10, 30, or 100 μg/mL in a presence or an absence of 2 ng/ml of LPS. The cells were then incubated for 18 h. LPS binding to TLR4 results in the induction of NF-κB reporter expression, causing the HEK-Blue detection medium to turn blue. The blue color was quantified by measuring absorption at 650 nm using a SpectraMax M3 plate reader from Molecular Devices (San Jose, CA).

2.3.7. In vitro analysis of pro-inflammatory mediators

RAW 264.7 cells were plated in 96-well microplate at a density of 5 x 10^4 cells/well and incubated until reaching 80% confluency. Cells were washed with PBS and different formulations of rHDL were added at peptide concentrations of 10, 30, or 100 μg/mL for 18 h followed by stimulation with LPS. To quantify the concentration of inflammatory cytokines including TNF-α, IL-6, and MCP-1, samples were prepared BD Cytometric Bead Array Mouse Inflammation Kit (San Jose, CA) per manufacturer's instruction. Then, prepared samples were analyzed with flow cytometry, Beckman Coulter CytoFLEX (Brea, CA).

2.3.8. Cellular cholesterol efflux analysis

RAW 264.7 were plated in 24-well plate at a density of 1 x 10^5 cells/well and incubated for 24 h. Cells were washed with PBS once and labeled with 1 µCi of [^{3}H] cholesterol/mL for 24 h in the growth medium. Cells were then washed with PBS and different formulations of rHDL were added at peptide concentrations of 10, 30, or 100 µg/mL in DMEM containing 0.2 mg/mL of fatty acid-free bovine serum albumin (BSA). After 18 h of incubation, media were collected, and cells lysed in 0.5 mL of 0.1% SDS and 0.1 N NaOH. Radioactive counts in media and cell fractions were measured by liquid scintillation counting using Perkin Elmer Tri-Carb 2910TR (Waltham, MA) and percent cholesterol efflux was reported by dividing the media count by the sum of the media and cell counts.

2.3.9. Analysis of lipid raft and TLR4 recruitment

J774A.1 were plated in 24-well microplate at a density of 5 x 10^4 cells/well and incubated until reaching 80% confluency. Cells were treated with either PBS or different formulations of rHDL at a peptide concentration of 100 µg/mL for 18 h. The control group was treated with 10 mM methyl-β-cyclodextrin for 30 min. Cells were washed with ice-cold PBS containing 2% FBS. Then, cells were incubated with 8 µg/mL Alexa Fluor 594-conjugated CT-B for 15 minutes and 2 µg /mL Alexa Fluor 488-conjugated anti-TLR4 for 30 minutes to label lipid raft and TLR4, respectively. Labeled cells were washed with ice-cold PBS containing 2% FBS and the percentage distribution of lipid raft and TLR4 were reported with the mean fluorescence intensity determined by MoFlo Astrios from Beckman Coulter.

2.3.10. RNA isolation and RT-PCR

RAW 264.7 cells were plated in a 6-well microplate at a density of 4×10^5 cells/well and incubated until reaching 80% confluency. Cells were then washed with PBS and different formulations of rHDL were added at peptide concentrations of 100 µg/mL for 1, 2, or 4 h. Cells were lysed and RNA was isolated using GeneJET RNA purification kit from Thermo Fisher Scientific. Approximately 1 µg of extracted RNA from each sample was transcribed to cDNA using SuperScript III First-Strand Synthesis System from Invitrogen. cDNA amplification was measured by quantitative real-time PCR on a StepOnePlus™ real-time PCR System from Applied Biosystems (Waltham, MA). TaqMan assays from Applied Biosystems were used to measure the following: *Gapdh* Mm99999915_g1; *Atf3* Mm00476033_m1. Gene expression was determined using the ΔΔCt method using Gapdh as the housekeeping control.

2.3.11. Cell lysis and immunoblotting:

RAW 264.7 cells were plated in 6-well microplates at 5×10^5 cells/well and incubated until reaching 80% confluency. Cells were then washed with PBS and different formulations of rHDL were added at peptide concentrations of 100 µg/mL for 18 h. Cells were washed with ice-cold 1x PBS twice and lysed on ice for 30 min with 1x RIPA buffer (25mM Tris-HCl pH 7.6, 150mM NaCl, 1% NP-40, 1% sodium deoxycholate, 0.1% SDS) supplemented with cOmplete™ EDTA-free protease inhibitor cocktail and PhosSTOP from Roche (Indianapolis, IN). Lysates were clarified by centrifugation at 12,000 RPM for 10 min at 4°C and measured protein concentration by BCA assay. An equal amount of protein per sample was loaded on 4 – 15% pre-casted SDS-PAGE gels from Bio-Rad (Hercules, CA) with Tris/glycine/SDS buffer and proteins were transferred onto PVDF membranes. Membranes were blocked in 5% (wt/vol) BSA in Tris-buffered

saline with Tween-20 (TBS-T) for 1 h at room temperature and incubated 18 h at 4°C with specific

primary antibodies diluted in BSA. Membranes were then washed with TBS-T, incubated with

secondary antibodies for 1 h, and washed with TBS-T. Images were acquired on Protein Simple

FluorChem M imaging system (San Jose, CA).

2.3.12. Analysis of NF-κB expression and pro-inflammatory mediators from rHDL pre-treatment

Depending on the experiments, either HEK-Blue cells or RAW 264.7 cells were plated in

96-well microplate at a density of 25,000 or 5×10^4 cells/well, respectively, and incubated until

reaching 80% confluency. Cells were washed with PBS and different formulations of rHDL were

added at peptide concentrations of 10, 30, or 100 μg/mL for 18 h. After 18 h incubation, rHDL

was completely removed and cells were washed with PBS. Cells were then challenged with LPS

(2 ng/mL) for 18 h again. The quantification of NF-κB expression and pro-inflammatory cytokines

were obtained as described previously.

2.3.13. Co-incubation of rHDL and LPS in vivo

Female C57BL/6 mice were randomly assigned to six groups; Vehicle (PBS control group),

LPS, 22A-POPC, 22A-DMPC, 22A-DPPC, and 22A-DSPC, containing five mice each. Different

formulations of rHDL were pre-incubated with LPS for 30 minutes at 37°C prior to injection. The

mixtures were then administered via intraperitoneal injection (i.p.) with a final concentration of 10

mg/kg of rHDL and 0.05 mg/kg of LPS. All blood samples were collected from the jugular vein

in heparinized BD centrifuge tubes (Franklin Lakes, NJ) at 2 h post-administration. Serum samples

were separated immediately by centrifugation at 14,000 rpm for 10 minutes at 4°C and stored at -80°C until further analysis.

2.3.14. Effect of rHDL infusion on the endotoxemia mice

Female C57BL/6 mice were randomly assigned to six groups; Vehicle, LPS, 22A-POPC, 22A-DMPC, 22A-DPPC, and 22A-DSPC, containing ten mice each. Different formulations of rHDL were administered at a dose of 10 mg/kg via intravenous injection (i.v.). Subsequently, LPS (0.05 mg/kg, i.p.) was administered. Vehicle group was dosed with PBS (i.v.) then PBS (i.p.). The LPS control group was dosed with PBS (i.v.) followed by LPS (0.05 mg/kg, i.p.). All blood samples were collected from the jugular vein in heparinized BD centrifuge tubes (Franklin Lakes, NJ) at 2 h post-LPS challenge. Serum samples were separated immediately by centrifugation at 14,000 rpm for 10 minutes at 4°C and stored at -80°C until further analysis.

2.3.15. In vivo analysis of pro-Inflammatory mediators

The concentrations of inflammatory mediators, TNF-α, IL-6, and MCP-1 in the serum of LPS co-incubation study were quantified using eBioscience Ready-Set-Go ELISA (San Diego, CA) per manufacturer's instruction. The concentration of inflammatory mediators of TNF-α, IL-6, and MCP-1 in the serum of endotoxemia model was quantified using BD Cytometric Bead Array Mouse Inflammation Kit per manufacturer's instruction and analyzed. on Beckman Coulter CytoFLEX Flow Cytometer

2.3.16. Survival determination

Male C57BL/6 were randomly assigned into three groups, containing ten mice each; Vehicle, LPS, and 22A-DMPC. The vehicle group received PBS (i.p. and i.v.). The LPS group was first received LPS (10 mg/kg, i.p.). Once the anal temperature increased 0.5°C from LPS (approximately 15 min), PBS (i.v.) was administered. The 22A-DMPC group was first received LPS (10 mg/kg, i.p.). Again, once the anal temperature increased 0.5°C from LPS (approximately 15 min), 22A-DMPC (10 mg/kg, i.v.) was administered. The mice were then observed for mortality every 6 h and survival rates were recorded. Their lungs and livers were isolated collected for histological evaluation.

2.3.17. Tissue preparation

Tissues were fixed in 10% neutral buffered formalin for a minimum of 24 h. Histology preparation was performed by the Unit for Laboratory Animal Medicine In Vivo Animal Core at the University of Michigan. Briefly, tissues were cassetted and processed to paraffin on an automated processor, TissueTek VIP 6 from Sakura (Torrance, CA). Tissues were embedded in paraffin, sectioned at 4 µm thickness on a rotary microtome, and mounted on glass slides. Slides were stained with hematoxylin and eosin on an automated histostainer and coverslipped.

2.3.18. Histology evaluation and images

Histological sections were evaluated using light microscopy at magnifications ranging from 20x to 600x by a board-certified veterinary pathologist using an Olympus BX45 light microscope (Tokyo, Japan) Corporation). The evaluation was performed without knowledge of the experimental groups. Representative images were taken after histology analysis using an Olympus

DP73 microscope-mounted camera with associated software, Olympus cellSens v 1.18 (Tokyo, Japan). Images were processed into figures using Adobe Photoshop CC v 19.0. Image processing was confined to global adjustments of white balance, brightness, contrast, and sharpness that did not affect image interpretation. Histology was assessed based on standardized nomenclature/criteria for rodent hepatobiliary lesions (167) and literature descriptions of relevant histology in LPS challenge experiments (168–171).

2.3.19. Lethal-endotoxemia model optimization

Male C57BL/6 were randomly assigned into three groups, containing ten mice each, to determine the appropriate concentration of LPS for inducing lethal endotoxemia via a single i.p. injection of LPS (5 mg/kg, 10 mg/kg, and 20 mg/kg). The mice were then observed for mortality every 6 h for 4 days, and survival rates were recorded.

2.3.20. 22A-DSPC treatment survival determination

Male C57BL/6 were randomly assigned into three groups, containing ten mice each; Vehicle, LPS, and 22A-DSPC. The vehicle group received PBS (i.p. and i.v.). The LPS group was first received LPS (10 mg/kg, i.p.). Once the anal temperature increased 0.5°C from LPS (approximately 15 min), PBS (i.v.) was administered. The 22A-DSPC group was first received LPS (10 mg/kg, i.p.). Again, once the anal temperature increased 0.5°C from LPS (approximately 15 min), 22A-DSPC (10 mg/kg, i.v.) was administered. The mice were then observed for mortality every 6 h and survival rates were recorded. Their lungs and livers were collected for histological evaluation.

2.3.21. Statistical analysis

Statistical differences were compared with Student's t-test for comparing two groups or with one-way analysis of variance (ANOVA) with Tuckey's post-hoc test for comparing multiple groups. All samples were performed in triplicate unless noted otherwise. $P < 0.05$ was considered statistically significant. The Chi-square test was used to compare survival rates. Statistical analysis was performed using GraphPad Prism 7 (La Jolla, CA). Measurements are presented as means ± standard error of the mean unless indicated otherwise.

2.4.   Results

2.4.1.   Preparation and characterization of rHDL

rHDL were prepared by complexing apoA-I mimetic peptide, 22A, with various PCs (POPC, DMPC, DPPC, or DSPC) using a co-lyophilization procedure. Based on preliminary studies, the optimal weight ratio of peptide to phospholipid to result in homogenous preβ-like HDL is at 1:2 wt/wt peptide to phospholipid (172). To validate the morphology and confirm the preβ-like discoidal shape, each rHDL formulation was observed with TEM (**Figure 2.1A**). 22A-DMPC, 22A-DPPC, and 22A-DSPC were observed with typical discoidal morphology and were uniform in size. In contrast, 22A-POPC displayed heterogeneity in both size distribution and morphology. This is plausibly owing to the presence of liposomal impurities. These characteristics were further confirmed with DLS. We observed that the average diameters for 22A-POPC (13.7 ± 0.2 nm), 22A-DMPC (9.7 ± 0.2 nm), 22A-DPPC (11.2 ± 0.3 nm), and 22A-DSPC (12.2 ± 0.3 nm) were all within range of previously reported rHDL sizes (172,173) (**Table 2.1**). Analysis via GPC verified the observed size differences and the purity of rHDL (**Figure 2.1C**). All rHDL formulations resulted in a similar retention time of approximately 8 min (**Table 2.1**), with 22A-POPC exhibiting

a broader peak, indicating a more heterogeneous size distribution. The small peaks appearing at approximately 11 min represent free 22A peptide, accounting for less than 2% and considered negligible for all formulations.
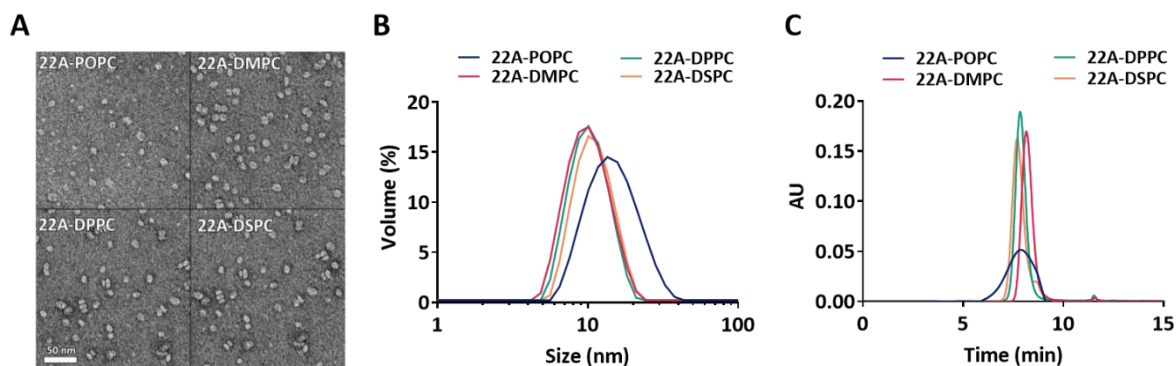
Figure 2.1. *Characterization of rHDL. A: Transmission electron microscopy image of different sHDL. B: Size distribution profile of different rHDL analyzed by dynamic light scattering. C: Size distribution and purity profile of different rHDL via gel permeation chromatography.*

Next, the T_m of each rHDL formulation was evaluated, as shown in **Table 2.1**. POPC is composed of 16:0/18:1 fatty acids, in which the unsaturated fatty acid causes a significantly low T_m (-3.3 ± 0.5°C) (174). When complexed with 22A, 22A-POPC had a observed T_m value of 0.5 ± 0.5°C. Similarly, DMPC is composed of 14:0/14:0 (T_m: 24.5°C) (175), DPPC is composed of 16:0/16:0 (T_m: 41.6°C) (175), and DSPC is composed of 18:0/18:0 (T_m: 54.5°C) (175). Once complexed with 22A to form rHDL, we observed rHDL T_m values of 27.0 ± 0.0°C, 45.4 ± 0.4°C, and 57.8 ± 1.3°C, respectively. A slight temperature rises from PC to rHDL is observed, possibly due to the addition of 22A peptide adding rigidity to the phospholipids. Based on T_m of each rHDL, 22A-POPC and 22A-DMPC are preferentially at the fluid and mobile liquid crystalline phase,

while 22A-DPPC and 22A-DSPC are at rigid and constrained gel phase at physiological temperature (37°C).

We further assessed the cytotoxicity of rHDL in multiple cell lines and none of the formulations exhibited cytotoxicity at concentrations up to 100 µg/mL (**Supplemental Figure 2.1**). Taken together, our results indicate the successful production of non-cytotoxic rHDL with preβ-like morphology and size.

Table 2.1. *Characterization Summary of rHDL.*

rHDL Formulation	RT (min)	Particle Size (nm)	Purity (%)	rHDL Tm (°C)
22A-POPC	7.9	13.7 ± 0.2	99.3 ± 0.1	0.5 ± 0.5
22A-DMPC	8.2	9.7 ± 0.2	99.2 ± 0.1	27.0 ± 0.0
22A-DPPC	7.8	11.2 ± 0.3	98.0 ± 0.8	45.4 ± 0.4
22A-DSPC	7.7	12.2 ± 0.3	99.2 ± 0.0	57.8 ± 1.3

The particle size of rHDL nanoparticles was analyzed by DLS; RT and purity were analyzed by GPC; and Tm of rHDL was analyzed by DSC (mean ± STD). RT: Retention Time, Tm: transition temperature

2.4.2. rHDL binding and neutralization of LPS

HDL can directly neutralize the TLR4-mediated inflammatory cascade by sequestering LPS in its phospholipid layer (57–59). To investigate whether rHDL made from different phospholipids could successfully neutralize LPS, a TLR4 ligand, by direct interaction, we analyzed the size-exclusion profile of rHDL after incubation with fluorescent LPS. As expected, all formulations of rHDL promoted a shift of LPS-Alexa 488 to rHDL molecular weight fraction, demonstrating successful binding of LPS to rHDL. (**Figure 2.2**).
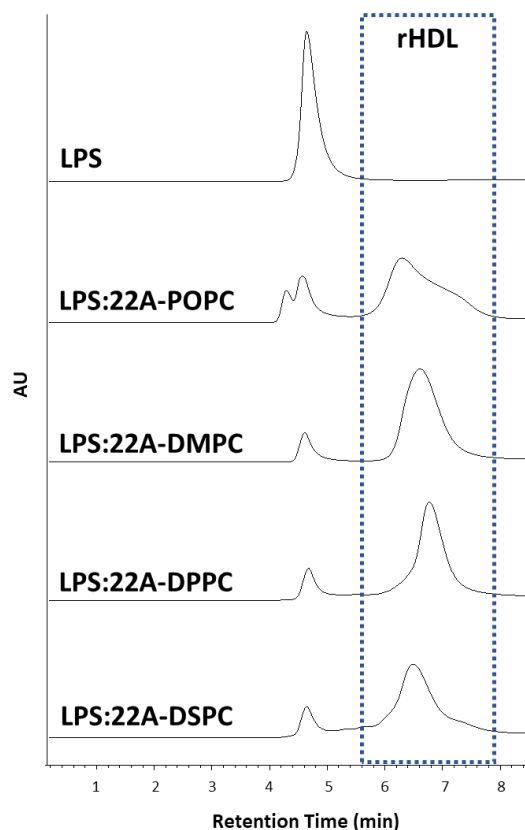
Figure 2.2. Absorbance profiles of fluorescent-LPS bound to rHDL. Fluorescent-LPS (10 µg/mL) and different formulations of rHDL (1 mg/mL) were mixed and incubated for 1 hour at 37 °C and the rHDL-LPS mixture was analyzed by HPLC with fluorescence detector. The blue dashed area represents the area in which rHDL present in UV absorbance.

2.4.3. Effect of rHDL lipids against LPS-induced inflammation in vitro

We next sought to evaluate how the ability of rHDL to sequester LPS could be translated to inhibition of inflammatory response, as TLR4 mediated recognition of LPS is thought to be one of the key triggers of the inflammatory response (45,46). To understand which formulations of rHDL most effectively modulate TLR4-mediated signaling, the HEK-Blue cell system was used to quantify the activity of NF-κB. HEK-blue hTLR4 cells were incubated with different rHDL at various concentrations (10, 30, and 100 µg/mL) in the presence of LPS (2 ng/mL). 22A-POPC and

42

22A-DMPC displayed significant concentration-dependent inhibition of NF-κB (P < 0.001) and inhibited NF-κB at all tested concentrations, 22A-DPPC inhibited activity at concentrations of 30 µg/mL and greater, and 22A-DSPC had no effect (**Figure 2.3A**). When comparing the two most potent inhibitors, 22A-POPC and 22A-DMPC, 22A-DMPC showed enhanced inhibition at all concentrations (P < 0.001).

We further examined the downstream TLR4-mediated inflammatory response by evaluating pro-inflammatory cytokine production. To do this, macrophages were incubated with rHDL at various concentrations in the presence or absence of LPS (2 ng/mL). Concentrations of TNF-α, IL-6, and MCP-1 in the media were quantified. 22A-POPC, 22A-DMPC, and 22A-DPPC effectively reduced LPS-induced pro-inflammatory mediators compared to controls (P < 0.001) and to 22A-DSPC ([#]P < 0.05) (**Figure 2.3B-D**). Here, we observed that fluid liquid crystalline phase 22A-DMPC resulted in the greatest inhibition of NF-κB activity and pro-inflammatory cytokine production. 22A-DPPC, although in the rigid gel phase, decreased the inflammatory response at the highest concentration as T_m is near physiological temperature, while 22-DSPC showed the least effective in LPS-induced inflammatory response modulation due to its limited fluidity making incorporating LPS into its phospholipid layer difficult.
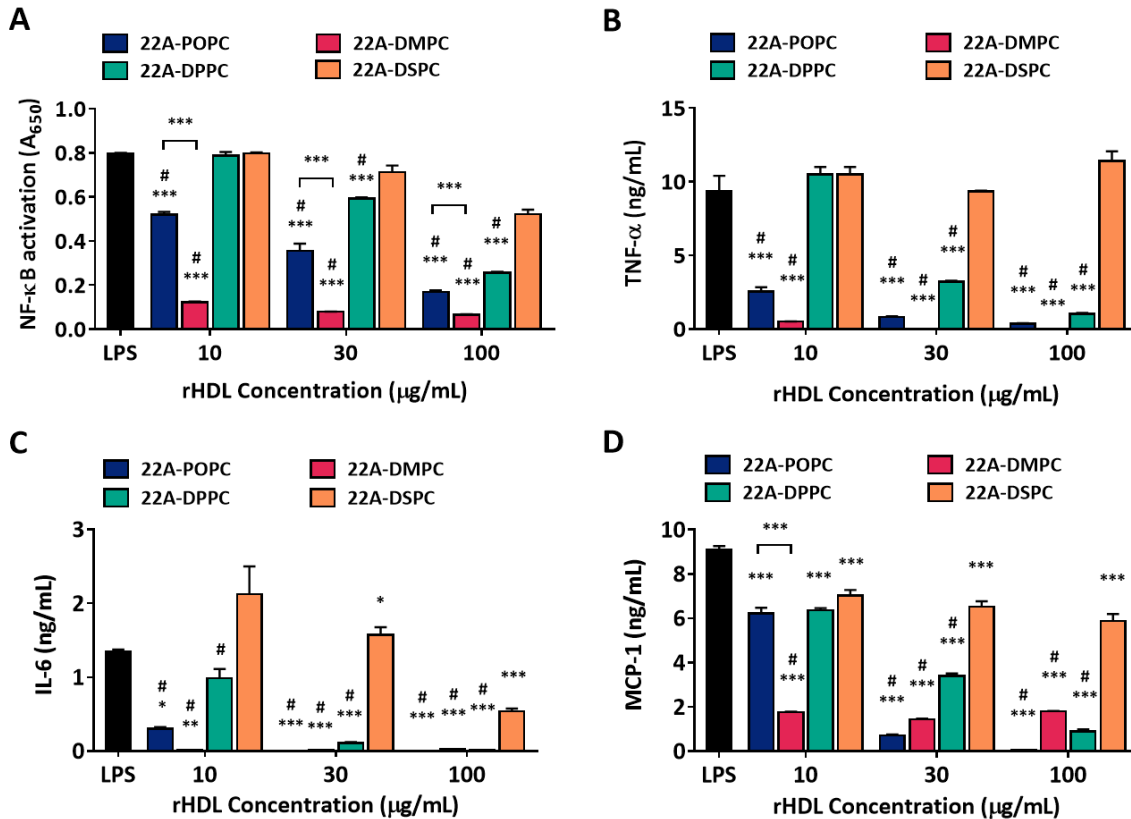
Figure 2.3. *Modulation of inflammatory response with different rHDL treatment. A: Activation of NF-kB of HEK-BLUE hTLR4 cells with treatment of different formulations and concentrations of rHDL in a presence of LPS (2 ng/mL). B-D: Concentration of TNF-α (B), IL-6 (C), and MCP-1 (D) of macrophages with treatment of different formulations and concentrations of rHDL in a presence of LPS (2 ng/mL). *P<0.05, **P < 0.01, ***P < 0.001 compared with LPS group; #P < 0.05 compared with 22A-DSPC group*

2.4.4. Effect of rHDL on TLR4 recruitment into lipid raft via cholesterol efflux

Lipid raft plays an important role in LPS-induced cellular activation. HDL promotes cholesterol efflux from macrophages via reverse cholesterol transport, compromising the integrity of lipid rafts as cholesterol is depleted leading to reduced lipid raft and TLR4 recruitment into lipid raft (4). First, to demonstrate whether rHDL could efflux cholesterol from macrophages, we incubated different rHDL (100 µg/mL) with [^{3}H]-cholesterol-loaded macrophages. 22A-DMPC

(61.8 ± 2.7%) exhibited the greatest cholesterol efflux, followed by 22A-POPC (57.2 ± 0.9%), 22A-DPPC (38.1 ± 1.4%), and 22A-DSPC (37.5 ± 1.9%) (**Figure 2.4A).** Given these results, we then examined the impact of rHDL-mediated cholesterol efflux on the alteration of lipid raft and TLR4 surface expression. Intriguingly, despite the significant cholesterol efflux observed from all rHDLs, none markedly reduced the lipid raft content, where only 22A-DMPC non-significantly reduced the lipid raft (90.1 ± 3.1%) (**Figure 2.4B**). However, minimal reduction of lipid rafts of 22A-DMPC was capable of a significant decrease of TLR4 recruitment on the cell surface (85.1 ± 4.5%) (**Figure 2.4C**). Overall, these results indicate that only 22A-DMPC was capable of inhibiting TLR4 recruitment into lipid raft via cellular membrane cholesterol depletion.
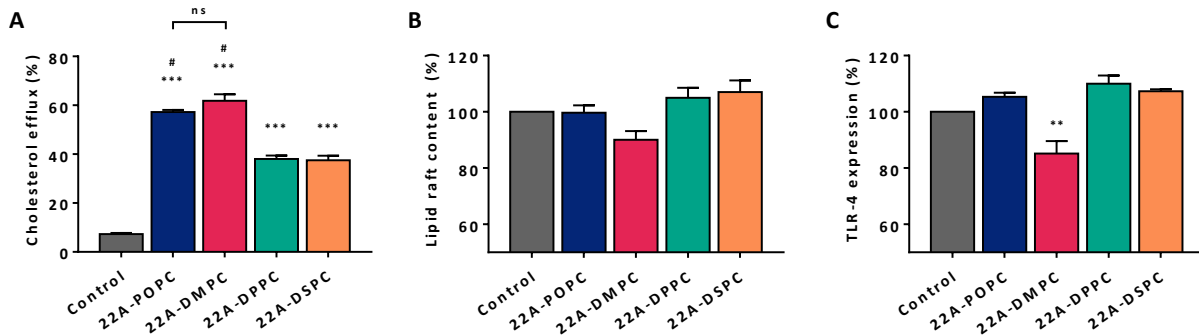
Figure 2.4. Disruption of lipid raft content and TLR-4 with rHDL. A: Relative quantification of cholesterol efflux from radio-labeled cholesterol-loaded macrophages with different formulations of rHDL (100 μg/mL) to the non-treated control group. Percentage cholesterol efflux from radio-labeled cholesterol-loaded macrophages was reported by liquid scintillation counting (n= 4, mean ± SEM). B-C: Relative measurement of lipid raft content of macrophages (B) and TLR4 expression (C) with different formulations of rHDL (100 μg/mL) to the non-treated control group. The percentage of lipid raft content and TLR4 expression was reported by the mean fluorescence intensity from flow cytometry. ns: not significant, *P<0.05, **P < 0.01, ***P < 0.001 compared with LPS group; #P < 0.05 compared with 22A-DSPC group

2.4.5. Effect of rHDL on ATF3 expression

ATF3 is a negative regulator of macrophage activation, acting as a negative-feedback system upon TLR4 activation to limit the excess production of pro-inflammatory cytokines (176,177). A few studies have shown that HDL can regulate the expression of TLR-induced pro-inflammatory cytokines on the transcriptional level via the transcriptional repressor ATF3 (5–7). To examine the ability of rHDL to promote ATF3 expression, we incubated macrophages with rHDL (100 µg/mL) and determined the mRNA and protein expression of ATF3. Notably, only 22A-DMPC induced *Atf3* mRNA expression significantly, increasing 5-fold in the first 1 h up to 21-fold after 4 h of incubation (P < 0.001), while 22A-POPC, 22A-DPPC, or 22A-DSPC had no effect (**Figure 2.5 A**). ATF3 protein expression was also examined by incubating macrophages with different rHDL for 18 h. Likewise, only 22A-DMPC induced prominent protein expression of ATF3, whereas expression was undetectable for the control group and other rHDL formulations (**Figure 2.5B**).
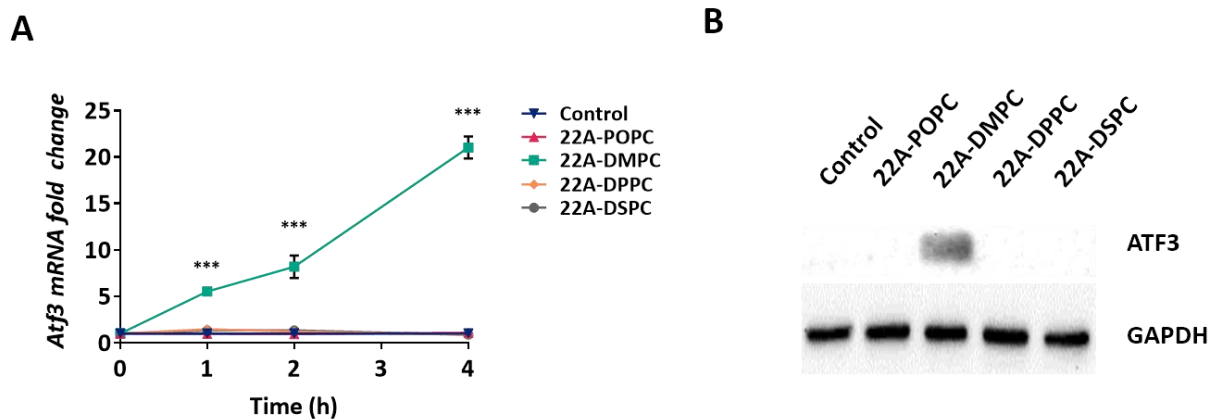
Figure 2.5. *The expression of ATF3 mRNA and protein with rHDL. A: Kinetics of ATF3 mRNA expression in macrophages with different formulations of rHDL (100 µg/mL) (n=9 ± SEM). B: ATF3 protein expression in macrophages by immunoblot with different formulations of rHDL (100 µg/mL) followed by 18 h incubation. ***P < 0.001*

2.4.6. Pre-treatment of rHDL against LPS-induced inflammation in vitro

Previous assessments revealed that among the different formulations of rHDL, only 22A-DMPC reduced TLR4 recruitment and promoted ATF3 expression. Here, we further demonstrated how these mechanisms can be elucidated to modulate the inflammatory response. Macrophages were incubated with different rHDL at various concentrations (10, 30, and 100 µg/mL). After 18 h incubation, rHDL was completely removed then cells were challenged with LPS (2 ng/mL) for 18 h again. When NF-κB expression was quantified from HEK-Blue hTLR4 cells, only 22A-DMPC showed significant inhibition in NF-κB expression in a dosage-dependent manner (P < 0.001) (**Figure 2.6A**). Similarly, when pro-inflammatory cytokines were measured from macrophages, again, only 22A-DMPC significantly altered TNF-α and IL-6 levels (P < 0.001) (**Figure 2.6B-C**). This study confirms that rHDL can promote anti-inflammatory activities not only through physical binding to LPS, but also through compromising lipid raft integrity to decrease TLR4 expression and promote ATF3 expression.
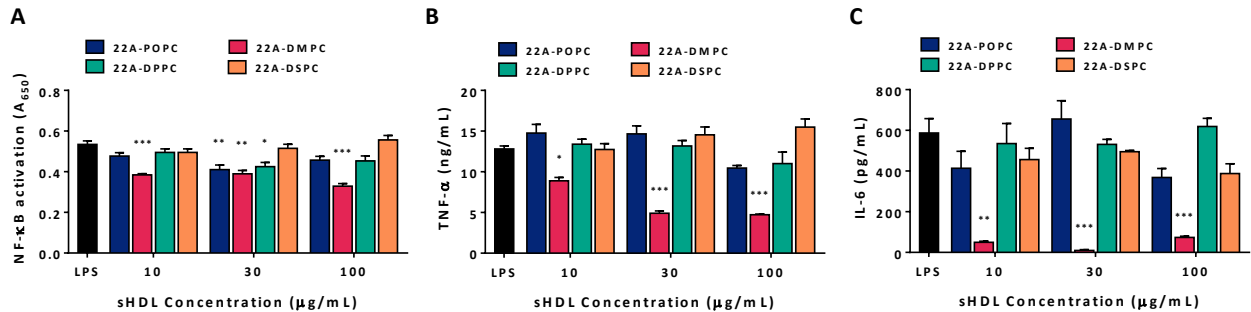
Figure 2.6. *Attenuation of inflammatory response with pretreatment of rHDL. A: Activation of NF-kB of HEK-BLUE hTLR4 cells. Cells were stimulated with 2 ng/mL of LPS after washing out the 18 h pre-treatment of different formulations and concentrations. B-D: Concentration of TNF-α (B), IL-6 (C), and MCP-1 (D) of macrophages. Macrophages were initially incubated with different formulations and concentrations of rHDL for 18 h, then rHDL were completely removed and stimulated with LPS (2 ng/mL). *P<0.05, **P < 0.01, ***P < 0.001*

2.4.7. *Effect of rHDL on LPS neutralization in vivo*

We examined whether LPS neutralization by rHDL effectively translates to modulation of the inflammatory response *in vivo* by administering pre-mixed LPS and rHDL solutions. Briefly, each rHDL was incubated with LPS for 30 min at 37°C and the mixture of each rHDL (10 mg/kg) and LPS (0.05 mg/kg) was administered to mice. When pro-inflammatory mediators including TNF-α, IL-6, and MCP-1 were analyzed at 2 h post-administration, all formulations of rHDL surprisingly suppressed their secretion (P < 0.001), however, no statistical differences were identified between the different rHDL formulations (**Figure 2.7**). This study strongly suggests that rHDL can effectively neutralize LPS-induced inflammatory activity by direct interaction.
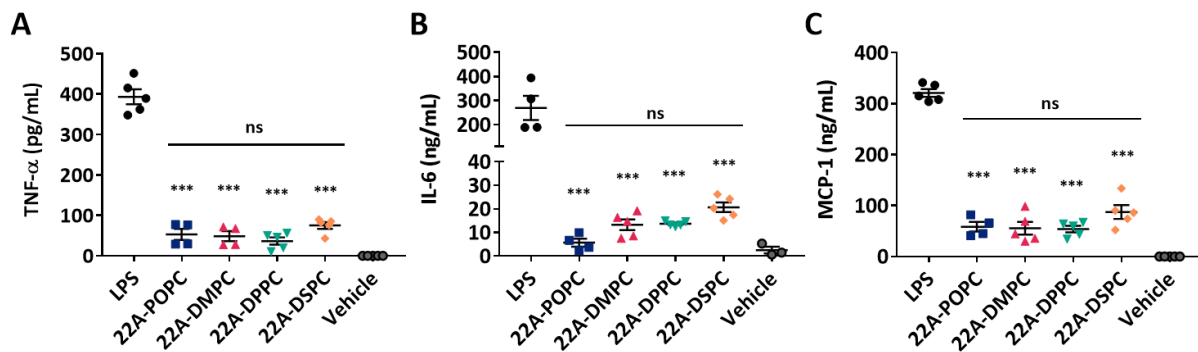
Figure 2.7. Serum cytokine levels post LPS-only or LPS-rHDL mixture administration. A-C: The LPS was incubated in the absence or presence of different formulations of rHDL for 30 min at 37°C. Experimental groups were with LPS-rHDL mixtures at 10 mg/kg of rHDL and 0.05 mg/kg of LPS. Blood was collected at 2 h post-administration and the concentrations of TNF-α (A), IL-6 (B), and MCP-1 (C) were measured (n=5). ns: not significant, ***P < 0.001

2.4.8. Effect of rHDL on LPS-induced endotoxemia mice

The ability of rHDL to elicit anti-inflammatory effect *in vivo* was examined in a murine endotoxemia model. Mice were initially administered with LPS (0.05 mg/kg) followed by different formulations of rHDL (10 mg/kg). 2 h post-LPS challenge, 22A-DMPC and 22A-DSPC caused a significant inhibition of TNF-α and IL-6 ($P < 0.01$ and $P < 0.001$, respectively), while 22A-DPPC resulted in a slight reduction of IL-6 ($P < 0.05$) and 22A-POPC had no effect (**Figure 2.8A-B**). In addition, 22A-DMPC and 22A-DSPC attenuated levels of MCP-1, although they were not statistically significant (**Figure 2.8C**). This study indicated that 22A-DMPC and 22A-DSPC were the only formulations able to effectively attenuate the inflammatory response in endotoxemia mice.
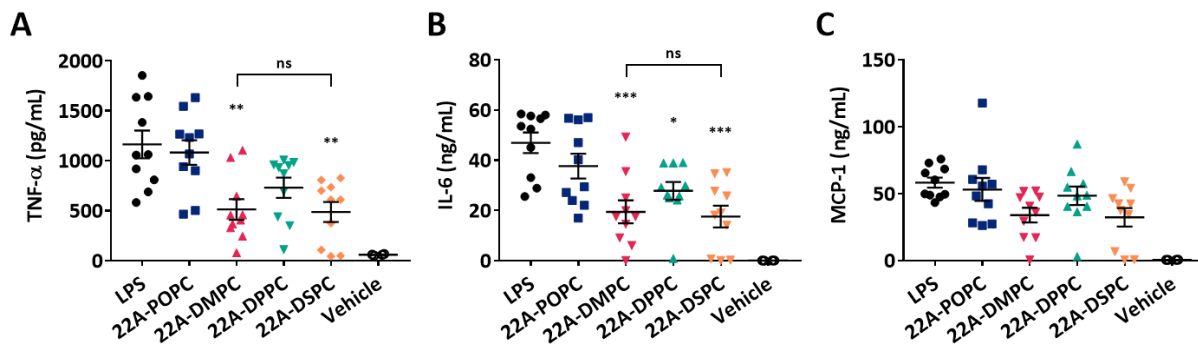
Figure 2.8. *Serum cytokine levels post rHDL administration from the endotoxemia model. A-C: Different formulation of rHDL was administered via intravenous injection at 10 mg/kg. Subsequently, LPS was challenged via intraperitoneal injection at 0.05 mg/kg. Blood was collected at 2 h post-administration and the levels of TNF-α (A), IL-6 (B), and MCP-1 (C) were measured (n=10). ns: not significant, *P<0.05, **P < 0.01, ***P < 0.001*

2.4.8. Effect of rHDL on lethal endotoxemia and organ injury

We further hypothesized that rHDL, especially 22A-DMPC, could improve the survival rate and protect organ injury from lethal endotoxemia, as it was observed to promote exceptional

anti-inflammatory activities *in vitro* and in mild endotoxemia mice. Once we determined the appropriate concentration of LPS for lethal endotoxemia (**Supplemental Figure 2.2**), mice were administered with a lethal endotoxin concentration of LPS (10 mg/kg). After the anal temperature had risen 0.5°c, mice were administered 22A-DMPC (10 mg/kg), and their survival was monitored for 4 days. As shown in **Figure 2.9** and **Table 2.2**, the survival in the 22A-DMPC treatment group drastically improved from 30% to 90% compared to the LPS-only group ($P < 0.01$). Additionally, the mean survival time in the 22A-DMPC treatment group prolonged dramatically from 53.4 ± 9.3 h to 93.6 ± 2.4 h relative to LPS-only treated animals ($P < 0.001$). There were no statistical differences observed between the 22A-DMPC group and the vehicle group.
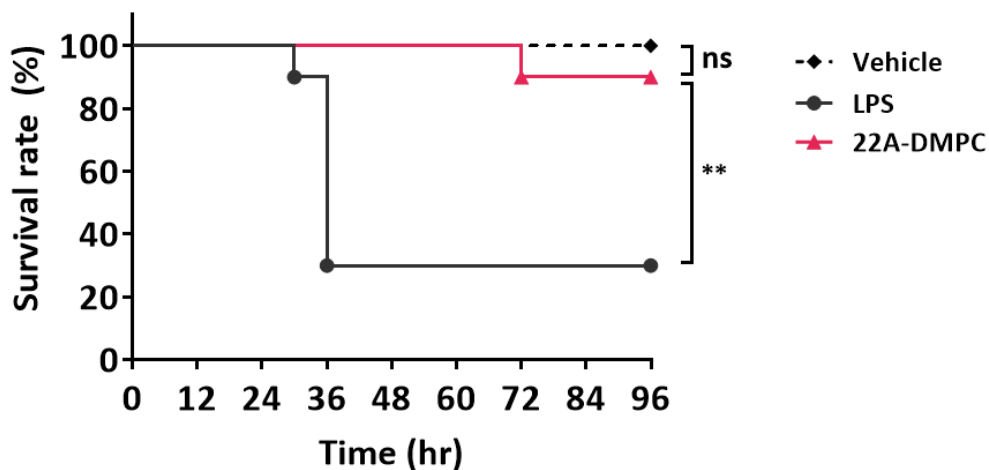
Figure 2.9. *The effect of 22A-DMPC treatment on LPS-induced lethality in mice. Mice were first challenged with LPS at 10 mg/kg (i.p.). After the anal temperature had risen 0.5°C (approximately 15 min), mice were administered PBS or 22A-DMPC at 10 mg/kg (i.v.). Survival was then monitored every 6 h for 96 h. Data show survival proportions (%) (n=10). **P < 0.01*

Table 2.2. *The treatment effect of 22A-DMPC rHDL in lethal endotoxemia mice.*

Group (n=10)	Survival rate (%)	Survival time (h)
LPS	30[**]	53.4 ± 9.3[***]
22A-DMPC	90[**]	93.6 ± 2.4[***]

**P > 0.01, ***P > 0.001

We further compared the relative severity of LPS-induced pulmonary and liver pathology in the rHDL treatment group and LPS group. As shown in **Figure 2.10** (liver), **Figure 2.11** (lung), and **Table 2.3**, the 22A-DMPC treatment group showed no alterations, no inflammatory infiltrations, and displayed similar pathology to the negative control group. In contrast, positive LPS controls had the greatest histological changes in both liver and lung, consisting of inflammatory cell infiltration in the liver and lung, hepatocyte degeneration, hepatic glycogen depletion, and hepatic extramedullary hematopoiesis of the myeloid lineage. These findings evidently indicate that rHDL, particularly 22A-DMPC, could protect endotoxemia mice from death and organ injury.
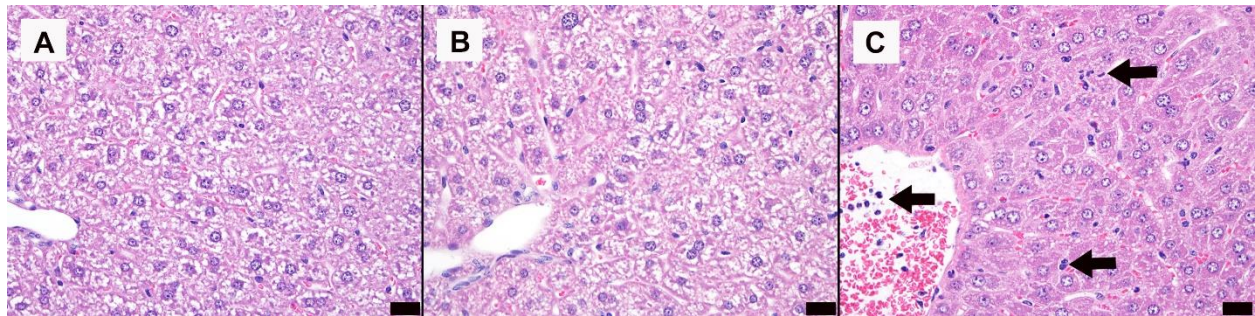
Figure 2.10. *Representative histologic images of the liver. A: Negative control group with normal levels of glycogen storage (evident as irregularly vacuolated hepatocytes) and no inflammatory infiltration. B: 22A-DMPC treatment group with the same appearance as control. C: LPS group with diffuse glycogen depletion (no hepatocyte vacuolation) and inflammatory cell infiltration within sinusoids and central venules (arrows). Original magnification 400x. Bars 20 µm.*
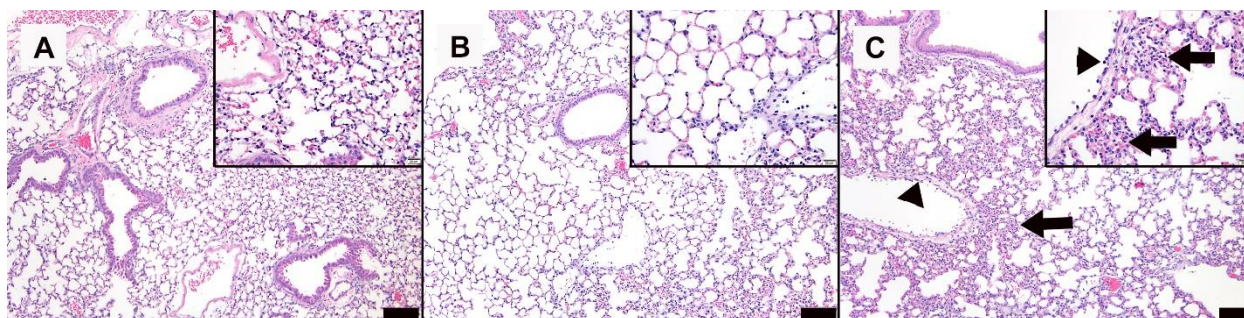
Figure 2.11. *Representative histologic images of the lung at low magnification overview (large image) and at higher magnification (insets). A: Normal lung in control showing open alveolar spaces separated by thin, delicate alveolar septae without interstitial expansion. B: Normal lung in the 22A-DMPC treatment group. C: Low level inflammatory cell infiltration evidenced as neutrophil emigration from pulmonary venules (arrowheads) and multifocal expansion of the interstitium by neutrophils and macrophages (arrows) (**C**). Original magnifications 100x (large image) and 400x (insets). Bars 100 µm (large image) and 20 µm (insets).*

Table 2.3. *Histology evaluation.*

Tissue	Finding	Severity scores of representative animals		
		Control	22A-DMPC	LPS
Liver	Infiltration, neutrophilic and macrophagic, sinusoidal	0	0	1
	Glycogen depletion	0	0	3
Lung	Infiltration, neutrophilic and macrophagic, interstitial and perivascular	0	1	2

Severity scores: 0 (not present); 1 (mild: few small foci or minimal density); 2 (moderate: multiple small foci or moderate density); 3 (severe: multiple larger or coalescing foci or regionally intense)

2.5. Discussion

In the present study, we extensively investigated how changes of phospholipids in rHDL can impact the anti-inflammatory activities in LPS-induced inflammation. We used PC that varies

in fatty acid chain length and saturation in the synthesis of rHDL, to display a unique fluidity of rHDL. The fluidity of the rHDL is known to be increased with the degree of the unsaturated fatty acid moieties (58). To this extent, HDL containing polyunsaturated saturated fatty acids (PUFA) would exhibit more fluid PC phase and result in enhanced anti-inflammatory activities by accelerating the efflux of cell-derived pro-inflammatory lipids, LPS, and cholesterol. However, our studies demonstrated that the rHDL with T_m closer to physiological temperature, 22A-DMPC resulted in the most enhanced anti-inflammatory activity in various mechanisms including LPS neutralization, cholesterol efflux, reduced TLR4 recruitment, and induced ATF3 expression to promote the greatest anti-inflammatory from fluid and mobile 22A-DMPC.

We first analyzed NF-κB, pro-inflammatory mediators quantify the capability of each rHDL to neutralize LPS and modulate inflammatory signaling cascade. 22A-DMPC notably suppressed NF-kB expression and pro-inflammatory mediators followed by 22A-POPC, 22A-DPPC, and 22A-DSPC (**Figure 2.3**). According to PUFA residues (26,178), 22A-POPC exhibits the greatest fluidity and expected to result in the greatest LPS neutralization, nevertheless, 22A-DMPC led to the greatest LPS neutralization. When 22A-DMPC, 22A-DPPC, and 22A-DSPC are compared, the LPS neutralization capability was correlated to the fatty acid chain length of PC as it affected the fluidity of rHDL. However, LPS neutralization capability between 22A-POPC and 22A-DMPC did not follow the degree of the fluidity and the difference could be potentially explained by the stability of rHDL. We believe that heterogeneous size distribution in 22A-POPC is possibly due to the presence of liposomal impurities. The difficulty of synthesizing pure 22A-POPC was described previously and was attributed to fluidity and instability of phospholipid membrane at room temperature which is above POPC T_m (179). In addition, the presence of an unsaturated fatty acid chain could result in phospholipid oxidation and oxidized HDL has been

reported with less fluidity (180,181). The instability and reduced fluidity of 22A-POPC would have caused reduced LPS neutralization capability. 22A-DMPC, in contrast, exhibits fluid liquid crystalline phase yet is relatively stable at physiological temperature since its T_m was close to physiological temperature. Biophysical characterizations should be further investigated to validate the fluidity of each rHDL through changes in fluorescence polarization anisotropy and how the fluidity influences the interaction with LPS.

Next, we sought to explore the disruption of lipid raft integrity, thereby decreasing TLR4 on the surface of the cell as TLR4 presentation is localized within lipid rafts. Numerous studies have reported differences in cholesterol efflux capability for PCs of different saturation and fatty acid chain length. For example, saturated long-chain phospholipids such as DPPC and DSPC have higher cholesterol efflux capabilities and higher physical binding affinity to cholesterols than POPC (30,31,182,183). Our result was marginally in discordance with previous reports, as we focused on the fluidity of rHDL rather than physical cholesterol binding affinity. Analogous to our LPS binding results, we observed the greatest cholesterol efflux capacity from 22A-DMPC followed by 22A-POPC, and the least capacity from 22A-DPPC and 22A-DSPC based on its fluidity to efflux cholesterol.

Despite the significant cholesterol depletion observed with 22A-DMPC, it did not notably reduce the lipid raft content. Nevertheless, the modest lipid raft reduction was sufficient to result in a significant decrease of TLR4 recruitment on the cell surface (**Figure 2.4**). Murphy *et al.* performed a similar study examining the change in human monocyte lipid raft content, however, they observed a dramatic reduction of lipid raft content with apoA-I treatment (184). Several past studies reported that reduction of lipid raft cholesterol occurs through ABCA1 which is a key transporter that primarily interacts with apoA-I to efflux cholesterol from macrophages (4,185).

Therefore, one explanation for why the high cholesterol efflux from 22A-DMPC did not translate to a dramatic decrease in lipid rafts is that 22A-DMPC was initiating cholesterol efflux through another transporter, such as ATP-binding cassette transporter G1 (ABCG1), scavenger receptor B type I (SR-BI), or by passive diffusion. ABCG1 transporters interact with mature HDL to efflux cholesterol while SR-BI transporter is located in the caveolar region of macrophage and promotes bidirectional cholesterol efflux. Validation of 22A-DMPC or other rHDL transporter-specific efflux in macrophages would explain the relative minimal lipid raft disruption compared to the dramatic observed cholesterol efflux capacity.

We also showed stimulation of ATF3 expression by rHDL, consistent with initial reports by De Nardo *et al.* (5), and further demonstrated that the expression of ATF3 is critically dependent on rHDL phospholipid composition. Activation of ATF3 leads to recruitment of histone deacetylase 1 to the promoter region of pro-inflammatory cytokine gene and assists in deacetylating to limit transcriptional binding (68,69). In addition, a recent study demonstrated that ATF3 can directly interact with the p65 subunit of NF-κB to attenuate the NF-κB activity, thus, modulate the inflammatory response, rather than via indirect histone deacetylase 1 pathway (70). We demonstrated that 22A-DMPC induced prominent expression of ATF3 mRNA and protein while other rHDLs had no effect (**Figure 2.5**). Several studies also explored how structural differences in HDL can impact ATF3 expression. Didchenko *et al.* confirmed the finding that large rHDL has a reduced ability to induce ATF3 and smaller rHDL have a strong ability to induce both anti-inflammatory phenotypes and ATF-3 expression in macrophages (186). Similarly, Wang *et al.* found that various apoA-I cysteine mutants of rHDL can cause altered ATF3 expression, as amino acid mutations can influence the ATF3 pathway in macrophages (6). The mechanism by which HDL activates ATF3 is still unclear, but it is well-recognized as a key inflammatory

modulator of HDL. We propose that rHDL phospholipid composition and fluidity of rHDL can also influence the ATF3 pathway in macrophages causing altered expression of ATF3.

Interestingly, we were surprised by the results from our *in vivo* endotoxemia model (0.05 mg/kg LPS) with rHDL administration (10 mg/kg). While we expected to see enhanced suppression of inflammatory response from the 22A-DMPC group due to its promising results *in vitro*, we did not expect that the 22A-DSPC group would also show a prominent suppression of the inflammatory response (**Figure 2.8**). *In vitro* 22A-DSPC was the least effective among all rHDL treatments, and we believe that 22A-DSPC efficacy in the endotoxemia model owes to its exceptional half-life. The half-life of 22A-DSPC was nearly 2-fold longer than 22A-DMPC, observed from a pharmacokinetic study (in revision, JPET), which may have allowed for greater exposure and neutralization of LPS (187). A credible explanation is that rHDL is known to be dissociated and remodeled upon administration *in vivo* (173,188), thus, 22A-DSPC favorably remodeled at a slower rate due to its rigid gel phase phospholipid compared to the fluid liquid crystalline phase phospholipid of 22A-DMPC (in revision, JPET). Nevertheless, the prolonged circulation of 22A-DSPC did not translate to a decrease in LPS-induced inflammation or an increase in survival following lethal doses of LPS (**Supplemental Figure 2.3**). Conversely, the efficacy of 22A-DMPC was further demonstrated in a lethal endotoxemia model which increased the survival rate and time (**Table 2.2**) along with the prevention of inflammation-induced organ injury (**Table 2.3**).

In 1993, Levine *et al.* reported that rHDL (80 mg/kg) composed with 18A peptide and egg PC could improve the survival rate 3- to 4-fold in endotoxemia mice (10 mg/kg LPS) and suggested the simple leaflet insertion model for neutralization of LPS by phospholipid on the surface of HDL (59). Imai *et al.* found that administration of apoA-I (10 mg/kg) 2 h post-LPS injection (1 mg/kg

LPS) reduces plasma TNF-α and increased the survival rate in endotoxemia rats (5 mg/kg). Similarly, Yan *et al.* demonstrated the administration of apoA-I (100 mg/kg) to endotoxemia mice (5 mg/kg LPS) significantly lowered mortality (159). Zhang *et al.* used rHDL (40 mg/kg) complexed with apoA-I Milano, a mutant apoA-I, with soy PC as a treatment in endotoxemia rats (400 EU/kg gram-negative bacteria endotoxin) and observed improvements in renal and hepatic functions as well as a reduction in pro-inflammatory cytokines (160). In addition, Wang *et al.* compared the anti-inflammatory effect of rHDL containing different apoA-I cysteine mutants in endotoxemia mice, suggesting the cysteine mutation can impact LPS neutralization capability (189). The results from our study are consistent with these previous findings, with rHDL exerting efficacy against LPS-induce endotoxemia by inhibiting pro-inflammatory mediators and improving the survival rate in endotoxemic mice. Moreover, we proposed the importance of rHDL phospholipid composition which influences the mechanisms of anti-inflammatory activities in LPS-induced inflammation.

In conclusion, for the first time, we demonstrate that phospholipid composition drastically alters the anti-inflammatory effect of rHDL on LPS-induced inflammation both *in vitro* and *in vivo*. Our data suggest that fluidity of rHDL due to structural variances of phospholipids critically determines the anti-inflammatory effect by promoting different anti-inflammatory mechanisms. In this study, 22A-DMPC exhibited the most fluid yet stable rHDL at physiological temperature, displaying the greatest anti-inflammatory activities through multiple mechanisms including LPS neutralization, disruption of lipid raft integrity, and activation of ATF3 *in vitro* but also protected mice against mortality and organ injury from lethal endotoxemia. Therefore, we suggest that 22A-DMPC may be a potential therapeutic effect against LPS-induced sepsis.

2.6.   Supplemental Information

57
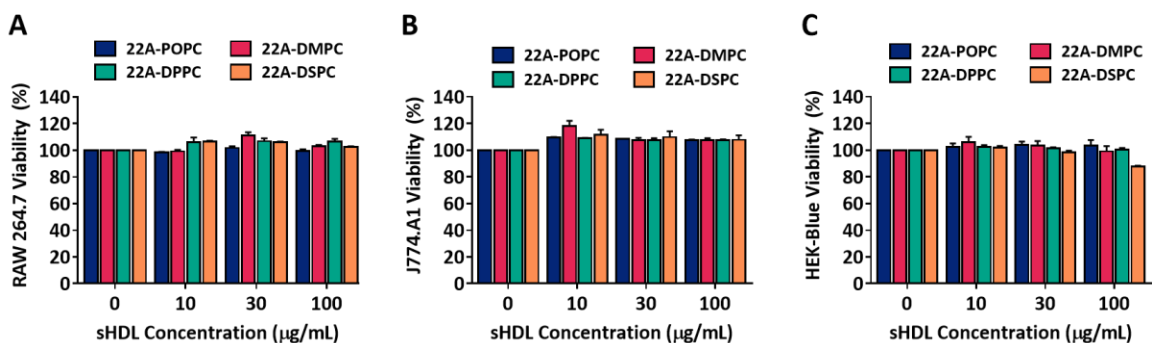
Figure 2.12. *Cell viability with rHDL treatment. A-C: Viability of Raw 264.7 (A), J774A.1 (B), HEK-Blue hTLR4 (C) cells with incubation of different formulations and concentrations rHDL for 18 h.*
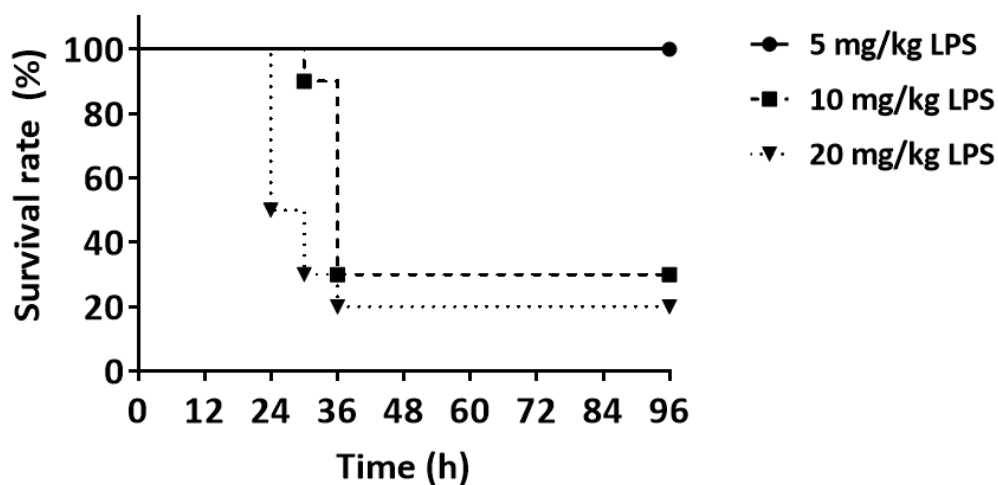
Figure 2.13. *Survival rate (%) of mice challenged with LPS of different doses. Mice were injected with 5, 10, or 20 mg/kg of LPS (i.p.) without any treatment with 22A-sHDL (**A**). Mice were divided into control, LPS (10 mg/kg) only and LPS (10 mg/kg) + 22A-DMPC (10 mg/kg) treatment groups. After the anal temperature had risen 0.5°c, mice were either treated with saline or 22A-DMPC (**B**). Survival was then monitored every 6 hr for 4 days. Data show survival proportions (%) (n=10). **P < 0.01*
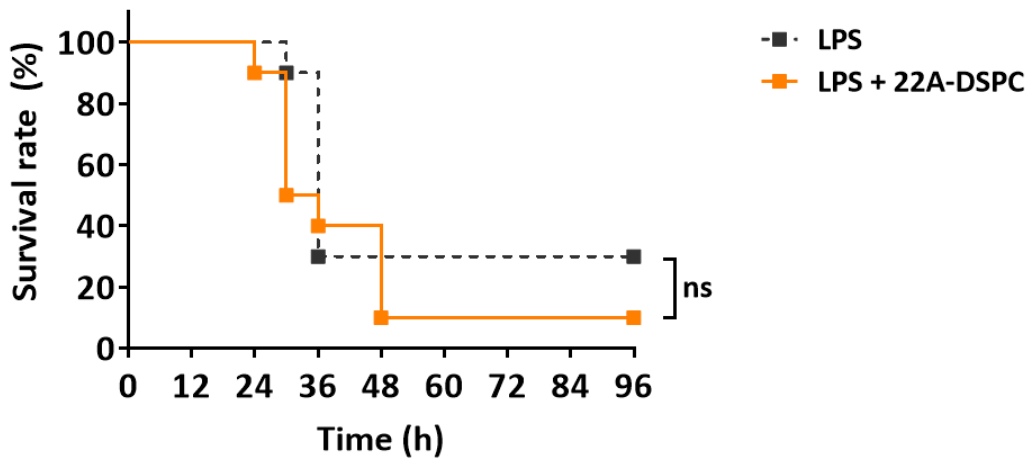
Figure 2.14. *The effect of 22A-DSPC treatment on LPS-induced lethality in mice. Mice were challenged with LPS via at 10 mg/kg (i.p.). After the anal temperature had risen 0.5°C (approximately 15 min), mice were administered in the absence or presence of 22A-DSPC at 10 mg/kg (i.v.). Survival was then monitored every 6 h for 96 h. Data show survival proportions (%) (n=10). **P < 0.01*

Chapter 3

Phospholipid Component Defines Pharmacokinetic and Pharmacodynamic Properties of Synthetic High-Density Lipoproteins

3.1. Abstract

Synthetic high-density lipoprotein (sHDL) nanoparticles composed of apolipoprotein A-I (ApoA-I) mimetic peptide and phospholipids have been shown to reduce atherosclerosis in animal models. Cholesterol is mobilized from atheroma macrophages by sHDL into the blood compartment and delivered to the liver for elimination. Historically, sHDL drug discovery efforts were focused on optimizing peptide sequences for interaction with cholesterol cellular transporters rather than understanding how both sHDL components, peptide and lipid, influence its pharmacokinetics (PK) and pharmacodynamic (PD) profiles. We designed two sets of sHDL having either identical phospholipid but variable peptide sequences with different plasma stability, or identical peptide and phospholipids with variable fatty acid chain length and saturation. We found that sHDL prepared with proteolytically stable 22A-P peptide had 2-fold longer circulation half-time relative to the less stable 22A peptide. Yet, longer half-life did not translate into any improvement in cholesterol mobilization. In contrast, sHDL with variable phospholipid compositions showed significant differences in phospholipid PK, with distearoyl phosphatidylcholine-based sHDL demonstrating the longest half-life of 6.0 h relative to 1.0 h for palmitoyl-oleoyl phosphatidylcholine-based sHDL. This increase in half-life corresponded to a ~6.5-fold increase in the area under the curve for the mobilized cholesterol. Therefore, the

60

phospholipid component in sHDL plays a major role in cholesterol mobilization *in vivo* and should not be overlooked in the design of future sHDL.

3.2.   Introduction

Reverse cholesterol transport (RCT) is a mechanism of cholesterol removal from the periphery to the liver for elimination. This transport starts when lipid-poor apolipoprotein A-I (ApoA-I) facilitates extracellular efflux of phospholipids and cholesterol through the transmembrane ATP-binding cassette transporter A1 (ABCA1) resulting in the formation of pre-β high-density lipoprotein (HDL) particles. Then, pre-β HDLs interact with lecithin:cholesterol acyltransferase (LCAT), an enzyme responsible for cholesterol esterification, leading to the formation of larger mature HDLs. Mature HDLs can either deliver esterified cholesterol (EC) cargo directly to the liver for elimination through scavenger receptor class B type I (SR-BI) or transfer EC to LDL by interaction with cholesterol ester transfer protein (CETP) for the elimination by the liver following LDL receptor-mediated uptake.

The idea of using reconstituted (rHDL) or synthetic (sHDL) HDL for the treatment of cardiovascular disease has been prominent in the past 20 years, with several therapies reaching clinical trials (190–193). While some clinical trials for rHDL products were successful (190,191,193), others failed (194,195). A 17,400-patient Phase III trial (AEGIS-II) is currently ongoing for CSL-112 to show a possible reduction of major adverse cardiovascular events in subjects with the acute coronary syndrome (193). The two most advanced sHDL products, CSL-112 and CER-001, both contain ApoA-I but differ in their lipid composition. CSL-112 is prepared from unsaturated soybean phosphatidylcholine while CER-001 is composed of primarily saturated sphingomyelin (195). Recently, we have shown that the type of phospholipid used in sHDL

preparation is critical for its anti-inflammatory and anti-atherosclerotic properties (188). Several other studies had examined the effects of phospholipid composition on the ability of sHDL to efflux cholesterol and interact with LCAT *in vitro* (31,196,197), yet the impact of phospholipid chain length and saturation on sHDL pharmacodynamics *in vivo* has not been systematically examined.

In contrast, a significant body of research had been performed to develop short peptides (2F (18A), D-4F, L-4F, 5A, 22A, and ATI-5261) as cost-efficient, safe and easily scalable alternatives to a full-length ApoA-I (128,130,139,166,198–201). These ApoA-I mimetic peptides have been optimized with the goal to improve several properties such as ABCA1 mediated cholesterol efflux, the ability to activate LCAT and facilitate cholesterol esterification, enhance anti-oxidant properties, improve chemical stability and reduce hemolytic side-effects (43,131,140,199). Most ApoA-I mimetics were optimized as "naked" or lipid-free peptides *in vitro* and *in vivo* and only a few studies examined the pharmacological activity of peptide-based sHDL (131,172).

Thus, we decided to systematically evaluate the effect of both peptide sequence and phospholipid composition of sHDL on nanoparticle's ability to mobilize and esterify cholesterol *in vitro* and *in vivo*. For our studies, we used the first ApoA-I mimetic peptide (22A) that reached clinical trials as part of the sHDL product called ETC-642 (127,166). ETC-642 contained 22A ApoA-I mimetic peptide, which was optimized for its ability to bind phospholipids and activate LCAT (135,199). While ETC-642 successfully completed single and multiple-dose trials in dyslipidemia patients, it was recently discovered by us that 22A peptide undergoes rapid hydrolysis in plasma to form the 21A peptide, which lacks the C-terminal lysine, a residue potentially important for LCAT activation (172,202). We hypothesized that the addition of a

proline moiety after the labile lysine (22A-P) would be able to protect 22A from proteolysis and result in longer circulation time while retaining LCAT activity *in vivo*. Thus, we prepared a set of sHDL particles using 22A, 21A, and 22A-P peptides while keeping lipid composition constant.

The second set of sHDL was prepared by varying only the phospholipid component and keeping the peptide component, 22A, constant. We used phospholipids with different chain length and saturation including 1-palmitoyl-2-oleoyl-sn-glycero-3-phosphocholine (POPC), 1,2-dimyristoyl-sn-glycero-3-phosphocholine (DMPC), 1,2-dipalmitoyl-sn-glycero-3-phosphocholine (DPPC) or 1,2-distearoyl-sn-glycero-3-phosphocholine (DSPC) known for their differences in cholesterol binding affinity and LCAT interaction (182,203,204). Phospholipids with longer, saturated fatty acid chains such as DPPC and DSPC have a higher affinity for cholesterol binding and higher physical stability due to their high transition temperatures (T_m) of 41°C and 55°C, respectively (182,183,205). In contrast, unsaturated phospholipids like POPC (T_m= -2°C) and those with shorter fatty acid chains like DMPC ($T_m = 23$°C) form fluid bilayers at physiological temperature facilitating LCAT-sHDL binding. The unsaturated fatty acids are superior substrates for LCAT esterification activity (203,206). By comparing two sets of sHDL with varying peptide and lipid components side by side, we expected to be able to elucidate the relative contribution of both components to cholesterol efflux and engagement of LCAT *in vitro* as well as the overall pharmacokinetic and pharmacodynamic behavior of sHDL *in vivo*.

3.3. Materials and Methods

3.3.1. Materials

22A (PVLDLFRELLNELLEALKQKLK), 21A (PVLDLFRELLNELLEALKQKL), and 22AP (PVLDLFRELLNELLEALKQKLKP) were synthesized by Genscript (Piscataway, NJ),

using solid-phase Fmoc (9-fluorenylmethyl carbamate) protection chemistry and purified with reverse phase chromatography (>95% pure). 5A peptide (DWLKAFYDKVAEKLKEAF-P-DWAKAAYDKAAEKAKEAA) was obtained from Bachem Americas Inc (Torrance, CA). Phospholipids including 1,2-dimyristoyl-*sn*-glycero-3-phosphocholine (DMPC), 1,2-dipalmitoyl-*sn*-glycero-3-phosphocholine (DPPC), 1,2-distearoyl-*sn*-glycero-3-phosphocholine (DSPC), and 1-palmitoyl-2-oleoyl-*sn*-glycero-3-phosphocholine (POPC) were purchased from NOF America Corporation. Ergosta-5,7,9(11), 22-tetraen-3β-ol (dehydroergosterol, DHE), cholesterol oxidase was obtained from Sigma-Aldrich (St. Louis, MO). Cholesterol (1,2-^{3}H(N)] was purchased from Perkin Elmer. Anti-human ApoA-I horseradish peroxidase-conjugated (HRP) antibody (1:1000 dilution) was purchased from Meridian Life Science (Memphis, TN). Recombinant human lecithin cholesterol acyl transferase (LCAT) was kindly provided by MedImmune (Gaithersburg, MD). All other materials were obtained from commercial sources.

3.3.2. Preparation and characterization of synthetic high-density lipoproteins

sHDL composed of a peptide (22A, 21A, or 22A-P) and phospholipid (DMPC, POPC, DPPC, or DSPC) were prepared by a co-lyophilization procedure (188). Briefly, peptide and phospholipids were dissolved in glacial acetic acid, mixed at 1:2 w/w ratio of peptide:lipid, and lyophilized overnight. The powder was hydrated with PBS pH 7.4 to make 10 mg/mL sHDL and cycled between 55°C (10 min) and room temperature (10 min) to facilitate sHDL formation. The resulting sHDL complexes were analyzed by gel permeation chromatography for purity at 1 mg/mL using 7.8 mm x 30 cm Tosoh TSK gel G3000SWxl column (Tosoh Bioscience, King of Prussia, PA) with UV detection at 220 nm. The HDL hydrodynamic diameters were determined by dynamic light scattering (DLS) using a Zetasizer Nano ZSP, Malvern Instruments

(Westborough, MA). The volume intensity average values were reported. The α-helical content of free and lipid-bound peptide was determined by Jasco J715 (Jasco, Easton, MD) circular dichroism (CD) spectropolarimeter. Samples at 0.1 mg/mL concentration in 10 mM phosphate buffer (pH 7.4) or buffer alone were loaded into a quartz cuvette (d = 0.2-cm path length), and CD spectra from 190 to 260 nm were recorded at 37°C. Buffer spectra were subtracted from each peptide or sHDL sample. Data analysis was conducted using CDPro analysis software and the percent helical content for each sample was calculated via CONTIN analysis method with the reference Soluble–Membrane Protein 56 Data Base (207).

3.3.3. *Generation of helical wheel peptide models and calculation of lipid binding parameters*

Helical wheel plots of 22A, 21A, and 22A-P peptides were created by Helixator (http://tcdb.org/progs/helical_wheel.php). This program displayed a peptide sequence looking down the axis of the alpha helix with aliphatic residues shown as blue circles. The hydrophobic momentum of 22A, 21A, and 22A-P peptides was calculated using the 3D Hydrophobic Moment Vector Calculator (http://www.ibg.kit.edu/HM/) (208). The helix stability (ΔG_{hel}), transfer energy from water to membrane (ΔG_{trans}), and parameters of spatial positions in membranes (tilt angle and membrane penetration depth) for each ApoA-I-mimetic peptide were calculated by the Folding of Membrane-Associated Peptide (FMAP) server (209) and the Positioning of Proteins in Membranes (PPM) server (210).

3.3.4. *Cholesterol efflux assay in vitro*

Cholesterol efflux studies were performed, as described by Remaley *et al*. (211). Briefly, RAW 264.7, BHK-Mock and BHK stably transfected with human ABCA1 cDNA cell lines were

labeled for 24 h with 1 μCi/mL of [^{3}H] cholesterol in minimum Dulbecco's modified Eagle's medium (DMEM), containing 0.2 mg/ml of fatty acid-free bovine serum albumin (BSA). Then, BHK-MOCK and BHK-ABCA1 cell lines were treated with 10 nM mifepristone for 18 h to selectively induce the expression of ABCA1 cholesterol transporter for BHK-ABCA1. ABCA1 transporter was not selectively induced in RAW 264.7 cell line. Following the radiolabeling or induction step, peptides (22A, 21A or 22A-P) or sHDL (21A-DMPC, 22A-P-DMPC, 22A-DMPC, 22A-POPC, 22A-DPPC or 22A-DSPC) were added at 0.01, 0.03 and 0.1 mg/mL concentration using DMEM-BSA media. After 18 h of incubation with cholesterol acceptors, media were collected and cells were lysed in 0.5 ml of 0.1% SDS and 0.1 N NaOH for 2 h. Radioactive counts in media and cell fractions were measured by liquid scintillation counting (Tri-Carb 2910 TR, PerkinElmer), and percent cholesterol efflux was calculated by dividing media counts by the sum of media and cell counts.

3.3.5. *Phospholipid lipolysis by LCAT*

The rate of phospholipid (POPC, DMPC, DPPC or DSPC) lipolysis was evaluated by incubating 15 μg/mL of rhLCAT with 0.1 mg/mL of sHDL (based on total lipid concentration) in 0.1 M sodium phosphate buffer pH 7.4 for 0, 5, 15, 30, 60, 90, and 120 min. The LCAT-sHDL reaction aliquots were collected into methanol (1:5 v/v) and vortexed to stop the lipolysis reaction at each time point. The amount of POPC, DMPC, DPPC or DSPC remaining at each time point was measured by Waters UPLC-MS equipped with QDa Mass Detector (Milford, MA). Chromatographic separation was achieved on Acquity BEH300 1.7 μm HILIC 2.1 x 50 mm column with gradient elution at 0.65 mL/min: mobile phase A (H$_2$O/0.1% formic acid), mobile phase B (acetonitrile/0.1% formic acid) and mobile phase C (100 mM ammonium formate) as

follows: 0-0.7 min (5-17% A, 90-78% B, and 5-5% C), 0.7-0.71 min (17-5% A, 78-90% B, and 5-5% C), and 0.71-3 min (17-5% A, 78-90% B, and 5-5% C). Mass spectra were acquired in the positive ion mode with the mass range set at m/z 150-1250 and POPC was detected at 760.7 amu, DMPC at 678.7 amu, DPPC at 734.7 amu, and DSPC at 790.7 amu. Data analysis was performed with Waters Empower software. The plot of POPC, DMPC, DPPC or DSPC area under the curve over time was generated for each sHDL sample. The rate of LCAT lipolysis (k) was calculated from the linear slope of the log10 (concentration) versus time.

3.3.6. *Cholesterol esterification by LCAT assay*

Two different sets of sHDL containing dehydroergosterol (DHE) was prepared via the thin-film method. Briefly, the first set was made from POPC, DPPC and DHE combined at a 4.5:4.5:1 molar ratio in chloroform and then mixed with peptide (22A, 21A or 22A-P) at 2:1 lipid:peptide weight ratio in methanol/water (4:3 v/v). The second set was prepared from POPC, DMPC, DPPC or DSPC and DHE at a 9:1 molar ratio then mixed with 22A peptide at 2:1 lipid:peptide weight ratio in methanol/water (4:3 v/v). The solvent was removed under nitrogen flow at room temperature and then in a vacuum oven overnight. The lipid film was hydrated with 20 mM phosphate buffer containing 1mM EDTA (pH 7.4) followed by 5 min water bath sonication at room temperature and probe sonication (2 min × 50 w) to obtain clear DHE-sHDL. The final DHE concentration in peptide-DHE-sHDL was 0.5 mM. The LCAT assay was adapted from Homan *et al.* (212) and performed in 384-well black polystyrene plates in triplicate. Briefly, 8 μL of different concentrations (0, 5, 10, 20, 40, 60, and 100 μM) of DHE-sHDL (substrates) in assay buffer (PBS containing 1 mM EDTA, 5 mM β-mercaptoethanol, and 60 μM albumin, pH 7.4) preheated to 37°C were incubated with 8 μL of 5 μg/mL LCAT in dilution buffer (PBS with 1 mM EDTA and

60 µM albumin, pH 7.4) preheated to 37°C in triplicates. The plates were incubated at 37°C with gentle shaking (80 rpm/min) for different lengths of time (0, 10, and 20 min). Reactions were stopped by adding 4 µL of stop solution (3.75 U/mL cholesterol oxidase) in PBS containing 1mM EDTA and 7% Triton X-100. Then, the plates were incubated at 37°C with shaking (80 rpm/min) for another 1 h to quench the fluorescence of unesterified DHE. The fluorescence was measured at an excitation wavelength of 325 nm and an emission wavelength of 425 nm using the plate-reader (SynergyTM NEO HTS Multi-Mode Microplate Reader, Bio-Tek). A standard curve was made by plotting the fluorescence of serially diluted DHE-containing sHDL mixed with LCAT and using stop solution without COx versus the concentration (µM) of DHE. To calculate the concentration (µM) of DHE ester for each reaction, the background fluorescence (0 µM of DHE) was subtracted from all fluorescence measurements and then divided by the slope (fluorescence/µM) of the above standard curve. To calculate V_{max} and K_m, the concentrations (µM) of DHE ester at different time points were plotted against time (h), and the initial velocity (V_0, µM DHE-ester/h) was the slope of the linear range of DHE-ester concentration versus time. The V_{max} and K_m were obtained by plotting V_0 versus DHE concentration and then analyzed by GraphPad Prism 7 (nonlinear regression, Michaelis-Menten model).

3.3.7. *Plasma peptide stability*

The *in vitro* stability of 22A, 21A, and 22A-P peptides was assessed by the addition of 2.5 µL of 10 mg/mL of a peptide to 97.5 µL of fresh rat plasma (K2 EDTA, Innovative Research Inc). Immediately after the addition of peptide to plasma, 10 µL of serum was removed to serve as a baseline and stored at -20 °C. Samples were incubated at 37°C for 24 hours with shaking at 240 rpm. To determine peptide concentration at 0 and 24 h post plasma incubation, 10 µL of plasma

containing a peptide or working standard (0-100 µg/mL) was mixed with 2 µL of 2.4 mg/mL internal standard (5A peptide) and 38 µL of H$_2$O. Methanol (200 µL) was added to precipitate plasma proteins. The mixture was vortexed for 10 s, centrifuged at 12,000 rpm for 10 min and the supernatant was collected for LC-MS analysis. Samples were mixed (1:1 v/v) with LC-MS mobile phase (80:20 v/v H$_2$O:acetonitrile, 0.1% formic acid) and analyzed on Waters Acquity UPLC equipped with QDa System (Milford, MA) using Acquity UPLC BEH C18 1.7 µM column for separation. The mobile phase consisted of (A) water containing 0.1% v/v formic acid and (B) methanol containing 0.1% v/v formic acid. The mobile phase was delivered at 0.3 mL/min using a gradient elution of 20% to 80% B during 0-1.5 min, and 80% to 20% B during 1.5-3.5 min. Mass spectra were acquired in the positive ion mode with the mass range set at m/z 150-1250. Data analysis was performed on Waters Empower software. The concentration of 22A, 21A or 22A-P peptide in each sample was determined from the standard curve.

3.3.8. *Peptide pharmacokinetics, cholesterol mobilization, and esterification in vivo*

Healthy male Sprague-Dawley rats (8 weeks old) were purchased from Charles River Breeding Laboratories (Portage, MI) and were fed a standard rodent chow diet. To examine the impact of peptide composition on sHDL PK/PD properties, animals were randomly assigned to two groups (n = 4/group) for 22A-POPC/DPPC and 22A-P- POPC/DPPC administration. To examine the impact of lipid composition on sHDL PK/PD, animals were randomly assigned to four groups (n = 3/group) for 22A-POPC, 22A-DMPC, 22A-DPPC, and 22A-DSPC administration. All sHDL particle was prepared at 1:2 w/w peptide to phospholipid ratios, sterile filtered and characterized by DLS and gel permeation chromatography for size and purity prior to animal dosing. All animals were fasted overnight before sHDL dosing at 50 mg/kg (based on peptide

concentration) via tail vein injection. At each time point (pre-dose, 0.25, 0.5, 1, 2, 4, 8, and 24 h) blood samples (~0.3 mL) were collected from the jugular vein to heparinized BD tubes (Franklin Lakes, NJ) and centrifuged at 10,000 rpm for 10 min at 4°C. The obtained serum samples were stored at -20°C for further analysis.

The levels of plasma phospholipids (PL), total cholesterol (TC) and free cholesterol (FC) were determined enzymatically (Wako Chemicals, Richmond, VA) using a plate reader (SynergyTM NEO HTS Multi-Mode Microplate Reader, Bio-Tek). Esterified cholesterol levels (EC) were calculated as the difference between TC and FC levels at each time point. Briefly, serum samples were diluted with PBS for TC and FC detection, or with MilliQ water for PL detection. Defined amounts of standards or diluted samples were transferred to 96-well plates (50 µL, 60 µL and 20 µL for TC, FC and PL analyses, respectively), and assay reagents were added per manufacturer's instructions. The plates were gently shaken using an orbital shaker and incubated at 37˚C for 5 minutes. The UV absorbance at 600 nm was measured by a Molecular Devices SpectraMax M3 plate reader (Sunnyvale, CA). Pharmacokinetic parameters were also obtained by non-compartmental analysis. The pharmacodynamic effect in each rat was determined as the area under the total effect curve ($AUEC$) using trapezoidal rule. Secondary pharmacodynamic endpoints, maximal effect (E_{max}) and time to E_{max} ($T_{max,E}$) were also analyzed to compare pharmacodynamic effects.

Peptide (22A or 22A-P) concentration in serum was determined by LC-MS. The 10 µL serum aliquots were combined with 10 µL of 2.4 mg/mL of internal standard (5A peptide) and then mixed with 40 µL ddH$_2$O. Working standard solutions (0-100 µg/mL) of 22A and 22A-P were prepared as described above for plasma samples with the exception of using blank rat serum. Plasma proteins were precipitated by adding 180 µL of methanol. After 5 minutes, the mixture was

centrifuged (12000 rpm $\times$ 10 min, 4°C) and 100 µL of the supernatant was used for analysis. Each sample was analyzed by LC-MS as described above in the plasma peptide stability section. Pharmacokinetic parameters such as maximum serum concentration (C_{max}), the area under the serum concentration-time curve (AUC), elimination rate constant (K), elimination half-life ($T_{1/2}$), total clearance (CL), and volume of distribution (V_d) were obtained by non-compartmental analysis.

3.3.9. *Remodeling of sHDL particles in the plasma*

Remodeling of endogenous lipoproteins in human plasma was assessed by incubation with sHDL. Various sHDL (22A-POPC, 22A-DMPC, 22A-DPPC, 22A-DSPC, 21A-sHDL, 22A-sHDL, and 22A-P-sHDL) at 1 mg/mL concentration were incubated at 37°C for 1 h with shaking at 300 rpm. The sub-classes of HDL were separated by size and charge by one-dimensional native polyacrylamide gel electrophoresis (PAGE) and visualized by Western Blot using anti-ApoA-I antibody. Briefly, samples were subjected to electrophoresis using Tris-borate-EDTA (TBE) gradient (4 – 20%) acrylamide mini-gels. For each well, 10 µL of human plasma incubated with or without sHDL was mixed with 10 µL of 2X TBE sample buffer, and 6 µL of the resulting mixtures were loaded per well. Gels were run at 200V. Proteins were transferred to polyvinylidene difluoride membrane (PVDF) and incubated overnight with the anti-human ApoA-I-HRP conjugated antibody. Proteins were visualized with the enhanced chemiluminescent substrate on Protein Simple FluorChem M imaging system (San Jose, CA).

3.3.10. *Statistical analysis*

Significance of difference was determined by Student's *t*-test for comparing two groups or by one-way analysis of variance (ANOVA) with Dunnett's post-hoc test for comparing multiple
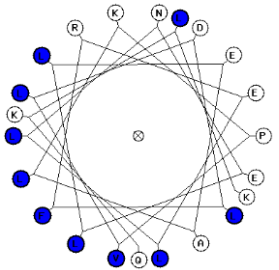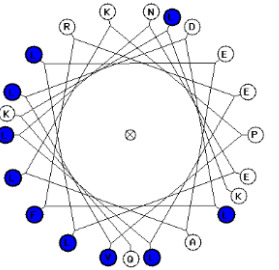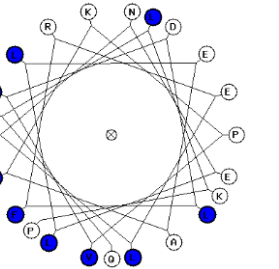
groups with 22A peptide or 22A-DMPC as the control. All samples were performed in triplicate and error bars were reported as a standard mean error (SEM) unless noted otherwise. P < 0.05 was considered statistically significant.

3.4.   Results

3.4.1. *Design of ApoA-I peptides with improved plasma stability*

Helical wheel plots for 22A, 22A-P, and 21A were generated to assess the amphipathic nature of each peptide. The hydrophobic amino acids clustered on one side of the helix suggested an amphipathic orientation of each peptide (**Table 3.1**). The 3D hydrophobic moment vector calculations were performed to predict and compare the interactions of each peptide with lipid membranes. It was determined that the hydrophobic moment vectors were almost identical with an average of 10.3 ± 0.7 A*kT/e. Additionally, we used an online server to determine the helix stability (ΔG_{hel}), transfer energy from water to membrane (ΔG_{trans}), and orientation of each peptide in the membrane (penetration depth, D). Again, we did not find large differences in any of the aforementioned parameters, suggesting that the absence of the terminal lysine in 21A or the addition of proline in 22A-P did not change the physical properties of these peptides compared to 22A. Next, we compared the plasma stability of 22A, 22A-P, and 21A as well as their abilities to bind lipid and form sHDL particles. We found that while 22A degrades in plasma with only 48% of intact peptide remaining after 24 h incubation at 37°C, both 22A-P and 21A are significantly more stable with 89 and 97% of intact peptide remaining, respectively. These results suggest that the plasma stability of 22A peptide can be greatly improved by the addition of a bulky proline, while computed lipid binding properties remained relatively unchanged.

Table 3.1. *Biophysical characterization of peptides.*

Peptide name	22A	21A	22A-P
Sequence	PVLDLFRELLNELLEALK QKLK	PVLDLFRELLNELLEAL KQKL	PVLDLFRELLNELLEAL KQKLKP
Helical wheel plot[a]			
Hydrophobic moment vector (A*kT/e)[b]	11.1	10.0	9.9
ΔG_{hel} **(kcal/mol)**[c]	-19.8	-19.4	-19.8
ΔG_{tran} **(kcal/mol)**[c]	-14.7	-13.4	-14.7
D (Å)[c]	11.8 ± 3.6	8.1 ± 4.6	11.8 ± 3.6
Helical content of lipid-free peptide (%)[d]	76.6	79.0	76.5
Helical content of lipid-bound peptide (%)[d]	93.9	90.9	81.6
Peptide plasma stability (%)[e]	48.4 ± 10.6	96.8 ± 5.4	89.3 ± 12.5

[a]*Helical wheel plots were generated using the online tool called Helixator where hydrophobic amino acids were highlighted in blue.* [b]*Hydrophobic moments were calculated by the 3D Hydrophobic Moment Vector Calculator.* [c]*Helix stability (ΔG_{hel}), transfer energy from water to membrane (ΔG_{tran}), and tilt angle in membranes were predicted by FMAP server for 22A, 21A, and 22A-P peptide sequences;* [d]*Helical content of lipid-free and lipid-bound peptides was determined by circular dichroism;* [e]*Peptide stability in rat plasma was determined by LC-MS shown as percent remaining peptide following 24 h incubation at 37°C (n=3, mean ± standard deviation).*

3.4.2. *Preparation and characterization of sHDL particles*

We next evaluated the ability of 21A, 22A, and 22A-P peptide to form homogeneous sHDL

particles. Synthetic HDL particles were prepared by combining 22A, 21A or 22A-P peptide with

DMPC at 1:2 w/w peptide:lipid ratio, which was previously used in ETC-642 formulation resulting in the formation of homogeneous sHDL particles with approximately 10 nm size (43,172). All three peptides formed homogeneous sHDL particles with average diameters of approximately 10 nm and a narrow polydispersity index of 0.17 ± 0.04 as determined by DLS (**Figure 3.1A**). Purity and homogeneity of sHDL size distribution were evaluated by gel permeation chromatography (**Figure 3.1B**). All three sHDL were over 98% pure, and negligible levels of the free peptide (<2%) were observed at the retention time of ~11 min (**Supplemental Table 1**). The binding of a peptide to phospholipid was also confirmed by increased helicity of 22A, 21A and 22A-P in sHDL particles (94, 91 and 82%) relative to the free peptide (77, 79 and 77%) as measured by CD.

We also altered the phospholipid composition of 22A sHDL to study its impact *in vitro* and *in vivo*. We chose four lipids with different physical properties such as transition temperature (T_m) and affinity for cholesterol (DSPC>DPPC>DMPC>POPC) (182,183,205). The sHDL complexes were formed by combining 22A peptide with individual lipids at 1:2 w/w ratio using the co-lyophilization method. All were highly homogeneous with an average hydrodynamic diameter ranging between 8.3 to 10.5 nm, low polydispersity index and gel permeation chromatography purity greater than 95% (**Figure 3.1C-D**). The purity, size, and polydispersity levels of sHDL are summarized in **Supplemental Table 1.** The DMPC, DPPC and DSPC-based sHDL had smaller hydrodynamic diameters, higher GPC purities, and sharper GPC peaks relative to 22A-POPC. The presence of free peptide (<1%, retention time ~11.3 min) and liposome impurities (<2%, retention time ~5.5 min) were observed for 22A-POPC, which also had the largest average particle size and broadest size distribution. Because POPC has the lowest T_m of -2 °C, it exists in a fluid gel state at room temperature, which likely impacts 22A-POPC stability.
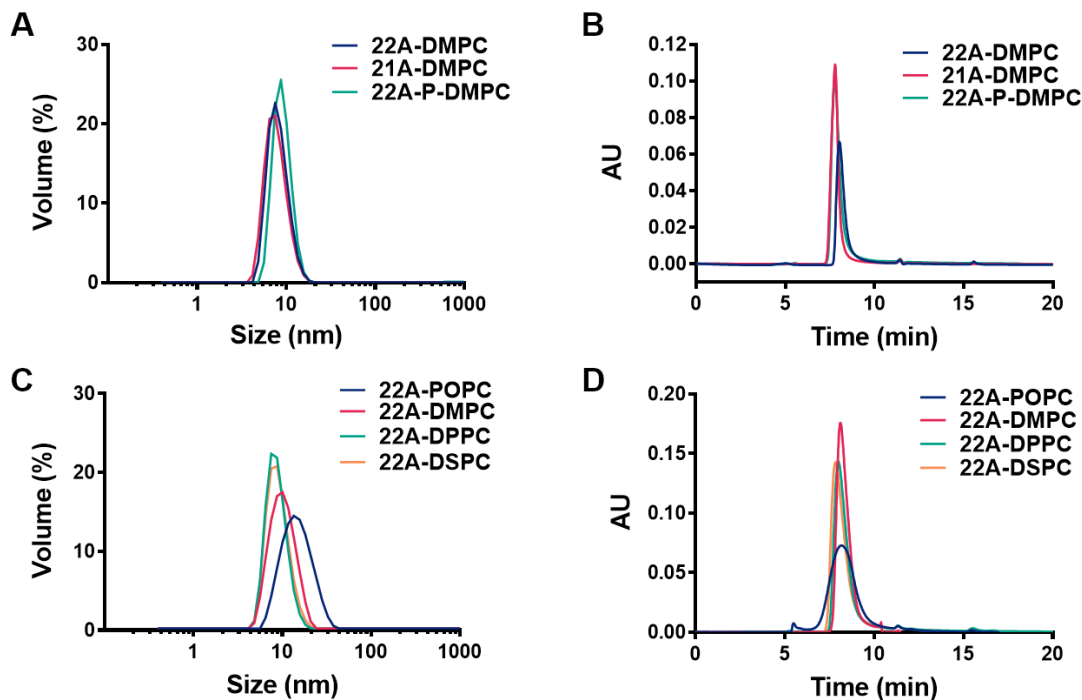
Figure 3.1. *Size distribution and purity of sHDL prepared with various peptide (A, B) and phospholipid (C, D) compositions. The size was determined by dynamic light scattering (DLS) (A, C) and purity was determined by gel permeation chromatography (GPC) (B, D).*

3.4.3. *Lipid composition of sHDL impacts macrophage cholesterol efflux*

We next examined how the C-terminal modifications in 22A-P and 21A impact cholesterol efflux abilities relative to 22A, either as free peptides or reconstituted into sHDL. Radioactive cholesterol was loaded into BHK cell line stably transfected with human ABCA1 transporter and peptides were incubated with the cells at 0, 0.01, 0.03, and 0.1 mg/mL. The same experiment was repeated using the control BHK-Mock cell line to assess cholesterol efflux by passive diffusion. Then, the non-specific cholesterol efflux values were subtracted from the data obtained for each peptide with ABCA1 transfected cells to reveal receptor-specific cholesterol efflux (**Figure 3.2A**). All three peptides exhibited concentration-depended cholesterol efflux with only minor differences

(< 5%) observed, indicating that modifications at the C terminal end of 22A did not affect lipid binding and ABCA1 transporter interaction. Then, the three peptide sequences were assembled into sHDL and their abilities to efflux cholesterol from macrophages were examined in RAW 264.7 cell line (**Figure 3.2B**). Similar to free peptide, we observed concentration-dependent cholesterol efflux with only minor differences (< 5%) at concentrations tested.

To explore the impact of the phospholipid component of sHDL on macrophage cholesterol efflux, 22A-POPC, 22A-DMPC, 22A-DPPC, and 22-DSPC were incubated with RAW 264.7 cells. Saturated long chain length phospholipids such as DPPC and DSPC have higher physical binding affinity to cholesterol relative to POPC and DMPC (182,183). However, the transition temperature of POPC and DMPC is below 37°C, thus the phospholipid bilayer is in liquid crystal state at physiological temperature facilitating cholesterol partitioning in these sHDL particles at the cell culture conditions (31). As expected, we observed greater cholesterol efflux to POPC and DMPC-based sHDL relative to DPPC and DSPC-based sHDL likely due to differences in lipid fluidity at 37°C (**Figure 3.2C**). Whereas 22A-DPPC and 22A-DSPC did not have any significant differences in cholesterol efflux as concentration increased, 22A-POPC and 22A-DMPC show sHDL concentration-dependent increase in cholesterol efflux. Interestingly, 22A-DMPC showed the most effective cholesterol efflux capability from as low as 36% at 0.01 mg/mL to as high as 61.8% at 0.1 mg/mL concentration. Membrane transporters such as ABCG1/G4 and SR-BI are known to play a major role in cholesterol efflux to HDL rather than lipid-free protein and may contribute to the differences seen between sHDL in our study (213,214). Taken together, the phospholipid composition of sHDL appears to play a significant role in cholesterol efflux from macrophages in cell culture.
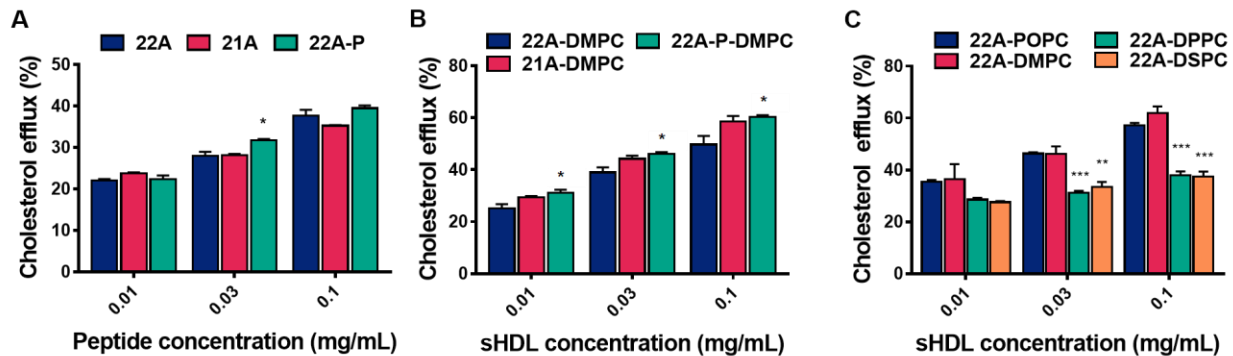
Figure 3.2. *Effect of peptides and sHDL on cholesterol efflux. Free peptides (22A , 21A, 22A-P) were used to efflux cholesterol from BHK cells stably transfected with ABCA1 transporter (A) and sHDL (22A-DMPC, 21A-DMPC, 22A-P-DMPC and 22A-POPC, 22A-DMPC, 22A-DPPC, 22A-DSPC) were utilized to efflux cholesterol from RAW 264.7 macrophage cells (B, C) at 0.01, 0.03, and 0.1 mg/mL for 18 hrs. The contribution of ABCA1 transporter was determined by subtracting efflux values of Mock-transfected cell line from ABCA1-transfected cell line (n=3, mean ± SEM). Statistical differences were compared to 22A peptide or 22A-DMPC with one-way ANOVA analysis with Dunnett's post-hoc test. $P < 0.05$ was considered statistically significant $^{*}P < 0.05$, $^{**}P < 0.01$, $^{***}P < 0.001$*

3.4.4. *Peptide and lipid composition both impact sHDL interaction with LCAT*

Following cholesterol efflux from macrophages, sHDL particles interact in plasma with LCAT (215). It is expected that both lipid and peptide composition of sHDL will have an effect on LCAT interaction. The fluidity of HDL lipid membrane determines the ease of LCAT binding to HDL particles (216). It has been shown that LCAT interaction with ApoA-I is critical for LCAT activation, especially for the facilitation of acyltransferase activity (217). Whereas some ApoA-I mimetic peptides have similar LCAT activation ability to full-length ApoA-I, others fail to facilitate EC formation (199,218,219). The presence of positively charged clusters on the C-terminus and presence of hydrophobic amino acids at positions 3, 6, 9 and 10, and net peptide charge of zero are believed to be critical to the high LCAT activation ability of 22A (199,220). To examine how modification of 22A and lipid composition of sHDL impact phospholipase A2

77

activity of LCAT, sHDL were co-incubated with enzyme and the kinetics of reduction of phospholipid concentration was monitored by LC-MS. We found that small changes in 22A sequence had only a limited impact on phospholipase A2 activity (lipolysis) activity (**Figure 3.3A**), indicating that LCAT activation by a C-terminal positive cluster on the peptide might not be critical for lipase activity. In contrast, the sHDL lipid composition had profound effect on LCAT-catalyzed phospholipid lipolysis with the rates of 0.08, 0.08, 0.01, and 0.0 h^{-1} for 22A-POPC, 22A-DMPC, 2A-DPPC and 22A-DSPC, respectively. DSPC and DPPC, phospholipids with T_m values above 37°C, had minimal lipolysis likely due to poor LCAT binding to sHDL and, thus, presumably difficulty in the accessibility of substrate for the enzymatic reaction.

Next, we assessed the impact of peptide and lipid composition of sHDL on LCAT acyltransferase activity by incorporating a fluorescent cholesterol analog called dehydroergosterol and measuring the rate of sterol esterification by LCAT. Changes in C-terminus of 22A peptide had a significant effect on the acyltransferase activity with a 2.6-fold decrease in k_{cat} upon the loss of lysine for 21A (**Figure 3.3C**). The rate was only decreased by 30% for 22A-P-HDL. When 22A-sHDL was complexed with different compositions of phospholipids, acyltransferase activity of LCAT was the highest for 22A-POPC sHDL (**Figure 3.3D**). Sterol esterification was only limited for 22A-DMPC sHDL, while no activity was detected for 22A-DPPC and 22A-DSPC. This trend was similar to the differences in phospholipase A2 activity observed for sHDL prepared with different lipids (POPC ≥ DMPC > DPPC > DSPC), following their general trends in T_m and membrane fluidity.
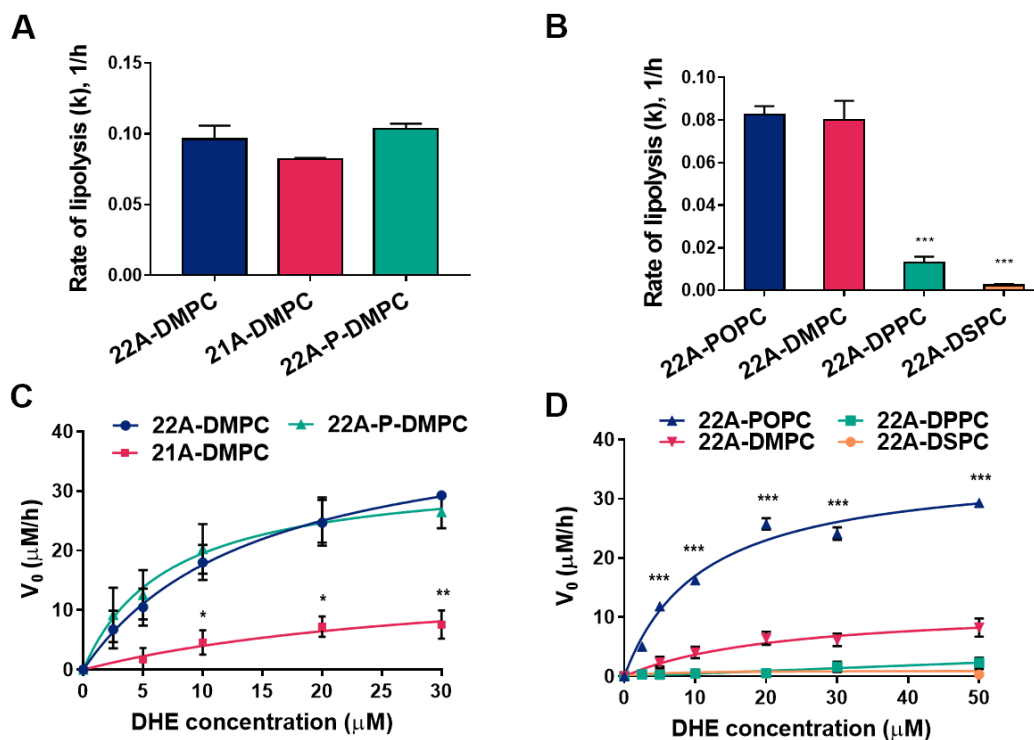
Figure 3.3. *Effect of peptide and phospholipid composition in sHDL on LCAT lipolysis and esterification rates. (A, B) The rate of sHDL lipolysis was determined by incubating sHDL (0.1 mg/mL) prepared with variable peptide composition (22A-DMPC, 21A-DMPC, 22A-P-DMPC) or variable phospholipid composition (22A-POPC, 22A-DMPC, 22A-DPPC, 22A-DSPC) with human rhLCAT (15 µg/mL) at 37 °C for 0, 5, 15, 30, 60, 90, and 120 min. The concentration of phospholipid at each time point was determined by LC-MS and the rate of lipolysis calculated from the slope of the concentration of the starting material versus time. LCAT esterification activity was measured for sHDL containing fluorescent cholesterol analog, dehydroergosterol (DHE) (C, D). The initial reaction rates (V_0) are plotted as a function of DHE concentration and the data were fitted into the Michaelis-Menten kinetic equation to calculate V_{max} and Km (n=3, mean ± SEM). Statistical differences were compared to 22A peptide or 22A-DMPC with the one-way ANOVA analysis with Dunnett's post-hoc test. $P < 0.05$ was considered statistically significant *$P < 0.05$, **$P < 0.01$, ***$P < 0.001$*

3.4.5. *Increase in peptide plasma half-life has no impact on cholesterol mobilization in vivo*

To evaluate whether *in vitro* peptide stability data correlates with *in vivo* peptide pharmacokinetics and cholesterol mobilization, we injected healthy Sprague Dawley rats with 22A-POPC-DPPC or 22A-P-POPC-DPPC sHDL at 50 mg/kg based on peptide concentration in

sHDL. Animal blood samples were collected before sHDL administration and at 0.25, 0.5, 1, 2, 4, 8, and 24 h post-dose. The peptide concentrations in rat serum were determined using LC-MS (**Figure 3.4A**). The noted stability of 22A-P when incubated with rat plasma translated well to *in vivo* settings with an increase in peptide circulation half-life and exposure ($T_{1/2}$ = 4.2 h and *AUC* = 17.2 mg*h/dL) compared to 22A ($T_{1/2}$ = 2.1 h and *AUC* = 5.5 mg*h/dL) (**Table 3.2**). We expected that these significant PK differences between two peptides would translate into increased cholesterol mobilization by sHDL *in vivo*. Additionally, we anticipated that levels of esterified cholesterol would be different between two formulations *in vivo* based on clear differences in LCAT-catalyzed esterification between 22A-sHDL and 22A-P-sHDL *in vitro*. However, we saw no differences in cholesterol mobilization and esterification profiles between 22A-sHDL and 22A-P-sHDL *in vivo* as quantified by enzymatic assay of rat serum samples (**Figure 3.4C-D, Table 3.2**). Finally, if the sHDL particle stayed intact upon *in vivo* administration, we would expect to see longer circulation half-life for total phospholipids with 22A-P-sHDL relative to 22A-sHDL. To test this hypothesis, we determined phospholipid concentrations in plasma pre- and post-sHDL administration by an enzymatic assay. We observed no differences in phospholipid PK parameters between 22A-sHDL and 22A-P-sHDL except for $T_{1/2}$ in which 22A-P-sHDL (1.3 h) showed significantly decreased $T_{1/2}$ compared to 22A-sHDL (1.8 h) (**Figure 3.4B, Table 3.2**). Altogether, these results suggest that the apparent differences in 22A-P and 22A stabilities in plasma and LCAT activation abilities had not resulted in measurable differences in cholesterol mobilization and esterification *in vivo*.
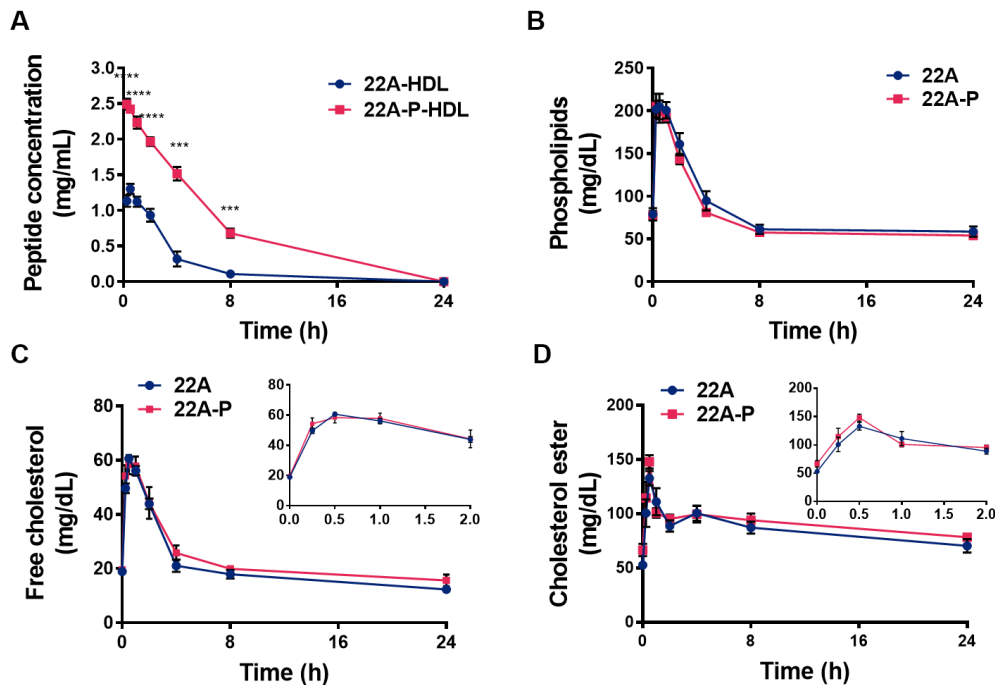
Figure 3.4. *Pharmacokinetic analysis of 22A and 22A-P peptides (A) or total phospholipids (B) in rat serum. Pharmacodynamic assessment of free cholesterol (C) and esterified cholesterol (D) mobilization in rat serum. Healthy male Sprague-Dawley rats were given a single tail vein injection of 50 mg/kg (based on peptide) of 22A-POPC-DPPC or 22A-P-POPC-DPPC and blood samples were collected at pre-dose and 0.25, 0.5, 1, 2, 4, 8, and 24 h after sHDL administration. Serum concentrations of peptides were determined by LC-MS while concentrations of phospholipids, free cholesterol, and esterified cholesterol were measured enzymatically (n=3). Statistical difference was compared with the two-tailed Student's t-test. P < 0.05 was considered statistically significant *P < 0.05, **P < 0.01, ***P < 0.001*

Table 3.2. Pharmacokinetic and pharmacodynamic parameters (%CV) of peptide, total phospholipids (PL), free cholesterol (FC), and esterified cholesterol (EC) after 50 mg/kg doses of 22A-sHDL and 22A-P-sHDL treatments.

	Parameters	Groups	
		22A-sHDL	22A-P-sHDL
Peptide	AUC (mg*h/dL)	5.5 (22.0)	17.2 (10.6)[***]
	K (h^{-1})	0.3 (25.8)	0.2 (12.0)
	T $_{1/2}$ (h)	2.1 (22.4)	4.2 (10.8)[**]
	CL (dL/h)	2.3 (21.8)	0.7 (10.9)[**]
	V$_d$ (dL)	6.9 (7.7)	4.4 (6.2)[**]
PL	AUC (mg*h/dL)	424.4 (15.7)	371.8 (23.5)
	K (h^{-1})	0.4 (23.8)	0.5 (16.0)
	T $_{1/2}$ (h)	1.8 (18.8)	1.3 (11.4)[*]
	CL (dL/h)	0.1 (7.7)	0.1 (7.0)
	V$_d$ (dL)	0.1 (21.4)	0.1 (2.1)
FC	T$_{max,E}$ (h)	0.5 (0.0)	0.8 (33.3)
	E$_{max}$ (mg/dL)	46.7 (5.8)	44.4 (13.0)
	AUEC (mg*h/dL)	158.0 (19.1)	175.3 (28.5)
EC	T$_{max,E}$ (h)	0.42 (24.5)	0.4 (33.3)
	E$_{max}$ (mg/dL)	51.3 (31.8)	42.2 (37.3)
	AUEC (mg*h/dL)	166.8 (12.8)	164.4 (31.8)

*Data were shown as mean with CV%. *P<0.05, **P < 0.01, ***P < 0.001. AUC: the area under the curve. K: elimination rate constant. T1/2: the half-life of elimination. CL: total clearance. Vd: volume of distribution. Tmax,E: time at which the Emax is observed. Emax: the maximum plasma concentration of different cholesterol species. AUEC: the area under the effect curve.*

3.4.6. Lipid composition of sHDL impacts cholesterol mobilization in vivo

To investigate the contribution of phospholipid composition of sHDL on cholesterol mobilization and esterification profiles *in vivo*, we administered 22A-POPC, 22A-DMPC, 22A-DPPC, and 22A-DSPC sHDL to healthy Sprague Dawley rats. Based on cholesterol efflux from RAW 264.7 cells and LCAT-catalyzed esterification results *in vitro* we were expecting to see higher cholesterol mobilization and esterification for POPC and DMPC-based sHDL *in vivo*.

However, the results of *in vivo* administration of 50 mg/kg of sHDL were reversed with 22A-DSPC showed significantly higher free cholesterol mobilization to the plasma compartment represented by the area under the effect curve (*AUEC*) $AUEC_{22A\text{-}DSPC}$ = 540 mg*h/dL compared to three other sHDL formulations with lower $AUEC_{22A\text{-}POPC}$ = 80 mg*h/dL, $AUEC_{22A\text{-}DMPC}$ = 130 mg*h/dL, and $AUEC_{22A\text{-}DPPC}$ = 220 mg*h/dL (**Figure 3.5, Table 3.3**). Although the C_{max} of plasma EC was higher for DMPC-based sHDL, DSPC-based sHDL administration resulted in higher EC concentration at later time points and 3.5-fold greater *AUEC* values relative to DMPC-based sHDL (**Figure 3.5D, Table 3.3**). The differences between *in vitro* and *in vivo* results could be attributed to differences in lipid T_m affecting the *in vivo* circulation time. Our *in vivo* data supports this hypothesis where phospholipids with higher transition temperatures such as DSPC (T_m = 55°C) showed greater half-life and slower clearance than other phospholipids (**Figure 3.5B**). Interestingly, the 22A peptide kinetics such as plasma half-life after administration of sHDL in rats did not follow phospholipid kinetics similar to the differences in PK parameters between lipid and peptide obtained with 22A- and 22A-P-sHDL. The half-life of 22A after the 22A-DSPC infusion was nearly identical to 22A-DMPC, 22A-POPC, and 22A-DPPC formulations (3.3 h, 3.0 h, 3.3 h, and 3.3 h, respectively) (**Table 3.3**). Taken together, these results suggest that the ability of sHDL to mobilize cholesterol is strongly dependent on phospholipid composition and pharmacokinetics.
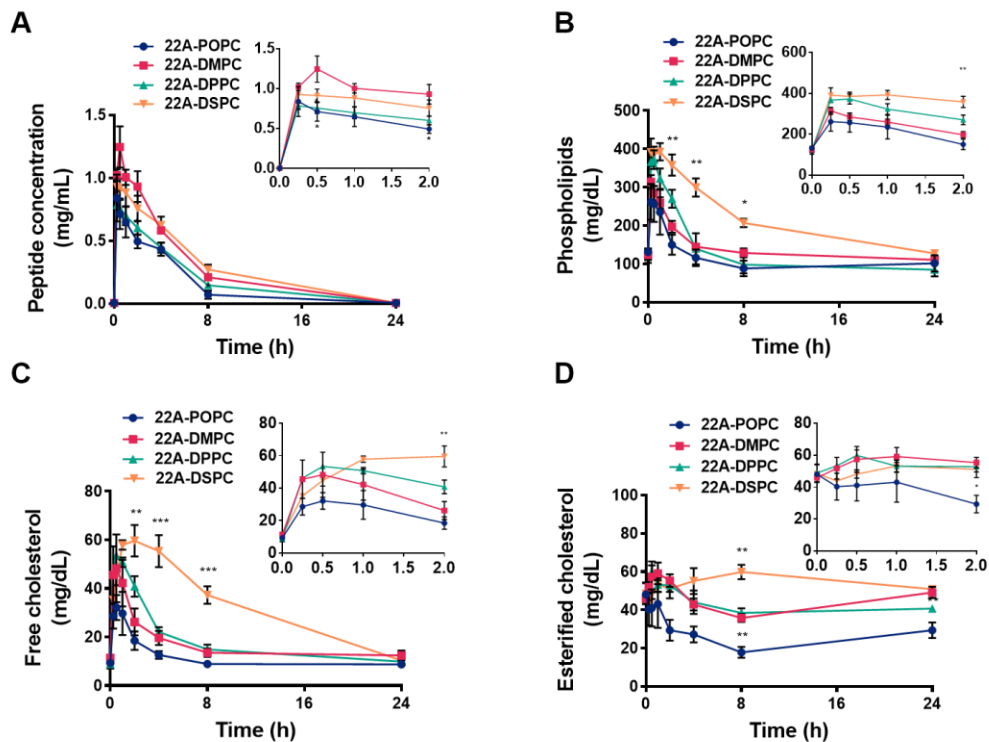
Figure 3.5. *Pharmacokinetic analysis of 22A (A) and total phospholipids (B) in rat serum. Pharmacodynamic assessment of free cholesterol (C) and esterified cholesterol (D) mobilization in rat serum. Healthy male Sprague-Dawley rats were given a single tail vein injection of 50 mg/kg (based on peptide) of 22A-POPC, 22A-DMPC, 22A-DPPC, or 22A-DSPC and blood samples were collected at pre-dose and 0.25, 0.5, 1, 2, 4, 8, and 24 h after sHDL administration. Serum concentrations of peptides were determined by LC-MS while concentrations of phospholipids, free cholesterol, and esterified cholesterol were measured enzymatically (n=3). Statistical differences for 22A-phospholipid were compared to 22A-DMPC with one-way ANOVA analysis with Dunnett's post-hoc test. P < 0.05 was considered statistically significant. P < 0.05, **P < 0.01, ***P < 0.001*

Table 3.3. Pharmacokinetic and pharmacodynamic parameters (%CV) of 22A peptide, total phospholipids (PL), free cholesterol (FC), and esterified cholesterol (EC) after 50 mg/kg doses of 22A-POPC, 22A-DMPC, 22A-DPPC, and 22A-DSPC sHDL treatments.

	Parameters	Groups			
		22A-POPC	22A-DMPC	22A-DPPC	22A-DSPC
Peptide	AUC (mg*h/dL)	3.6 (8.6)**	6.6 (10.0)	4.6 (15.2)*	6.9 (17.7)
	K (h^{-1})	0.2 (6.0)	0.2 (1.7)	0.2 (2.4)	0.2 (4.0)
	$T_{1/2}$ (h)	3.3 (6.2)	3.0 (1.8)	3.3 (2.4)	3.3 (4.2)
	CL (dL/h)	5.6 (11.8)**	3.2 (13.9)	4.6 (17.4)	2.9 (25.2)
	V_d (dL)	27.1 (16.7)**	14.0 (15.5)	21.9 (19.0)	13.7 (29.1)
PL	AUC (mg*h/dL)	371.6 (29.0)	703.2 (23.2)	934.9 (22.8)	2396 (21.1)***
	K (h^{-1})	0.7 (10.6)***	0.2 (4.4)	0.3 (16.8)	0.0 (12.6)**
	$T_{1/2}$ (h)	1.0 (9.8)***	3.3 (4.4)	2.2 (18.6)*	6.0 (12.4)***
	CL (dL/h)	0.1 (22.2)	0.1 (23.3)	0.0 (27.7)***	0.0 (27.3)***
	V_d (dL)	0.2 (29.8)	0.3 (23.3)	0.2 (45.9)	0.1 (16.0)*
FC	$T_{max,E}$ (h)	0.7 (35.4)	0.4 (28.3)	0.7 (35.4)	1.3 (35.4)*
	E_{max} (mg/dL)	25.8 (36.8)	37.6 (19.8)	44.8 (5.1)	51.5 (15.3)
	$AUEC$ (mg*h/dL)	79.4 (33.9)	126.5 (10.0)	215.0 (20.9)	536.4 (19.1)***
EC	$T_{max,E}$ (h)	0.5 (70.7)	0.8 (28.3)	0.9 (84.3)	6.7 (28.3)**
	E_{max} (mg/dL)	7.7 (65.2)	28.2 (30.3)	24.9 (13.7)	20.6 (24.7)
	$AUEC$ (mg*h/dL)	84.8 (65.3)	93.3 (41.9)	98.9 (31.6)	334.7 (18.0)**

*Data were shown as mean with CV%. *P<0.05, **P < 0.01, ***P < 0.001. AUC: the area under the curve. K: elimination rate constant. T1/2: the half-life of elimination. CL: total clearance. Vd: volume of distribution. Tmax,E: time at which the Emax is observed. Emax: the maximum plasma concentration of different cholesterol species. AUEC: the area under the effect curve.*

3.4.7. Remodeling of endogenous HDL in human plasma

To assess how different compositions of sHDL facilitate the remodeling of endogenous lipoproteins, all sHDL particles were incubated with human plasma for 1 hour at 1 mg/mL peptide concentration. The HDL sub-fractions were separated by size using 1D native PAGE electrophoresis and visualized by Western Blot using anti-ApoA-I antibodies (**Figure 3.6**). Compared to human plasma control incubated with PBS, incubation of plasma with 22A-sHDL,

21A-sHDL, and 22A-P-sHDL resulted in the remodeling of endogenous HDL indicated by a diminished signal for the large α-HDL and increased levels of lipid-poor ApoA-I. The effect of the phospholipid composition of sHDL on endogenous HDL remodeling was more prominent. Incubation of plasma with 22A-POPC resulted in a shift of HDL size from large α-HDL to smaller pre-β HDL. Incubation with 22A-DMPC showed the formation of even smaller pre-β HDL particles with a band of lipid-free ApoA-I. In contrast, plasma incubation with 22A-DSPC displayed very limited HDL remodeling, likely due to the rigidity of the DSPC lipid membrane and thus reduced the insertion of endogenous ApoA-I. The 22A-DPPC incubation with plasma resulted in some reduction of α-HDL levels and formation of a predominant band of lipid-free ApoA-I. Overall, the extent of HDL remodeling was significantly affected by the phospholipid composition of sHDL. The sHDL prepared with high T_m phospholipids (22A-DPPC and 22A-DSPC) exhibited higher plasma stability and less remodeling.
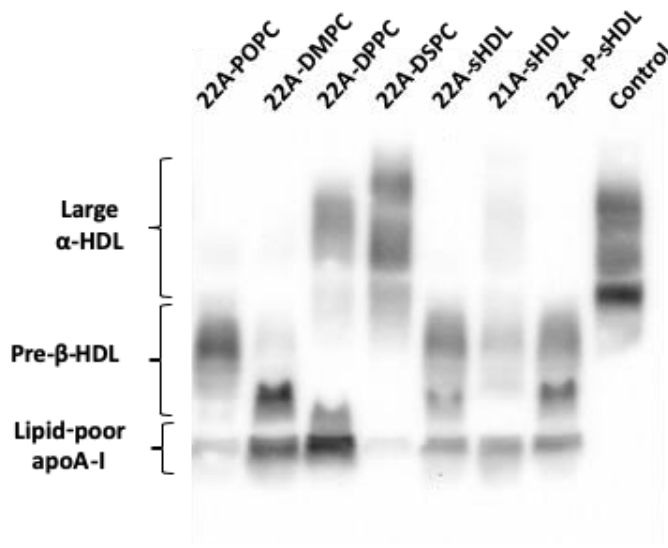
Figure 3.6. *Effect of sHDL incubation with human plasma on endogenous HDL remodeling. Various compositions of sHDL were incubated in human plasma at 1 mg/mL for 1 h at 37°C. Lipoproteins were separated by 1-D native page electrophoresis and visualized by western blot using anti-apoA-I antibody.*

86

3.5. Discussion

Our previous studies have shown that upon intravenous administration of sHDL, 22A peptide becomes rapidly hydrolyzed into 21A due to the loss of terminal lysine (172). The addition of the C-terminal proline after the labile lysine in 22A afforded a resistant to proteolysis peptide as shown by incubation of 22A-P with rat plasma. The new peptide was successfully formulated into sHDL and dosed into rats. We expected to see longer circulation time and corresponding greater *in vivo* cholesterol mobilization for 22A-P-sHDL. As predicted *in vitro*, the half-life of 22A-P in animals was extended from 2.1 to 4.2 hours and AUC for 22A-P is nearly 3-fold higher. However, the longer circulation time of 22A-P *in vivo* did not translate into a higher cholesterol mobilization profile by 22A-P-sHDL compared to 22A-sHDL. Furthermore, the AUC of the phospholipid component of 22A-P-sHDL and 22A-sHDL were also not affected by the extension of the peptide half-life. When sHDL particles prepared with the same peptide 22A and different phospholipids (POPC, DMPC, DPPC, or DSPC) were administered to rats the peptide half-life was similar for all four formulations (3.2 ± 0.1 h). However, the phospholipid half-life varied dramatically with DSPC circulating for 6.0 h compared to 1.0 - 3.3 h for other lipids. The trend of phospholipid circulation time for each sHDL formulation in animal serum was similar to that of cholesterol mobilization (22A-DSPC> 22A-DPPC, 22A-DMPC> 22A-POPC). Moreover, these findings are further supported by our HDL remodeling results, showing only limited interaction of 22A-DSPC with endogenous HDL, which could extend circulation half-life. The limited remodeling by endogenous lipoproteins is likely due to the difficulty of protein insertion in the gel membrane of DSPC (T_m of 55 °C, above physiological temperature) as was observed *in vitro* for 22A-DSPC interaction with LCAT. Altogether, the data suggest that the pharmacokinetics of peptide and lipid components in sHDL are not interdependent and original infused sHDL particles

may dissociate or become remodeled upon administration *in vivo*. In addition, the phospholipid rather than peptide component in sHDL has a major impact on the ability to mobilize cholesterol *in vivo*. However, it is important to note that the peptide sequence modifications performed by us were rather minor. It has been shown that different sequences of ApoA-I mimetic peptides have measurable differences in cholesterol efflux *in vitro* and variable *in vivo* performance (130,131,139,140).

Several other groups reported on the discordance between the PK of protein and phospholipid components of HDL *in vivo*. Xu *et al.* investigated the fate of ApoA-I protein and phospholipid after *in vivo* administration of HDL in an attempt to interrogate the validity of the reverse cholesterol transport pathway (221). The investigators used ABCA1-derived ApoA-I-HDL with radiolabeled components and reported that phospholipids and ApoA-I enter different pathways for clearance in mice. The authors suggested that after the administration of radiolabeled ApoA-I-HDL, phospholipids were rapidly cleared by the liver and also transferred to LDL while ApoA-I fused with endogenous HDL and circulated longer. CSL-112, the ApoA-I-soybean phosphatidylcholine sHDL product undergoing phase III clinical trial, is believed to undergo remodeling in human plasma with the generation of lipid-poor ApoA-I that is important for cholesterol efflux (222). Another sHDL product in clinical development, CER-001, composed from ApoA-I and primarily sphingomyelin, have shown differences, specifically longer half-life for phospholipid (~46 h) relatively to ApoA-I (~10 h) (223,224). We also found that incorporation of polyethylene glycol-modified lipids in ApoA-I peptide-based sHDL extended circulation time for lipids and prolonged the duration of mobilized cholesterol circulation but had not altered ApoA-I peptide PK (173). Therefore, peptide and lipid components of sHDL may both contribute

to cholesterol mobilization, however not as intact nanoparticles, but rather as separate entities via different mechanisms.

The phospholipid composition also impacted the ease of sHDL preparation, purity, and size of the resulting nanoparticles and their stability *in vitro* and *in vivo*. The sHDL prepared with DSPC, DPPC, and DMPC showed relatively similar narrow size distributions and high purities while sHDL prepared with POPC appeared to be more heterogeneous with larger average particle sizes and a presence of liposomal impurities. This relative difficulty of forming pure POPC-based sHDL particles has been reported previously and was attributed to the fluidity and instability of the POPC membrane at room temperature, which was well above the phospholipids T_m (179). The sHDL prepared with saturated lipids appeared to be more homogeneous and pure but required heating particles above lipid T_m during preparation to facilitate ApoA-I peptide-lipid binding. In addition, the presence of unsaturated double bonds in lipids such as POPC could result in phospholipid oxidation, although this phenomenon was not investigated in this study.

Interestingly, we also observed a discordance between *in vitro* and *in vivo* results for sHDL prepared with different phospholipids and peptides. The *in vitro* trends for higher cholesterol efflux and superior ability to activate LCAT for 22A-POPC and 22A-DMPC did not translate into higher cholesterol mobilization and esterification *in vivo*. The free cholesterol mobilization and circulation time appear to be closely following the circulation time of phospholipids, with the longer circulating saturated DSPC exhibiting higher C_{max} for FC mobilization and *AUEC*. Thus, the ease of cholesterol incorporation in unsaturated 22A-POPC becomes of limited significance *in vivo* due to the rapid elimination of POPC. The esterification seems to follow the same trend, as faster LCAT-catalyzed lipolysis and sterol esterification did not translate to greater C_{max} and *AUEC* for EC *in vivo*. However, it is important to point out that the actual rate of EC formation and LCAT

activation *in vivo* was not directly measured in this study and will require additional experiments as described by Turner *et al*. (225). The stability of 22A-P is greatly improved *in vivo* relative to 22A, however phospholipid PK appeared to be unchanged and cholesterol mobilization follows phospholipid PK. One of the explanations for this may be that both 22A and 22A-P are capable of forming sHDL *in vitro* and maintaining sHDL stability *in vivo*, as the structures of all three peptides used by us are very similar. It is also important to point out that other groups had seen discordance between showing some structure-activity relationship for ApoA-I peptides *in vitro* and seeing no statistical differences in their pharmacological effects *in vivo* (226).

Our data support the complexity of RCT and highlights that both ApoA-I protein/peptide and lipid components of sHDL contribute to the RCT pathway. The study also highlights that the phospholipid composition of sHDL is the driving force for cholesterol mobilization *in vivo* and we plan to further examine if higher cholesterol mobilization for sHDL composed of saturated lipids will lead to greater anti-atherosclerosis effect in a murine model of the disease.

3.6.   Supplemental Information

Table 3.4. Characterization of sHDL particles prepared with different peptides and phospholipids.

Name	Particle Size (nm)[a]	Retention Time (min)[b]	Purity (%)[c]	Impurity (%)[c]	
				Free Peptide	Liposome
22A-DMPC	10.1 ± 3.3	8.0	98.5	1.1	0.4
21A-DMPC	9.9 ± 3.4	7.8	99.4	0.6	0.0
22A-P-DMPC	10.5 ± 3.6	7.6	98.2	1.8	0.0
22A-POPC	10.4 ± 3.9	8.2	98.0	0.9	1.1
22A-DMPC	8.3 ± 1.9	8.1	99.1	0.9	0.0
22A-DPPC	9.2 ± 2.3	8.0	98.8	0.9	0.3
22A-DSPC	9.9 ± 2.5	7.8	99.2	0.8	0.0

[a]*Particle size of sHDL measured by DLS;* [b]*Retention time of sHDL particle measured by GPC;* [c]*Purity and impurity of sHDL determined by the area under the curve from GPC.*

Chapter 4

MiNano Mimicking High-Density Lipoproteins Reverses Atherosclerosis and Prevents Inflammatory Response in Animals

4.1.   Abstract

Over decades, reconstituted high-density lipoprotein (rHDL or sHDL) therapy has shown promising results of atheroma volume reduction in patients with cardiovascular diseases (CDV). We speculate, in the near future, that an exponential amount of human plasma purified apolipoprotein A-I (apoA-I) or recombinant apoA-I will be required for commercialization of rHDL or sHDL therapy due to the high prevalence of CVD. Nevertheless, purification of such apoA-I is highly difficult and costs a great amount of money. Here, we formulated a nano-micelle called MiNano that is a structural nano-mimetic of sHDL with a small particle size (12-14 nm) and a hydrophobic core and hydrophilic exterior. It showed similar biological functionality to sHDL including cholesterol efflux capability from macrophages and cholesterol elimination to hepatocytes. Interestingly, MiNano inhibited inflammatory cytokines, as much as 14-fold greater, compared to sHDL. In addition, MiNano exhibited a 2-fold increased cholesterol mobilization compared to sHDL. Moreover, MiNano showed successful inflammatory cytokine inhibition in a lipopolysaccharide-induced endotoxin mice model. MiNano also led to an atheroma reduction of up to 40% in an atherosclerosis mice model. In summary, a novel nano-micelle, MiNano, resulted in a structural and functional mimetic of sHDL and had a successful effect against various diseased mice models. Because of its composition and preparation simplicity, we propose MiNano could

be a promising sHDL alternative in treatment against atherosclerosis and other inflammatory-related diseases.

4.2. Introduction

Cardiovascular disease (CVD) is the leading cause of death in the United States (227). Imbalance of metabolism and vascular inflammation induces accumulation of cholesterol loaded macrophages in the sub-intimal space and further forms lipid-rich vulnerable plaques in the arteries that could be ruptured and lead to cardiovascular infarct and death (228–230). The majority of therapeutics against CVD target the suppression of cholesterol synthesis and absorption to prevent new plaque. However, there are no therapeutics yet to reduce the existing atheroma burden (231,232).

High-density lipoprotein (HDL) is the smallest and densest of the plasma lipoproteins consisting of apolipoprotein A-I (apoA-I) and phospholipids. HDL has an average diameter of 8 – 12 nm with a hydrophilic exterior to promote plasma circulation and a hydrophobic interior to facilitate cholesterol sequestration (233). HDL exerts a number of physiological functions, such as reverse cholesterol transport in which excess cholesterol is effluxed from lipid-laden macrophages, mobilization of effluxed cholesterol into blood circulation, and trafficking of cholesterol to the liver for elimination via the mechanism known as the reverse cholesterol transport (RCT) (234).

Its small particle size allows HDL to translocate at the endothelial layer into the core of the atheroma to interact with macrophages to efflux cholesterol (235). However, the number of functional HDL particles in individuals with CVD is observed in low levels and the capability to efflux cholesterol is reduced (236). Therefore, reconstituted or synthetic HDL (rHDL or sHDL) products have been developed and clinically tested for their abilities to reduce atheroma burden.

sHDL is generally complexed by using purified human apoA-I or recombinant apoA-I with commercially available phospholipids.

In general, patients with CVD who are on rHDL/sHDL therapy require 5 to 6 weekly dosages to reduce plaques (237,238). CSL-112, for example, showed a significant decrease in mortality, myocardial infarction, and stroke, which led to a phase III clinical trial with 17,400 patients (239). CSL-112 requires a 40 mg/kg dose to achieve clinical efficacy, which is calculated as approximately 20 g of human plasma purified apoA-I per therapy. Based on the conservative estimates of patients needing annual treatment, at least 20 tons of apoA-I protein is required. In addition, such recombinant manufacturing processes for apoA-I is very costly due to several factors; hydrophobic nature of this protein, relatively low expression levels of apoA-I, and multiple purification steps for removal of protein-bound hydrophobic impurities. Therefore, there is a speculation in which a plasma purified version of apoA-I will likely result in a shortage of plasma supply due to high market needs in the future.

Nanomaterials have been shown to mimic the structures and functions of human proteins (240). Nanoparticles are similar to globular proteins in terms of their size, charge, and shape. Nanoparticles can be also coated with organic functional groups to function as protein mimetics. For these reasons, several groups proposed nanotechnology-based functional mimetics of sHDL (241–244). For example, one group developed the HDL biomimetic on a gold nanoparticle core with a functionalized surface via attachment of phospholipids and apoA-I proteins (241,245). Another group developed a poly(lactic-co-glycolic) acid (PLGA) core functionalized with lipids and apoA-I mimetic peptides (243,246). Such HDL nano-mimetics can accumulate in atherosclerosis plaques and achieve a similar cholesterol efflux capacity as HDL (247).

In this study, we aimed to create a synthetic nanoparticle that mimics the structural and functional properties of sHDL intending to meet two main requirements; 1) display an endogenous HDL particle size of 10 – 12 nm in diameter to allow endothelial layer penetration and cholesterol efflux from macrophage and 2) exhibit amphipathic nature of HDL with a hydrophilic exterior for long circulation time and a hydrophobic core with the ability to expand in size to allow for cholesterol sequestration in the nanoparticle core. To achieve these requirements, we have formulated phosphatidylcholine (PC) with polyethylene-glycol modified PC (PEG-PC) to complex nanoparticles with fatty acids tails in the hydrophobic interior, and hydrophilic phosphate head groups and PEG on the exterior at the target particle size of 10 to 15 nm. We further narrowed down our formulations to two HDL biomimetics with different sizes (MiNano-12 and MiNano-14) to compare with sHDL complexed with PC and apoA-I mimetic peptides. This particular sHDL was previously investigated in single and multiple-dose clinical studies known as ETC-642 which has been well established for its safety and efficacy (127,166). We found that a novel HDL biomimetic nano-micelle (MiNano) showed a 14-fold improved inhibition against LPS-induced pro-inflammatory mediators, a 2-fold higher cholesterol mobilization capacity *in vivo*, and a 2-fold superior anti-atherogenic effect in an ApoE-/- murine model of the disease.

4.3. Materials and Methods

4.3.1. Materials

ApoA-I mimetic peptides 22A (PVLDLFRELLNELLEALKQKLK) were synthesized by Genscript (Piscataway, NJ). The peptide purities were determined to be over 95% by reverse phase HPLC. 1,2-dipalmitoyl-sn-glycero-3-phosphocholine (DPPC) and N-(Carbonyl-methoxypolyethyleneglycol 2000)-1,2-distearoyl-sn-glycero-3-phosphoethanolamine (DSPE-PEG2k) were purchased from NOF Corporation (White Plains, NY). Bodipy-labeled cholesterol

94

was purchased from Avanti Polar Lipids, Inc. (Alabaster, AL). Lipopolysaccharide (LPS) (E. coli O111:B4) was purchased from Sigma Aldrich (St. Louis, MO). All other materials were obtained from commercial sources.

4.3.2. Preparation of sHDL and MiNano

All investigated particles were prepared using a co-lyophilization method. Briefly, to prepare sHDL, 22A peptide and DPPC were dissolved in glacial acetic acid at a molar ratio of 0.14:1. Micellar nanoparticles (MiNanos) were prepared by dissolving DPPC and DSPE-PEG2000 in glacial acetic acid at the molar ratios of 1:0.065, 1:0.131, 1:0.262, 1:0.523, 1:1.05 and 1:2.09. After freeze-drying for over 24 hours, PBS (pH = 7.4) was added to hydrate the powders to a final lipid concentration of 27.24 mM. The mixture was vortexed briefly, heated to 50°C for 10 min. and cooled to 25°C for 10 min. This cycle was repeated three times. sHDL particle and MiNano concentrations are expressed in terms of total lipid concentration throughout this work.

sHDL and MiNano particles loaded with DiR fluorescent dye or bodipy-labeled cholesterol were prepared by a freeze-drying method and by dissolving DiR or labeled cholesterol in glacial acidic acid together with all other components. The final concentration of bodipy-cholesterol after hydration of the lyophilized powder was 30 μg/mL.

4.3.3. Characterization of sHDL and MiNano

The particle size distribution of sHDL and MiNano was determined by dynamic light scattering (DLS) using a Zetasizer Nano ZSP, Malvern Instruments (Westborough, MA) at a concentration of 2.7 μM. The average size and polydispersity index with standard deviation were reported. The particle morphology was assessed by transmission electron microscopy (TEM). The

diluted sample solution was deposited on a carbon film-coated 400 mesh copper grid and dried for 1 minute. Samples were then negatively stained with 1% (w/v) uranyl formate, and the grid was dried before TEM observation. All specimens were imaged on a 100kV Morgagni TEM equipped with a Gatan Orius CCD.

4.3.4. *Cholesterol efflux evaluation*

RAW 264.7 cells were grown in DMEM medium supplemented with 10% FBS, penicillin (100 units/ml) and streptomycin sulfate (100 mg/ml) in a humidified 5% CO2 atmosphere. 1×10^5 cells were then seeded into 24-well plates and grown for 24 h. Cells were washed with PBS (pH 7.4) once at room temperature and labeled with cholesterol for 24 h in DMEM/BSA/antibiotic media (0.5 mL) containing 1 μCi of [^{3}H] cholesterol/mL of media. Subsequently, labeled cells were washed twice with PBS (pH 7.4) to remove [^{3}H] cholesterol that was not taken up by the cells. Tritium-labeled cholesterol was effluxed from cells for 18 h, using various lipid complexes at different concentrations in duplicate. Finally, all cell media (0.5 mL) was removed into separate Eppendorf tubes and centrifuged at 10,000 rpm for 5 min. The remained cells were lysed with a 0.1% SDS / 0.1M NaOH solution for 2 h. Radioactive counts of media and cell fractions were measured separately using a Perkin Elmer liquid scintillation counter. Percent cholesterol effluxed from cells was calculated by dividing media counts by the total sum of media and cell counts and then multiplying this number by 100%.

4.3.5. *Liver cell uptake of cholesterol form sHDL and MiNano*

The uptake of bodipy-labeled cholesterol loaded in either sHDL or MiNano by HepG2 cells was visualized by confocal laser scanning microscopy and quantified by flow cytometry. Briefly, liver hepatocellular carcinoma (HepG2) cells were cultured in Dulbecco's Modified Eagle

Medium with 10% FBS and 1% Pen Strep Glutamine and maintained in an incubator at 37°C and 5% CO2. On day 0, 1 x 10^4 to 1 x 10^5 cells were seeded in a MatTek 35 mm petri dish in DMEM. The next day, the media was aspirated and cells were washed with PBS (pH 7.4). Fresh media containing sHDL or MiNano loaded with bodipy-labeled cholesterol was added at a final lipid concentration of 272.4 μM. After incubation at 37 °C for 2 h, cells were washed twice with PBS (pH 7.4) followed by fixation with 4% paraformaldehyde in PBS for 15 min at room temperature. 1% Triton-X solution was then added to the dish for 15 min and washed twice with PBS (pH 7.4).

Finally, the cell nuclei were stained with DAPI. The nuclei and bodipy fluorescence images were acquired on a Nikon A-1 Spectral Confocal microscope system (Nikon Corporation, Tokyo), with an excitation wavelength of 495 nm for bodipy. Quantification of the cellular fluorescent signal was performed using a cell sorter (Beckman Coulter FC500 5-colour analyzer) at an excitation wavelength of 495 nm.

4.3.6. *Anti-inflammation effect of sHDL and MiNano in vitro*

To evaluate the anti-inflammatory effect of sHDL and MiNano, RAW 264.7 macrophage cells were seeded in a 96-well plate on the first day. After a 24 h incubation, cytokine release from macrophage cells was stimulated by the addition of 2 ng/mL lipopolysaccharides (LPS). Subsequently, nanoparticles were added to the media immediately after the LPS at a 27.2 uM lipid concentration and incubated for 16 h. The level of pro-inflammatory cytokines, TNF-α and IL-6, in the media were measured with an ELISA kit (Thermo Fisher Scientific, Waltham, MA). HEK-Blue cells purchased from InvivoGen (San Diego, CA) were cultured in DMEM containing 10% low endotoxin FBS and selective antibiotics according to the manufacturer's instructions. The growth medium was discarded, and cells were resuspended in HEK-Blue Detection medium. Cells

were seeded at 25,000 cells per well. The cells were treated with sHDL or MiNano at 0.082 mM in the presence or absence of 2 ng/ml of LPS and incubated for 18 hours. LPS binding to TLR4 results in the activation of NF-κB reporter gene expression, causing the HEK-Blue detection medium to turn blue. The blue color was quantified by measuring absorption at 650 nm using a SpectraMax M3 plate reader from Molecular Devices (San Jose, CA).

4.3.7. *Pharmacokinetics and pharmacodynamics evaluation in rats*

The sHDL and MiNano were prepared at a final lipid concentration of 54.48 μM in PBS (pH 7.4). Eight male Sprague-Dawley rats were randomly assigned to two groups of four rats each, sHDL and MiNano-12 (DPPC: DSPE2k = 1:2.09). All rats were fasted overnight before dosing and received different formulations at a dose of 136 μmol/kg based on lipids concentration via tail vein injection. Blood samples of approximately 0.3 mL were collected from the jugular vein in heparinized BD centrifuge tubes (BD, Franklin Lakes, NJ) at pre-dose and 0.25, 0.5, 1, 2, 4, 8, 24 and 48 h after dosing. Serum samples were separated immediately by centrifugation at 10,000 rpm for 10 minutes at 4°C and stored at -20°C until further analysis.

4.3.8. *Quantification of serum lipids*

The levels of serum phospholipids (PL), total cholesterol (TC), and unesterified or free cholesterol (FC) were determined by enzymatic analyses using commercially available kits (Wako Chemicals, Richmond, VA). Cholesterol ester levels (CE) were calculated as the difference between TC and FC levels at each time point. Briefly, serum samples were diluted with PBS (pH 7.4) for TC and FC detection, or with Milli Q water for PL detection. Defined amounts of standards or diluted samples were transferred to 96-well plates (50 μL, 60 μL and 20 μL for TC, FC and PL

98

analyses, respectively), and assay reagents were added per manufacturer's instructions. The UV absorbance at 600 nm was measured using a Synergy NEO HTS Multi-Mode Microplate Reader (Bio-Tek).

4.3.9. *Pharmacokinetics and pharmacodynamic analyses*

A non-compartmental analysis (NCA) was performed to derive basic pharmacokinetic parameters for phospholipid serum concentrations versus time profiles using Phoenix© WinNonlin® Version 7.3 (Pharsight Corporation, Mountain View, CA). Serum concentrations of phospholipids, total cholesterol, free cholesterol and cholesterol esters versus time were plotted. The pharmacokinetic parameters of phospholipids were calculated and the pharmacodynamic effect in each rat was determined as the area under the total effect curve (AUEC) from dosing time point to 48 hours after dosing. Secondary pharmacodynamic endpoints (maximal effect [Emax] and time to Emax [Tmax, E]) were also analyzed to compare pharmacodynamic effects. The coefficient of variation was calculated for each parameter.

4.3.10. *Cholesterol distribution among lipoproteins*

Distribution of mobilized cholesterol between VLDL, LDL and HDL lipoprotein fractions following nanoparticle administration and exchange of cholesterol between lipoprotein throughout the 48 h elimination process was monitored via lipoprotein analysis. Briefly, rat serum lipoproteins were separated by size using a Waters HPLC system equipped with a Superose 6, 10/300 GL column (GE Healthcare, Piscataway, NJ). Cholesterol distribution among VLDL, LDL, and HDL lipoprotein fractions was determined by post-column enzymatic reactions. Rat serum collected prior to nanoparticle dosing and 0.5, 4, 24, and 48 h post-injection was analyzed. Serum aliquots

(50 μL) were injected and eluted with a 154 mM sodium chloride/0.02% sodium azide solution at 0.8 mL/min. The post-column reaction was used to determine cholesterol concentration as described in our previous published work (172).

4.3.11. Anti-inflammation effect of sHDL and MiNano in vivo

The anti-inflammatory effects of sHDL and MiNano were compared in a murine endotoxemia model. 7 to 8 week old male C57BL/6 mice were purchased from Jackson Laboratories and randomly divided into four groups, containing 5 mice each: a) PBS, b) LPS, c) LPS and sHDL, and d) LPS and MiNano-12. In the first study, 0.05 mg/kg of LPS was mixed with either sHDL or MiNano-12 and dosed to mice by intraperitoneal (IP) injection. LPS alone and PBS injections were used as controls. In the second study, 0.05 mg/kg of LPS was dosed initially by intraperitoneal injection. Subsequently, different formulations were dosed at 27.2 μmol/kg (based on the phospholipids concentration) by tail vein injection. All blood samples were collected from the jugular vein in heparinized BD centrifuge tubes (Franklin Lakes, NJ) at 2 h after LPS dosing. Serum samples were separated immediately by centrifugation at 14,000 rpm for 10 min at 4°C and stored at -80°C until further analysis. The concentration of TNF-α in the serum were quantified using ELISA (Thermo Fisher Scientific, Waltham, MA) per manufacturer's instruction.

4.3.12. Bio-distribution and accumulation of particles in plaque area in mice

To monitor whether sHDL and MiNano particles could accumulate in the atheroma, ApoE-/- (knockout) mice were fed a high-fat high-cholesterol diet (21% fat, 34% sucrose, and 0.2% cholesterol; Harlan, T.D. 88137) for 6 weeks to develop atherosclerotic lesions. DiR fluorescent dye was incorporated into sHDL and MiNano for tracking. The final DiR concentration was 20

μg/ml. The accumulation of sHDL or MiNano in plaque was evaluated by intravenous administration of DiR-labelled particles at a DiR level of 100 μg/kg after 12-weeks of feeding. Aortas were isolated for imaging purposes at 72 h after dosing using an IVIS Spectrum Imaging System (Caliper, Fullerton, CA).

4.3.13. Anti-atherosclerotic efficacy study

Eight-week-old male ApoE knockout mice purchased from the Jackson Laboratories were fed a high-fat high-cholesterol diet (21% fat, 34% sucrose, and 0.2% cholesterol; Harlan, T.D. 88137) for 6 weeks to develop atherosclerotic lesions. Mice were then randomized into three groups and received an intravenous injection twice a week (Tuesday and Friday) of either sHDL or MiNano at a lipid dose of 136 μmol/kg or an equivalent volume (200 μl) of PBS as a control for another 6 weeks under the same feeding diet. At 72 h after the last treatment, the whole blood of mice was collected for serum clinical chemistry analysis, and the left ventricle of the heart was perfused with PBS, followed by a fixative solution (4% paraformaldehyde in PBS). The liver was collected and kept in formalin for histological evaluation. To quantify the extent of the atherosclerotic lesions in the aortic root, the atherosclerotic lesions in the aortic sinus region were examined at three locations, each separated by 80 μm. The largest plaque of the three valve leaflets was used for morphological analysis. The lipid-burden plaque areas at the aortic sinus were determined by Verhoeff's staining. The macrophage cells in plaques were stained using a galectin-3 antibody (Mac-2; SANTA CRUZ Biotechnology, Santa Cruz, CA). To compare the effect of different groups, the area of stained lipid and macrophage were calculated using Image J.

4.3.14. Analysis of serum clinical chemistry and liver histology

As described in section 4.3.13, whole blood of ApoE knockout mice was collected at 72 h after the last treatment and serum were separated by centrifuge at 14,000 rpm for 10 min. Serum triglyceride, alanine aminotransferase (ALT) activity, and aspartate aminotransferase (AST) activity were measured using kits (TR0100, MAK052, MAK055, Sigma-Aldrich, St. Louis, MO). Liver tissue was collected and fixed in 4% formalin after perfusion of the animals. Then the liver tissue was routinely processed and embedded in paraffin. 8 μm thick sections were cut and stained with hematoxylin and eosin (H&E) for histopathological examination. All sections were investigated using a light microscope.

4.3.15. Lipogenesis study in mice

Normal C57BL/6 mice were divided into three groups (5 animals per group), including a PBS control, sHDL and MiNano-12 group. sHDL or MiNano-12 was given at the lipid dose level of 136 μmol/kg through intravenous administration. At 24 hours post-injection, mice were euthanized by CO_2 inhalation. After perfusion using PBS, liver tissues were collected and kept at -80 °C. Total RNA was purified from the liver tissues with TRIzol Reagent (Life technologies. Corp.), followed by reverse transcription with a SuperScript III kit (Invitrogen). qPCR was carried out with iQ SYBR Green Supermix (Bio-Rad). Cholesterol biogenesis related gene expression including Srebp2 and Hmgcr was determined.

4.3.16. Statistical Analysis

For comparisons and analyses between two groups, the significance of differences between data points, calculated pharmacokinetic and pharmacodynamic parameters were determined by the

two-tailed unpaired Student's t-test. For comparisons among three groups or more, one-way ANOVA analysis was performed followed by Tukey's test. Data are presented as mean ± SEM. A p-value < 0.05 was considered statistically significant.

4.4. Results

4.4.1. Preparation and characterization of nanoparticles

We prepared the model sHDL nanoparticles using 22A and DPPC combined at a 1:2 w/w (1:7.15 mol/mol) ratio of peptide to lipid. This composition was based on the composition of ETC-642, a peptide-based sHDL that has been previously tested in clinical trials in dyslipidemic patients (127,166). The average diameter of sHDL was determined to be 9.2 ± 0.3 nm by dynamic light scattering (DLS) (**Table 4.1, Figure 4.1A**), similar to the reported sHDL size (172). To match the size of the nano-micelles (MiNano) with sHDL, we combined increasing amounts of pegylated phospholipid (DPSE-PEG2000) with DPPC. We then prepared six MiNano and their compositions and sizes are summarized in Table 4.1. The average particle size of the micelles decreased gradually with an increase in DSPE-PEG-2000 to DPPC ratio. We selected two micelles having a similar size to sHDL, 14 and 12 nm, and low polydisperse for further investigation and named them MiNano-14 and MiNano-12, respectively. We further characterized the nanoparticle morphology using transmission electron microscopy (TEM) (**Figure 4.1B**). In agreement with our DLS findings, the TEM images showed homogeneous size distribution for all three nanoparticles.

Table 4.1. *Characterization of sHDL and MiNano particles.*

Formulation (molar ratio)	Particle size (nm)	PDI
22A: DPPC (0.14:1)	9.2 ± 0.3	0.16 ± 0.09
DPPC: DSPE-PEG2k (1:0.0654)	699 ± 51	0.40 ± 0.01
DPPC: DSPE-PEG2k (1:0.131)	403 ± 4.4	0.34 ± 0.03
DPPC: DSPE-PEG2k (1:0.262)	30.9 ± 1.0	0.13 ± 0.01
DPPC: DSPE-PEG2k (1:0.523)	27.8 ± 2.3	0.18 ± 0.01
DPPC: DSPE-PEG2k (1:1.05)	14.2 ± 0.4	0.20 ± 0.01
DPPC: DSPE-PEG2k (1:2.09)	12.2 ± 0.2	0.12 ± 0.01
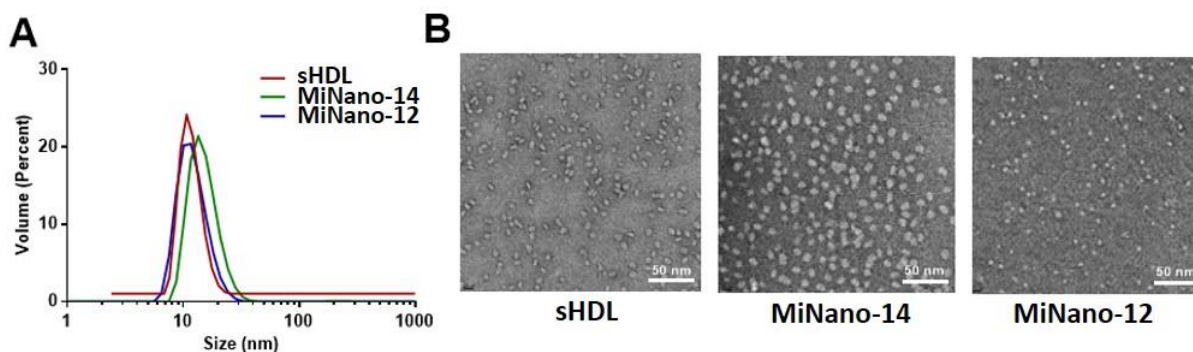
Figure 4.1. *Characterization of sHDL and MiNano. Particle size distribution determined by dynamic light scattering (A) and TEM (B).*

4.4.2. Cholesterol efflux capacity of sHDL and MiNano

Cholesterol filled macrophage-derived foam cells in the arterial wall are the hallmark of atherosclerosis. The removal of excess cholesterol from macrophage cells is important for the reverse cholesterol transport process and reduction of plaque area (236). We evaluated the ability of sHDL and MiNano to facilitate cholesterol efflux using RAW 264.7 macrophages. All

nanoparticles showed a significant ability to efflux cholesterol from the cellular membrane of macrophages (**Fig. 4.2A**). As the concentration of nanoparticles increased, the amount of effluxed cholesterol also increased and reached saturation at 70 to 80 µM lipid concentrations for all nanoparticles. At low concentrations, sHDL had a slightly higher cholesterol efflux capacity relative to the MiNano, while all three groups achieved a similar plateau at high concentrations. Taken together, the MiNano have similar cholesterol efflux ability *in vitro* compared to sHDL.
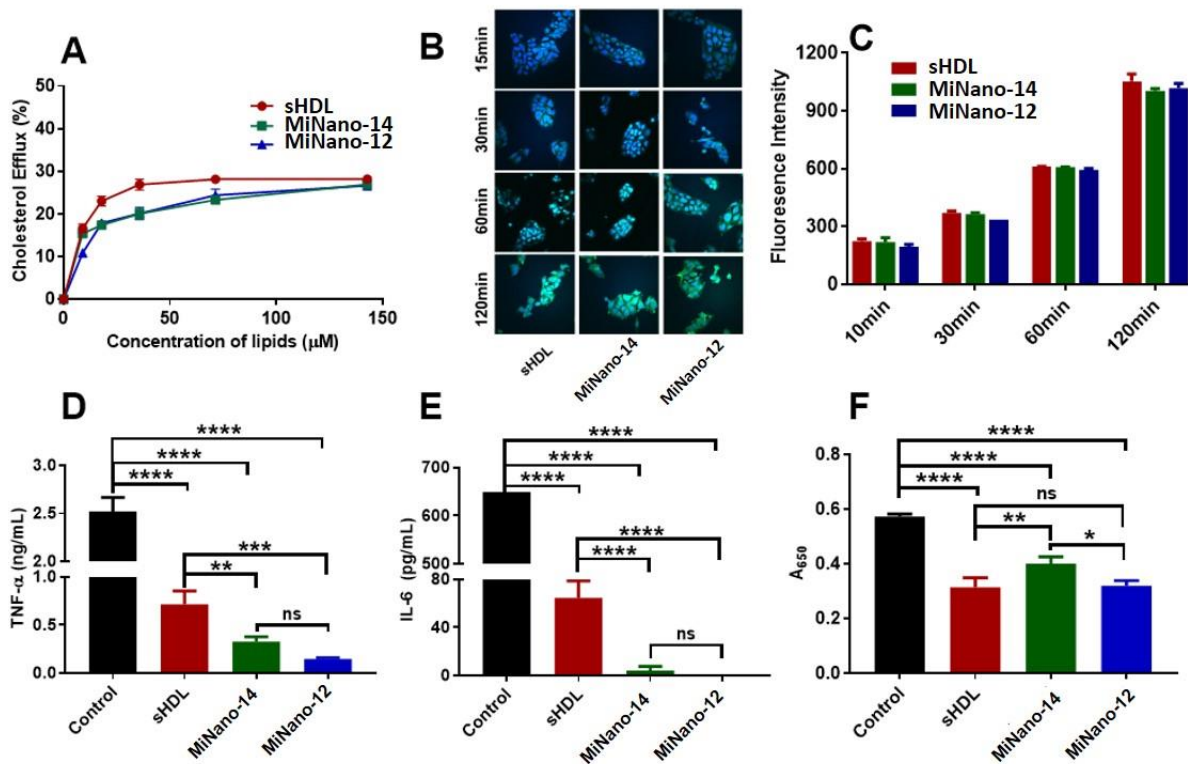
Figure 4.2. *Comparison of in vitro potency of MiNano and sHDL. Cholesterol efflux from RAW 264.7 macrophages (A). Cholesterol uptake kinetics by HepG2 cells following incubation with bodipy-labeled cholesterol-loaded sHDL or MiNano imaged with confocal microscopy (B) and quantified by flow cytometry (C). Panel B shows the channel overlay, with nuclei in blue and bodipy-cholesterol in green. Release of inflammatory cytokines TNF-α (D) and IL-6 (E) after incubation of sHDL or MiNano with RAW 264.7 macrophages for 16 h with pre-treatment of LPS. LPS-induced NF-kB activation in HEK-blue hTLR4 cells reduced by the addition of sHDL and MiNano (F). *P<0.05, **P<0.01, ***P<0.001, ****P<0.0001, ns: no significant difference.*

4.4.3. *Cholesterol uptake by liver cells in sHDL and MiNano*

After cholesterol is effluxed from peripheral tissues by sHDL, it is taken up by scavenger receptors on hepatocytes, metabolized and excreted into the bile (248). To evaluate cholesterol uptake by hepatocytes, sHDL and MiNano were loaded with bodipy-labeled cholesterol and incubated with HepG2 cells for various time intervals. The kinetics of cellular uptake of bodipy-cholesterol was visualized using confocal imaging and quantified by flow cytometry (**Figure. 4.2B-C**). The fluorescence of bodipy appeared to distribute throughout the cellular membranes and cytosol for all groups. When bodipy-cholesterol uptake by HepG2 cells was quantified using flow cytometry and compared among different formulations, there were no significant differences observed between the sHDL and MiNano. Thus, we conclude that similar to the delivery of cholesterol by sHDL, cholesterol can be taken up by hepatocytes when delivered by MiNano.

4.4.4. *In vitro anti-inflammation effect of sHDL and MiNano*

The anti-inflammatory properties of sHDL and MiNano were evaluated in RAW 264.7 macrophages. We induced an inflammatory response by the addition of endotoxin (LPS) to stimulate the release of pro-inflammation cytokines such as TNF-α and IL-6 (249). Either sHDL or MiNano was added to cell culture media and we determined cytokine levels to assess the abilities of the nanoparticles to inhibit the inflammatory response (**Figure 4.2D-E**). Both sHDL and MiNano showed a significant inhibitory effect on the secretion of TNF-α due to their abilities to physically bind and neutralize LPS and possibly disrupt toll-like receptor 4 (TLR4) recruitment by altering the lipid raft microenvironment through cholesterol efflux (250). Compared to sHDL,

the MiNano had a 4 to 14-fold higher cytokine release inhibitory effect. The difference between the effects of sHDL and MiNano is potentially due to differences in their LPS binding capacity.

Next, NF-κB activation was measured using HEK-Blue hTLR4 cells. As shown in **Figure 4.2F**, both sHDL and MiNano suppressed the activation of NF-κB by inhibiting LPS interaction with TLR-4. MiNano-12 exhibited similar activity to sHDL and appeared to be superior to MiNano-14 as measured by this assay.

4.4.5. *Pharmacokinetic characterization of sHDL and MiNano*

We selected MiNano-12 for further evaluation *in vivo* based on our *in vitro* results, showing that MiNano-12 exhibited a higher anti-inflammation efficacy and smaller particle size compared to other micelles analyzed. We compared the pharmacokinetics of sHDL and MiNano-12 and the nanoparticles' abilities to efflux cholesterol from the peripheral cells into the blood compartment in the Sprague Dawley rat. Both nanoparticles were administered at a 136 μM of phospholipids/kg dose by an intravenous bolus administration. This phospholipid dose was equivalent to a 50 mg/kg dose of apoA-I peptide, the typical dose used in preclinical models (153,172). We measured the serum concentrations of the phospholipid components of sHDL and MiNano-12 and evaluated the pharmacokinetic parameters (**Figure 4.3A, Table 4.2**).

The PK behavior of sHDL phospholipids was significantly different from that of MiNano-12. Though there was no significant difference between the peak concentration C_{max} of phospholipids in sHDL and MiNano-12, the peak time of MiNano-12 appeared much later than that of sHDL, at 8 h after administration. The later C_{max} for MiNano relative to sHDL may be due to differences in the biodistribution of the two nanoparticles (251). In addition, MiNano-12 had a longer lipid serum half-life *in vivo* with a value of 16 h compared to 1.7 h for sHDL. The AUC increased nearly 10-fold from 1063 mg*h/dL for sHDL to 10620 mg*h/dL for MiNano-12

resulting from the slower clearance. Thus, packaged in MiNano, phospholipids appear to have a longer residence time *in vivo*, which might result in the ability to efflux and eliminate more cholesterol per injected dose.
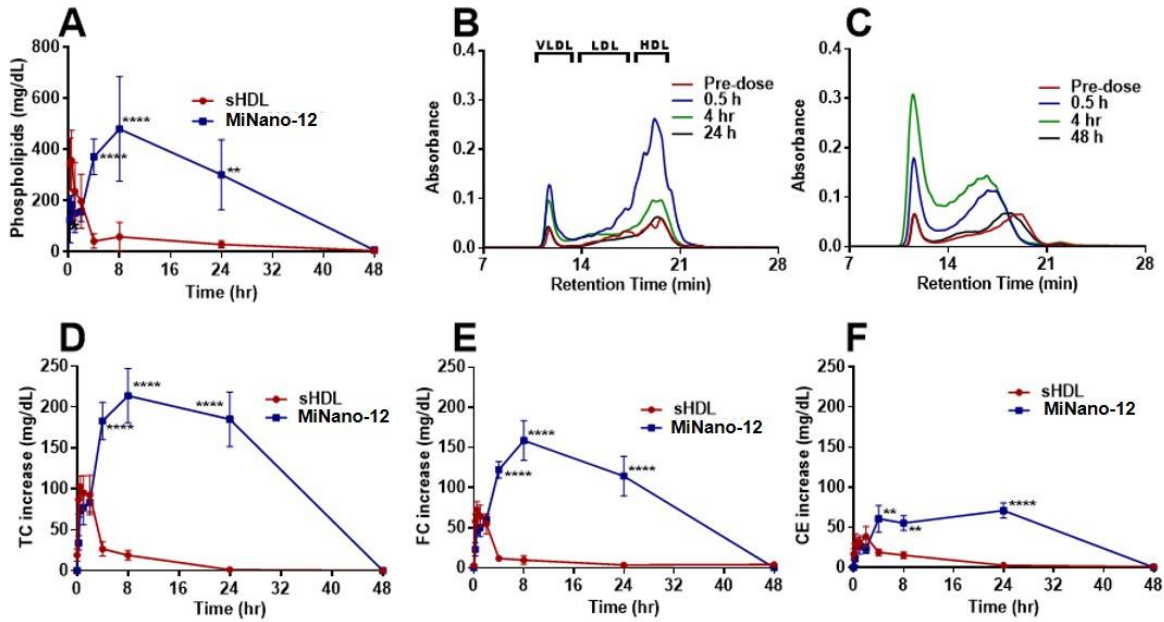
Figure 4.3. Comparison of sHDL and MiNano-12 pharmacokinetics and pharmacodynamics in the rat. Pharmacokinetics of phospholipids after IV bolus administration of 136 µmol/kg of sHDL or MiNano-12 in the Sprague Dawley rat. Changes in plasma lipids were measured by choline oxidase assay (A); Distribution of mobilized cholesterol among VLDL, LDL, and HDL lipoprotein fractions following administration of sHDL (B) and MiNano-12s (C). Mobilization of cholesterol from peripheral tissues into the blood compartment. The change in levels of total cholesterol (TC) (D), free cholesterol (FC) (E) and cholesterol ester (CE) (F) in rat serum were determined using commercially available kits. *P<0.05, **P<0.01, ***P<0.001, ****P<0.0001, ns: no significant difference.

Table 4.2. *Pharmacokinetic parameters (%CV) of phospholipids after administration of sHDL and MiNano-12.*

Parameter	Groups	
	sHDL	MiNano-12
$C_{max}{}^a$ (mg/dL)	383.9 (24.3)	481.8 (36.4)
$T_{max}{}^b$ (h)	0.38 (33.3)	8.0 (0.00) [****]
AUC^c (mg*h/dL)	1603 (26.0)	10620 (31.3) [**]
$K_{10}{}^d$ (h⁻¹)	0.4776 (41.8)	0.04885 (37.6) [**]
$T_{1/2}{}^e$ (h)	1.686 (34.7)	16.07 (32.1) [**]
CL^f (dL/h)	0.018 (26.9)	0.0027 (30.0) [***]
$V_{SS}{}^g$ (dL)	0.0404 (26.1)	0.0649 (51.8)

$^aC_{max}$: the maximum plasma concentration of peptide; ^bAUC: the area under the curve in a plot of concentration of peptide against time; $^cK_{10}$: elimination rate constant; $^dT_{1/2}$: the half-life of elimination; ^eCL: total clearance for peptide; $^fV_{ss}$: volume of distribution for peptide at steady state. Data were shown as mean with CV%. *P<0.05, **P<0.01, ***P<0.001, ****P<0.0001, ns: no significant difference compared with sHDL group.

4.4.6. *in vivo pharmacodynamics of sHDL and MiNano*

To examine the impact of increased circulation time of MiNano relative to sHDL on a pharmacological response, we determined the changes in cholesterol metabolism biomarkers following the administration of nanoparticles to normal SD rats by IV infusion. sHDL has been reported to facilitate cholesterol removal from peripheral tissues through RCT, thus, transient increase in serum cholesterol levels reflects cholesterol efflux induced by the administration of nanoparticles followed by its elimination by the liver. The levels of plasma total cholesterol (TC), free cholesterol (FC) and cholesterol ester (CE) were measured as shown in **Figure 4.3D-F**. Pharmacodynamic parameters were calculated and summarized in **Table 4.3**. The typical pharmacological response following sHDL infusion is the rapid mobilization of free cholesterol into the plasma compartment, followed by a rise in cholesterol ester due to esterification by lecithin-cholesterol acyltransferase (LCAT) and subsequent elimination of cholesterol by the liver.

These expected effects were observed for sHDL infusions with a maximum FC mobilization of 75 mg/dL at 0.5 h followed by a peak in CE (46 mg/dL) at 4 h, and elimination of all mobilized cholesterol by 24 h post-dosing. In line with the improvements in PK, MiNano-12 exhibited greater cholesterol mobilization and a longer pharmacodynamic effect relative to sHDL with a peak time of 7 h after infusion and maximum free cholesterol increase of 166 mg/dL. The area under the effect curve increased over 10-fold from 422 mg*h/dL (sHDL) to 4387 mg*h/dL (for MiNano-12). We observed a similar trend for the total cholesterol and cholesterol ester levels with significantly higher E_{max} and AUEC values for MiNano-12. However, cholesterol increase in both groups was transient, and the cholesterol levels returned back to baseline after 24 h for sHDL and 48 h for MiNano-12 along with the elimination. Hence, the longer lipid circulation time for MiNano-12 resulted in greater levels of mobilized cholesterol and a longer duration of the effect, which, in turn, should lead to a higher amount of cholesterol eliminated from the body and superior anti-atherosclerotic effect of MiNano relative to sHDL.

Table 4.3. *Pharmacodynamic parameters (%CV) of total cholesterol (TC), free cholesterol (FC) and cholesterol ester (CE) after administration of sHDL and MiNano-12.*

	Parameter	sHDL	MiNano-12
	$T_{max,E}{}^a$ (h)	0.75 (33.3)	6.0 (33.3)[**]
TC	$E_{max}{}^b$ (mg/dL)	114.9 (22.0)	237.9 (16.4)[**]
	$AUEC^c$ (mg*h/dL)	562.8 (22.4)	6607 (24.1)[***]
	$T_{max,E}$ (h)	0.56 (48.4)	7.0 (24.7)[***]
FC	E_{max} (mg/dL)	74.6 (23.2)	165.9 (20.5)[**]
	$AUEC$ (mg*h/dL)	421.7 (31.6)	4387 (28.9)[***]
	$T_{max,E}$ (h)	1.2 (68.8)	15 (60.7)[*]
CE	E_{max} (mg/dL)	46.4 (37.2)	84.7 (17.8)[*]
	$AUEC$ (mg*h/dL)	372.9 (18.6)	2220 (14.7)[****]

[a]T_{max}: time at which the E_{max} is observed. [b]E_{max}: the maximum plasma concentration of different cholesterol species. [c]AUEC: the area under the effect curve. Data were shown as mean CV%. *P<0.05, **P<0.01, ***P<0.001, ****P<0.0001, ns: no significant difference compared with sHDL group.

4.4.7. Distribution of mobilized cholesterol and lipoprotein remodeling in vivo

To investigate in greater detail the mechanism of cholesterol mobilization and elimination following administration of sHDL and MiNano, we determined the relative distribution of mobilized cholesterol in HDL, low-density lipoprotein (LDL), and very low-density lipoprotein (VLDL) fractions by HPLC. The positions of HDL, LDL, and VLDL sized particles containing cholesterol are labeled in **Figure 4.3B-C**. The infusion of sHDL caused a rapid mobilization of cholesterol in the HDL fraction, with the maximum increase at 0.5 h post-dose (blue line). The increase in HDL was accompanied by a small increase in VLDL, and cholesterol returned to baseline levels by 24 h post-dose. The cholesterol profile changes were different when MiNano-12 was administered. Because MiNano-12 is slightly larger in size than sHDL, the mobilized cholesterol appeared to elute between the HDL and LDL fractions at 0.5 and 4 h post-dose. The increase in VLDL appeared to be higher for MiNano-12 relative to sHDL. It is possible that DSPE-PEG caused inhibition of lipoprotein lipase or stimulation of liver lipogenesis, which both lead to the transient increase in VLDL. However, for both formulations, cholesterol increases were transient. The cholesterol level and its relative lipoprotein distribution returned to pre-dose levels, indicating completion of the RCT process triggered by administered sHDL and MiNano-12.

4.4.8. In vivo anti-inflammation effect of sHDL and MiNano

To further examine the functional similarities of MiNano and sHDL, we examined their abilities to inhibit inflammatory cytokine release in a mouse endotoxemia model. In clinical trials, co-administration of endotoxin mixed with sHDL in healthy subjects resulted in reduced inflammatory cytokine release, control of blood pressure and a marked decrease in the severity of clinical symptoms relative to the administration of endotoxin alone (144). To simulate this study,

we co-administered normal C57BL/6 mice with 0.05 mg/kg of LPS and either sHDL or MiNano-12. When mice were co-administered with sHDL or MiNano-12, significant suppression of TNF-α was observed (**Figure 4.4A**).

To simulate a more realistic scenario of infection-induced sepsis and nanoparticle treatment, we next dosed C57BL/6 mice with LPS by intraperitoneal injection, while sHDL and MiNano-12 were administered subsequently by IV bolus at a 27.2 µmol/kg dose as a rescue treatment. 2 h post-dose, we collected whole blood and isolated serum to quantify cytokines levels. Both sHDL and MiNano-12 exhibited notable inhibition of TNF-α and IL-6 (**Figure 4.4B**). Taken together, MiNano-12 exhibits anti-inflammatory functions of sHDL *in vivo*.
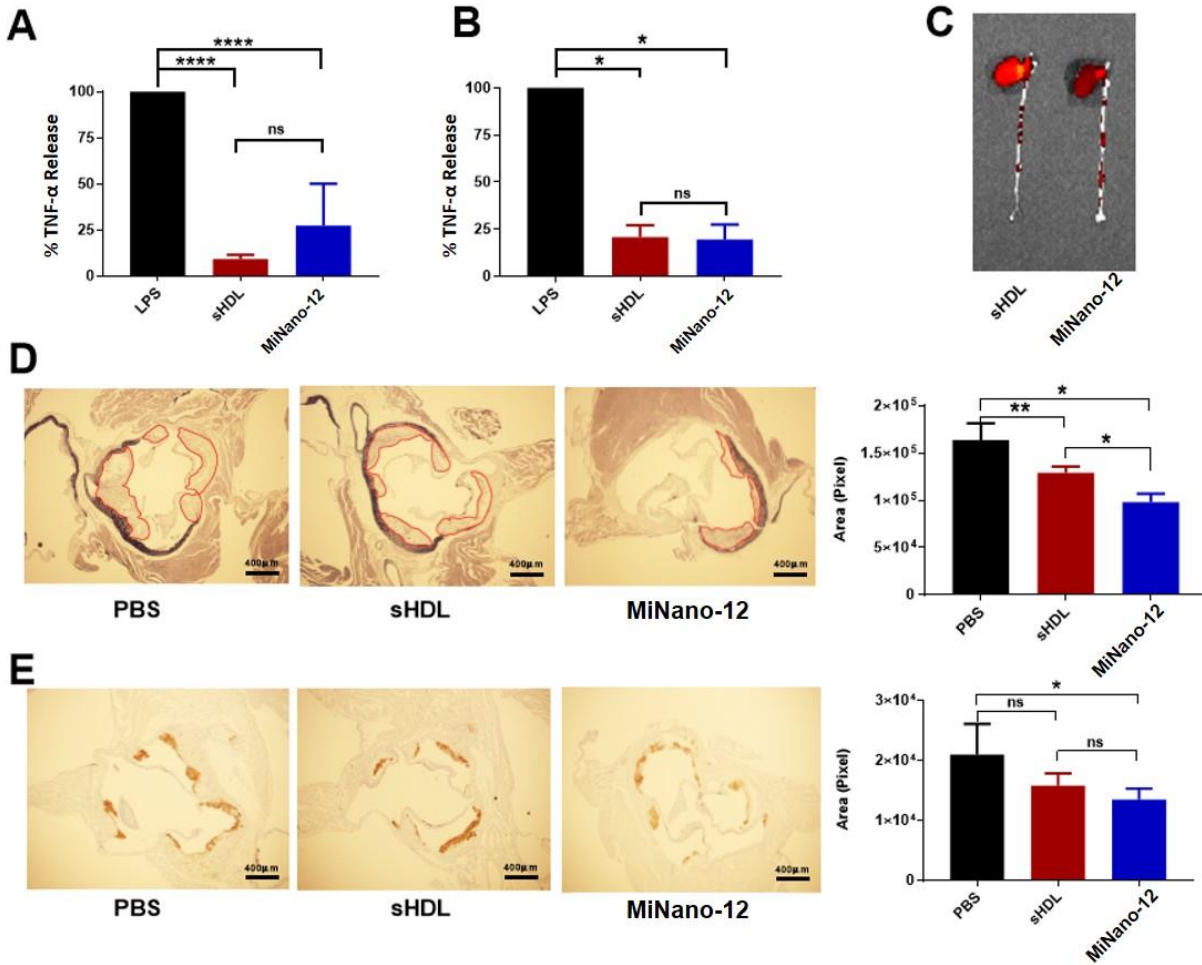
Figure 4.4. *Pharmacological effects of MiNano-12 and sHDL in murine models of inflammation and atherosclerosis. The serum concentration of TNF-α in C57BL/6 mice at 2 h after co-administration of sHDL or MiNano-12 (27.2 μmol/kg) with LPS (0.05 mg/kg) by IP route (A) and administration of LPS by IP followed by administration of sHDL or MiNano-12 by IV at the same doses (B). (n=5/group; *p<0.05, **p<0.01, ***p<0.001, ****p<0.0001, ns: no significant difference) Accumulation of DiR-labelled sHDL or MiNano-12 particles in plaque in ApoE-/- mice fed a high-fat diet for 12 weeks (C). Effect of sHDL and MiNano-12 on atherosclerosis regression in ApoE-/- mice. Aortas were dissected and plaque areas were visualized by Verhoeff's staining (D) and macrophages in aorta sections were visualized by Mac-2 stain (E). Representative lesion images and corresponding quantitative analyses of the aortic root cross-sections are shown. (n=12/group; *p<0.05, **p<0.01, ***p<0.001, ****p<0.0001, ns: no significant difference)*

4.4.9. Accumulation of sHDL and MiNano in atherosclerotic plaque

We examined the ability of MiNano and sHDL to accumulate in the atheroma of ApoE-/- mice that were fed a high-fat diet for 12 weeks to develop atherosclerosis. MiNano-12 and sHDL were fluorescently labeled by incorporation of DiR dye and dosed by intravenous administration at a 100 µg/kg DiR dose corresponding to a 136 µmole/kg lipid dose. At 72 h post-dose, the entire aorta was isolated for IVIS imaging (**Figure 4.4C**). Both sHDL and MiNano-12 successfully accumulated in the heart and plaque area, enabling the potential interaction between sHDL and MiNano-12 with macrophages for cholesterol efflux. The accumulation of both particles can last at least three days after administration due to the hydrophobicity of the particles and the specific distribution can potentially reduce the side effects caused by systemic treatment.

4.4.10. Anti-atherosclerosis efficacy of sHDL and MiNano

The ability of sHDL and MiNano to reduce the atherosclerotic burden was evaluated in ApoE-/- mice. ApoE-/- mice were placed on a high-fat diet for 6 weeks to develop atherosclerosis and were randomly divided into three groups for treatment with either PBS, sHDL or MiNano-12 for 6 weeks. We dosed the mice intravenously twice weekly at a dose level of 136 µmol/kg. Following the conclusion of treatment regimens, animals were euthanized and aortic roots were excised for plaque area analysis by Verhoeff's staining (**Figure 4.4D**) and Mac-2 macrophage staining (**Figure 4.4E**).

Compared to PBS control groups, the atheroma area was reduced significantly following the 6-week treatment of either sHDL or MiNano-12. There was a 21% reduction in plaque area following sHDL administration and a 40% reduction for MiNano-12 compared to the non-treatment group (**Figure. 4.4D**). MiNano-12 exhibited a greater anti-atherosclerotic potency in the

114

ApoE-/- murine model that is consistent with a higher efflux capacity *in vivo*. The Mac-2 staining signal represents the macrophages infiltration in the aorta root area, which is a biomarker for inflammation and plaque formation (252,253). sHDL treatment did not show a significant influence on the Mac-2 positive macrophage area, while the MiNano-12 group showed a 36% reduction of macrophage positive plaque burden compared to PBS control. By inhibiting the macrophage infiltration into the arterial wall, the induction of an early atherosclerotic lesion development can be prevented (254). Taken together, MiNano resulted in a significant reduction in atherosclerotic burden and prevented atherogenesis in a murine model of the disease.

4.4.11. Safety evaluation after treatment with sHDL and MiNano

We next studied the potential side effects and liver toxicity caused by sHDL or MiNano administration in ApoE-/- mice. H&E staining of liver tissues indicated no obvious damage to liver tissues when either sHDL or MiNano-12 were administered (**Figure 4.5A**). Plasma AST or ALT levels determined 72 h following the last dose were similar for all groups indicating no reduction in liver function (**Figure 4.5C-D**). In addition, plasma triglycerides levels were identical among the nanoparticle groups (**Figure 4.5E**). Then, we assessed the effect of sHDL or MiNano in C57BL/6 mice at a dose level of 136 μmol/kg (**Figure 4.5B**). At 24 h after intravenous administration of nanoparticles, cholesterol biosynthesis-related gene expression was examined. Srebp2 expression was not changed while Hmgcr expression in the liver was slightly down-regulated in the MiNano-12 group. The elevation of plasma AST, ALT and triglyceride levels are hallmarks of sHDL nanoparticle toxicity resulting from the need for the liver to metabolize large quantities of mobilized cholesterol. The sHDL used in ApoE-/- study was found to be safe in dyslipidemic patients at a similar dose level (~ 11.4 μmol/kg peptide) and safe in non-human

primates at 2-fold higher doses (43,255). Since no significant liver enzymes and triglyceride elevation had been observed for sHDL or MiNano-12 at the therapeutic dosage, we expect that MiNano-12 will have a comparable safety to that of sHDL in humans.
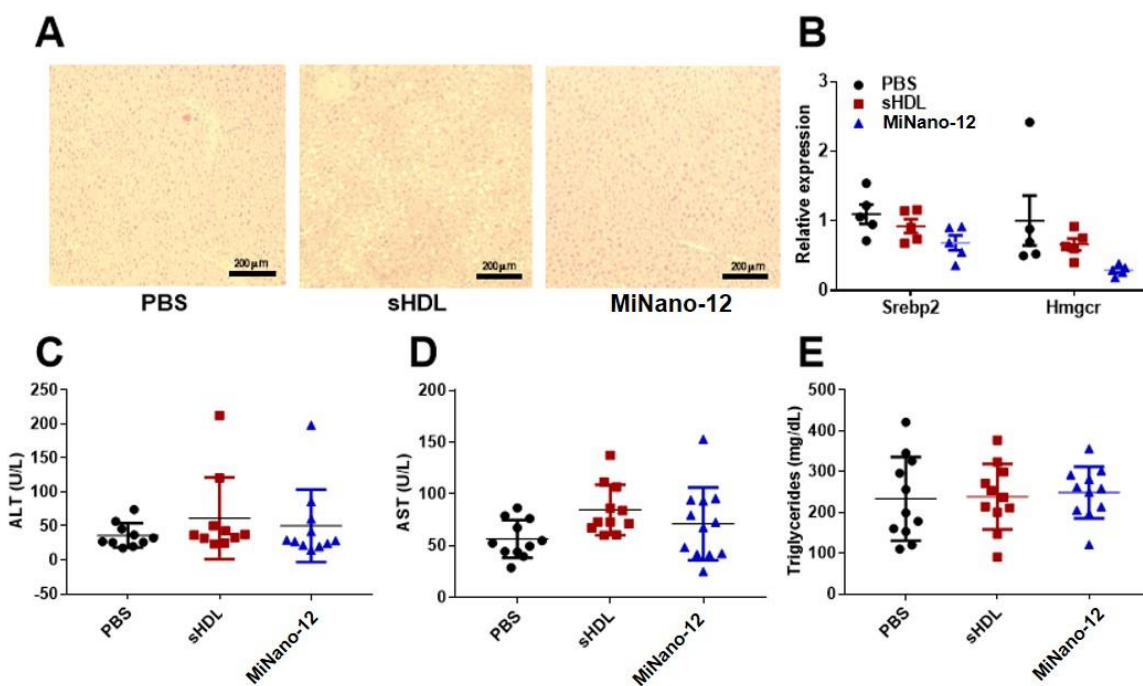
Figure 4.5. Safety comparison between sHDL and MiNano-12. H&E staining of liver tissues after a 6-week treatment of either PBS, sHDL or MiNano -12 in ApoE-/- mice (scale bar 300 µm) (A). The expression of genes involved in cholesterol biogenesis in the liver at 24 h after administration of sHDL or MiNano-12 at 136 µmol/kg in wildtype mice (B) (n= 5/group). The serum concentration of ALT (C), AST (D) and triglyceride (E) after a 6-week treatment with either PBS, sHDL, or MiNano-12s in ApoE-/- mice (n=12/group).

4.5. Discussion

In this study, we successfully established a MiNano system that mimics sHDL in structure and biological functions. The size of MiNano-12 was similar to sHDL, with a hydrophobic core and hydrophilic outer membrane, and exhibited similar cholesterol efflux capability (**Figure 4.2A**),

116

cellular uptake by liver cells (**Figure 4.2 B-C**), and anti-inflammation effect in macrophages (**Figure 4.2 D-F**) compare to sHDL. Despite the high similarity *in vitro*, the biological function of MiNano-12 was significantly different *in vivo*. MiNano-12 led to a greater extent of cholesterol mobilization and a longer duration of cholesterol elevation relative to sHDL (**Figure 4.3**) due to the longer circulation of MiNano-12 *in vivo*. In our therapeutic experiment, both sHDL and MiNano-12 achieved a significant reduction of plaque burden with a 6-week treatment of atheroma-bearing ApoE-/- mice. Surprisingly, MiNano-12 showed greater anti-atherosclerosis efficacy with a 40% atheroma area reduction compared to 21% for sHDL. Following a 6-week treatment, no histological changes in the liver or toxicities were observed, indicating the safeness of MiNano-12 at the therapeutic dosage (**Figure 4.5**). Thus, MiNano-12 appears to function just like sHDL *in vivo*, regardless of its simplicity, providing an easy manufacturing and economical alternative to sHDL, as MiNano can be prepared without the expensive recombinant apoA-I proteins or peptides.

Recently, there has been a major challenge in HDL therapeutics with cholesterol ester transfer protein (CETP) inhibitors in large phase III clinical trials (256,257). CETP inhibitors block cholesterol transfer from HDL to LDL, therefore, reducing the levels of LDL. and increasing the levels of HDL. Nevertheless, it only increased the circulating HDL cholesterol levels instead of increasing the functional HDL levels, which resulted in an accumulation of larger cholesterol-loaded HDLs that have limited capability for additional cholesterol efflux. In contrast, CVD patients administered with cholesterol-free sHDL have shown a rapid efflux of cholesterol from peripheral tissues with drastic reductions in atheroma volume (190,191,223). Furthermore, a 17,400-patient Phase 3 trial (AEGIS-II) is currently ongoing for an sHDL therapeutic to show a possible reduction of major adverse cardiovascular events in subjects with the acute coronary

syndrome (239). In addition, sHDL therapeutics have potential against other systemic inflammatory diseases such as sepsis, lupus and rheumatoid arthritis (144,258,259), therefore, we believe that MiNano may also have high potential beyond cardiovascular applications.

The potential of biomimetic HDL has been proposed from multiple investigations. For example, a biodegradable HDL-NP platform, synthesized with PLGA, cholesteryl oleate, a phospholipid with triphenylphosphonium, and apoA-I mimetic peptide 4F, was developed by Marrach *et al.* to detect vulnerable plaques by targeting the collapse of mitochondrial membrane potential that occurs during apoptosis (246). In addition, incorporation of quantum dots into a PLGA matrix allowed imaging purposes. Sanchez-Gaytan *et al.* developed a hybrid polymer/HDL nanoparticle composed of a lipid/apolipoprotein coating that encapsulates a PLGA core which elicited some key properties of endogenous HDL such as preferential uptake by macrophages and effective cholesterol efflux capacity (243). The presence of a PLGA core also enabled sustained release and atheroma targeting delivery, further showing the ability to accumulate in atherosclerotic plaques and co-localization with atheroma macrophages in an ApoE-/- mouse model. HDL nanoparticles with Au NP core-shell structure developed by Thaxton *et al.* showed a similar size and mimicked the general composition of endogenous HDL exhibiting physical binding of cholesterol and cellular cholesterol efflux *in vitro* (241,247). The design of such nanoparticles allowed the Au NP core to serve as a size- and shape-controlling scaffold for constructing an HDL-like particle by surface attachment of phospholipids and apoA-I. While such biomimetic HDL nanoparticles have demonstrated promising ability to target and accumulate in the atheroma with some local anti-inflammatory effects (10,144), to the best of our knowledge, none could reduce atheroma in diseases bearing animals and compare its efficacy directly with sHDL. Moreover, these nanoparticles displayed a larger particle size and density compared to

endogenous HDL which may alter the biodistribution, receptor interaction, and hepatic uptake of mobilized cholesterol.

While the tendency in the field to increase the complexity of nanomedicine designs grows, we approach to design simple HDL mimetic nano-micelle where this simplicity could reduce the manufacturing and the quality control labors, as well as the cost. MiNano involves only PC and PEG-PC which are approved excipients for parenteral administration. We also observed that the pegylation of PC significantly results in reduced size of nanoparticles reaching the target size of 12 nm with the capability to efflux cholesterol and exert anti-inflammatory activities. Therefore, we believe the manufacturing of MiNano can be established under quality scrutiny required for producing clinical-grade material. Similarly, we found several drugs with a simple design are currently in clinical trials against CVD and inflammatory disease. ETC-588, for example, is a type of blank liposome composed of naturally occurring phospholipids that upon infusion into humans would remain in the circulation to serve as a "sponge" for cholesterol and is able to show clinical efficacy in ischemia patients in Phase II trials (260). A phospholipid emulsion, GR270773, that was developed as a treatment against sepsis showed effective scavenger against the endotoxin, lipopolysaccharides (261). Moreover, sHDL showed promising results in binding to endotoxins and inhibiting inflammatory responses in humans while also rapidly regressing atheroma in CVD patients (144,192). As our simple structure of MiNano has shown to be effective in endotoxin neutralization and cholesterol mobilization compared to sHDL, we believe MiNano would likely serve as an exciting alternative to sHDL.

Chapter 5

Conclusion and Perspectives

The work presented in this thesis highlights the importance of the phospholipid composition of sHDL that has not been focused on previously. Many research studies and clinical trials of sHDL utilized proteins or peptides against both sepsis and atherosclerosis. Recent studies have acknowledged the importance of phospholipid composition, such as its role inducing intracellular signaling and receptor interactions (165). Therefore, we investigated how phospholipid composition can impact the biological functions of sHDL and further influence its therapeutic applications in various disease models including sepsis and atherosclerosis.

In chapter 2, we examined how phospholipid composition impacts the anti-inflammatory properties of sHDL with a goal to optimize nanoparticles for the treatment of sepsis. We selected phospholipids with various fatty acid chain lengths and saturations to formulate different fluidities of phospholipid phases on sHDL based on distinct phase transition temperatures of each phospholipid. The characteristics of each phospholipid led to sHDL forming into either a liquid crystalline phase or a gel phase. Among the different formulations of sHDL, we showed that the relatively stable and fluid phospholipid phase of 22A-DMPC elicited multi-faceted anti-inflammatory mechanisms including effectively suppressing NF-κB signaling and TLR4 signaling through regulation of TLR4 recruitment into lipid rafts and inducing ATF-3. Furthermore, single low-dose administration of sHDL remarkedly improved survival and reduced organ damage in mice treated with lethal doses of LPS. Here, we showed how altering phospholipid composition

could ultimately change the anti-inflammatory activities of sHDL. In the future, we would like to take further steps to validate biophysical characterization and further confirm the relationship between the fluidity of sHDL and LPS neutralization. We also found that the specific phospholipid composition of sHDL can affect the circulation half-life. In the future, it would be worthwhile to investigate mixtures of phospholipids to improve both anti-inflammatory activity and circulation half-life in order to maximize the therapeutic efficacy and to use more clinically relevant disease models such as CLP models. The CLP model causes polymicrobial infection via allowing the release of fecal material into the peritoneal cavity to induce exacerbated immune response which achieves the clinically relevant human condition. The CLP mice model, like in humans, is observed with the early hyperdynamic phases that progresses to the late hypodynamic phase along with a similar cytokine profile in human with sepsis.

In chapter 3, we systematically observed the effect of both peptide sequence and phospholipid composition in sHDL on the nanoparticle's ability to mobilize and esterify cholesterol *in vitro* and *in vivo*. We designed two sets of sHDL with either identical phospholipids and variable peptide sequences with different plasma stabilities or identical peptide sequences with variable fatty acid chain lengths and saturation. We observed that phospholipid composition rather than peptide composition in sHDL greatly influenced both the pharmacokinetic and pharmacodynamic profiles of the nanoparticle. Initially, we expected to observe an increase in circulation half-life and cholesterol mobilization with proteolytically stable 22A-P sHDL; however, increased circulation half-life did not translate to increased cholesterol mobilization *in vivo*. In contrast, 22A-DSPC sHDL greatly increased the circulation half-life and cholesterol mobilization compared to other phospholipids in sHDL. We further confirmed this finding through HDL remodeling experiments, which illustrated limited remodeling and interaction between 22A-DSPC

121

and endogenous HDL, leading to low protein insertion into the rigid gel phase of 22A-DSPC. We observed that a relatively fluid liquid crystalline phase sHDL undergoes rapid remodeling by endogenous HDL while rigid gel phase sHDL does not undergo remodeling. It is necessary to investigate whether more saturated and rigid phospholipid sHDL could lead to greater circulation half-life, cholesterol mobilization, and therapeutic effect in the animal models of atherosclerosis.

Finally, in chapter 4, we investigated an alternative therapeutic strategy with a novel nano-micelle called MiNano that could potentially mimic the biological functions of sHDL and reverse cholesterol transport, overcoming the limitation of apoA-I or recombinant apoA-I. We were able to formulate MiNano with structural and functional similarities to sHDL with a small particle size (12 – 14 nm) and a hydrophobic core and hydrophilic exterior. We validated their similar capabilities of reverse cholesterol transport and anti-inflammatory activities *in vitro*. Interestingly, *in vivo*, MiNano resulted in a significant improvement in circulation and cholesterol mobilization compared to sHDL. In therapeutic studies, MiNano led to 40% atheroma area reduction and marked inflammatory cytokine reductions in the atherosclerosis model and inflammatory model, respectively. Based on our previous findings that different phospholipid compositions could influence the biological function of sHDL, we believe MiNano can also be optimized for various disease models by altering the phospholipid composition of MiNano. For example, we could formulate MiNano with DMPC to increase the potential anti-inflammatory activities or with DSPC to increase the circulation half-life. In summary, we believe MiNano to be a potential treatment option for other inflammatory diseases such as sepsis, SLE, and rheumatoid arthritis.

In conclusion, the work of this thesis gives rise to new insights on the importance of the phospholipid composition of sHDL and its biomimetic MiNano. Different phospholipids can alter the biological function of sHDL, and we have verified that phospholipids critically impact the

pharmacokinetic and pharmacodynamic profiles of the nanoparticle. In addition, we have shown that, with phospholipids alone, we could synthesize a more cost-effective MiNano to mimic sHDL. We hope that the new insights provided in this thesis can further expand, benefit, and improve sHDL to be widely used in various disease indications.

Bibliography

1.   von Eckardstein, A., Nofer, J. R. & Assmann, G. High density lipoproteins and arteriosclerosis. Role of cholesterol efflux and reverse cholesterol transport. *Arterioscler. Thromb. Vasc. Biol.* **21**, 13–27 (2001).

2.   Pirillo, A., Catapano, A. L. & Norata, G. D. HDL in Infectious Diseases and Sepsis. in *Handbook of experimental pharmacology* **224**, 483–508 (Springer, Cham, 2015).

3.   Guo, L., Zheng, Z., Ai, J., Huang, B. & Li, X.-A. Hepatic scavenger receptor BI protects against polymicrobial-induced sepsis through promoting LPS clearance in mice. *J. Biol. Chem.* **289**, 14666–73 (2014).

4.   Zhu, X. *et al.* Macrophage ABCA1 reduces MyD88-dependent Toll-like receptor trafficking to lipid rafts by reduction of lipid raft cholesterol. *J. Lipid Res.* **51**, 3196–206 (2010).

5.   De Nardo, D. *et al.* High-density lipoprotein mediates anti-inflammatory reprogramming of macrophages via the transcriptional regulator ATF3. *Nat. Immunol.* **15**, 152–60 (2014).

6.   Wang, Y. *et al.* Effect of lipid-bound apolipoprotein A-I cysteine mutant on ATF3 in RAW264.7 cells. *Biosci. Rep.* **37**, BSR20160398 (2017).

7.   Smith, C. K. *et al.* Lupus high-density lipoprotein induces proinflammatory responses in macrophages by binding lectin-like oxidised low-density lipoprotein receptor 1 and failing to promote activating transcription factor 3 activity. *Ann. Rheum. Dis.* **76**, 602–611 (2017).

8.   Remaley, A. T., Amar, M. & Sviridov, D. HDL-replacement therapy: mechanism of action, types of agents and potential clinical indications. *Expert Rev. Cardiovasc. Ther.* **6**, 1203–15 (2008).

9.   Nofer, J.-R. *et al.* HDL and arteriosclerosis: beyond reverse cholesterol transport. *Atherosclerosis* **161**, 1–16 (2002).

10.   Barter, P. J. *et al.* Antiinflammatory properties of HDL. *Circ. Res.* **95**, 764–772 (2004).

11.   van Leeuwen, H. J. *et al.* Lipoprotein metabolism in patients with severe sepsis. *Crit. Care Med.* **31**, 1359–66 (2003).

12.   Chien, J.-Y., Jerng, J.-S., Yu, C.-J. & Yang, P.-C. Low serum level of high-density lipoprotein cholesterol is a poor prognostic factor for severe sepsis. *Crit. Care Med.* **33**,

1688–93 (2005).

13.   Tsai, M.-H. *et al.* Low serum concentration of apolipoprotein A-I is an indicator of poor prognosis in cirrhotic patients with severe sepsis. *J. Hepatol.* **50**, 906–15 (2009).

14.   Lilleby, V. *et al.* Body composition, lipid and lipoprotein levels in childhood-onset systemic lupus erythematosus. *Scand. J. Rheumatol.* **36**, 40–47 (2007).

15.   Soep, J. B., Mietus-Snyder, M., Malloy, M. J., Witztum, J. L. & Von Scheven, E. Assessment of atherosclerotic risk factors and endothelial function in children and young adults with pediatric-onset systemic lupus erythematosus. *Arthritis Care Res. (Hoboken).* (2004). doi:10.1002/art.20392

16.   Yuan, J., Li, L. I., Wang, Z., Song, W. & Zhang, Z. Dyslipidemia in patients with systemic lupus erythematosus: Association with disease activity and B-type natriuretic peptide levels. *Biomed. reports* **4**, 68–72 (2016).

17.   Gaal, K. *et al.* High-density lipopoprotein antioxidant capacity, subpopulation distribution and paraoxonase-1 activity in patients with systemic lupus erythematosus. *Lipids Health Dis.* **15**, 60 (2016).

18.   Toloza, S. M. A. *et al.* Systemic lupus erythematosus in a multiethnic US cohort (LUMINA): XXIII. Baseline predictors of vascular events. *Arthritis Rheum.* (2004). doi:10.1002/art.20622

19.   Gamal, S. M. *et al.* Immunological profile and dyslipidemia in Egyptian Systemic Lupus Erythematosus patients. *Egypt. Rheumatol.* (2017). doi:10.1016/j.ejr.2016.05.007

20.   Kontush, A. & Chapman, M. J. *High-Density Lipoproteins: Structure, Metabolism, Function and Therapeutics*. (John Wiley & Sons, 2012).

21.   Kontush, A. *et al.* Structure of HDL: particle subclasses and molecular components. *Handb. Exp. Pharmacol.* **224**, 3–51 (2015).

22.   Lund-Katz, S. & Phillips, M. C. High density lipoprotein structure-function and role in reverse cholesterol transport. *Subcell. Biochem.* **51**, 183–227 (2010).

23.   Segrest, J. P. Amphipathic helixes and plasma lipoproteins: thermodynamic and geometric considerations. *Chem. Phys. Lipids* **18**, 7–22 (1977).

24.   Tall, A. R., Small, D. M., Deckelbaum, R. J. & Shipley, G. G. Structure and thermodynamic properties of high density lipoprotein recombinants. *J. Biol. Chem.* **252**, 4701–11 (1977).

25.   Segrest, J. P. *et al.* Structure and function of apolipoprotein A-I and high-density lipoprotein. *Curr. Opin. Lipidol.* **11**, 105–15 (2000).

26.   Kontush, A., Lhomme, M. & Chapman, M. J. Unraveling the complexities of the HDL lipidome. *J. Lipid Res.* **54**, 2950–63 (2013).

27. Parks, J. S., Huggins, K. W., Gebre, A. K. & Burleson, E. R. Phosphatidylcholine fluidity and structure affect lecithin:cholesterol acyltransferase activity. *J. Lipid Res.* **41**, 546–53 (2000).

28. Sparks, D. L., Davidson, W. S., Lund-Katz, S. & Phillips, M. C. Effects of the neutral lipid content of high density lipoprotein on apolipoprotein A-I structure and particle stability. *J. Biol. Chem.* **270**, 26910–7 (1995).

29. Ma, C.-I. J. *et al.* Tweaking the cholesterol efflux capacity of reconstituted HDL. *Biochem. Cell Biol.* **90**, 636–45 (2012).

30. Marmillot, P., Patel, S. & Lakshman, M. R. Reverse cholesterol transport is regulated by varying fatty acyl chain saturation and sphingomyelin content in reconstituted high-density lipoproteins. *Metabolism.* **56**, 251–9 (2007).

31. Davidson, W. S. *et al.* The effect of high density lipoprotein phospholipid acyl chain composition on the efflux of cellular free cholesterol. *J. Biol. Chem.* **270**, 5882–90 (1995).

32. Rye, K. A., Hime, N. J. & Barter, P. J. The influence of sphingomyelin on the structure and function of reconstituted high density lipoproteins. *J. Biol. Chem.* **271**, 4243–50 (1996).

33. Rosenson, R. S. *et al.* HDL measures, particle heterogeneity, proposed nomenclature, and relation to atherosclerotic cardiovascular events. *Clin. Chem.* **57**, 392–410 (2011).

34. Matyus, S. P. *et al.* HDL particle number measured on the Vantera®, the first clinical NMR analyzer. *Clin. Biochem.* **48**, 148–155 (2015).

35. Silva, R. A. G. D. *et al.* Structure of apolipoprotein A-I in spherical high density lipoproteins of different sizes. *Proc. Natl. Acad. Sci. U. S. A.* **105**, 12176–81 (2008).

36. Calabresi, L., Gomaraschi, M., Rossoni, G. & Franceschini, G. Synthetic high density lipoproteins for the treatment of myocardial ischemia/reperfusion injury. *Pharmacol. Ther.* **111**, 836–54 (2006).

37. Ikonen, E. Cellular cholesterol trafficking and compartmentalization. *Nat. Rev. Mol. Cell Biol.* **9**, 125–138 (2008).

38. HDL Map Test® | Boston Heart Diagnostics. Available at: http://www.bostonheartdiagnostics.com/science_portfolio_map_test.php. (Accessed: 8th April 2016)

39. Oram, J. F., Lawn, R. M., Garvin, M. R. & Wade, D. P. ABCA1 is the cAMP-inducible apolipoprotein receptor that mediates cholesterol secretion from macrophages. *J Biol Chem* **275**, 34508–34511 (2000).

40. Wang, N., Lan, D., Chen, W., Matsuura, F. & Tall, A. R. ATP-binding cassette transporters G1 and G4 mediate cellular cholesterol efflux to high-density lipoproteins. *Proc Natl Acad Sci U S A* **101**, 9774–9779 (2004).

41.   Ji, Y. *et al.* Scavenger receptor BI promotes high density lipoprotein-mediated cellular cholesterol efflux. *J Biol Chem* **272**, 20982–20985 (1997).

42.   Rader, D. J. Regulation of reverse cholesterol transport and clinical implications. *Am. J. Cardiol.* **92**, 42J-49J (2003).

43.   Li, D., Gordon, S., Schwendeman, A. & Remaley, A. T. Apolipoprotein Mimetic Peptides for Stimulating Cholesterol Efflux. in *Apolipoprotein Mimetics in the Management of Human Disease* 29–42 (Springer International Publishing, 2015). doi:10.1007/978-3-319-17350-4_3

44.   Medzhitov, R. & Janeway, C. Innate immunity. *N. Engl. J. Med.* **343**, 338–44 (2000).

45.   Poltorak, A. *et al.* Defective LPS signaling in C3H/HeJ and C57BL/10ScCr mice: mutations in Tlr4 gene. *Science* **282**, 2085–8 (1998).

46.   Maeshima, N. & Fernandez, R. C. Recognition of lipid A variants by the TLR4-MD-2 receptor complex. *Front. Cell. Infect. Microbiol.* **3**, 3 (2013).

47.   Harris, H. W., Grunfeld, C., Feingold, K. R. & Rapp, J. H. Human very low density lipoproteins and chylomicrons can protect against endotoxin-induced death in mice. *J. Clin. Invest.* **86**, 696–702 (1990).

48.   Eggesbø, J. B., Lyberg, T., Aspelin, T., Hjermann, I. & Kierulf, P. Different binding of 125I-LPS to plasma proteins from persons with high or low HDL. *Scand. J. Clin. Lab. Invest.* **56**, 533–43 (1996).

49.   Rose, J. R. *et al.* Consequences of interaction of a lipophilic endotoxin antagonist with plasma lipoproteins. *Antimicrob. Agents Chemother.* **44**, 504–10 (2000).

50.   Roth, R. I., Levin, F. C. & Levin, J. Distribution of bacterial endotoxin in human and rabbit blood and effects of stroma-free hemoglobin. *Infect. Immun.* **61**, 3209–15 (1993).

51.   Wasan, K. M. *et al.* Lipoprotein distribution of a novel endotoxin antagonist, E5531, in plasma from human subjects with various lipid levels. *Antimicrob. Agents Chemother.* **43**, 2562–4 (1999).

52.   Grunfeld, C. *et al.* Lipoproteins inhibit macrophage activation by lipoteichoic acid. *J. Lipid Res.* **40**, 245–52 (1999).

53.   Emancipator, K., Csako, G. & Elin, R. J. In vitro inactivation of bacterial endotoxin by human lipoproteins and apolipoproteins. *Infect. Immun.* **60**, 596–601 (1992).

54.   Van Oosten, M. *et al.* Apolipoprotein E protects against bacterial lipopolysaccharide-induced lethality. A new therapeutic approach to treat gram-negative sepsis. *J. Biol. Chem.* **276**, 8820–4 (2001).

55.   Wurfel, M. M., Kunitake, S. T., Lichenstein, H., Kane, J. P. & Wright, S. D.

Lipopolysaccharide (LPS)-binding protein is carried on lipoproteins and acts as a cofactor in the neutralization of LPS. *J. Exp. Med.* **180**, 1025–35 (1994).

56.   Levels, J. H., Abraham, P. R., van den Ende, A. & van Deventer, S. J. Distribution and kinetics of lipoprotein-bound endotoxin. *Infect. Immun.* **69**, 2821–8 (2001).

57.   Ulevitch, R. J. & Johnston, A. R. The modification of biophysical and endotoxic properties of bacterial lipopolysaccharides by serum. *J. Clin. Invest.* **62**, 1313–24 (1978).

58.   Wurfel, M. M., Hailman, E. & Wright, S. D. Soluble CD14 acts as a shuttle in the neutralization of lipopolysaccharide (LPS) by LPS-binding protein and reconstituted high density lipoprotein. *J. Exp. Med.* **181**, 1743–54 (1995).

59.   Levine, D. M., Parker, T. S., Donnelly, T. M., Walsh, A. & Rubin, a L. In vivo protection against endotoxin by plasma high density lipoprotein. *Proc. Natl. Acad. Sci. U. S. A.* **90**, 12040–12044 (1993).

60.   Kitchens, R. L., Wolfbauer, G., Albers, J. J. & Munford, R. S. Plasma lipoproteins promote the release of bacterial lipopolysaccharide from the monocyte cell surface. *J. Biol. Chem.* **274**, 34116–22 (1999).

61.   Cai, L., Ji, A., de Beer, F. C., Tannock, L. R. & van der Westhuyzen, D. R. SR-BI protects against endotoxemia in mice through its roles in glucocorticoid production and hepatic clearance. *J. Clin. Invest.* **118**, 364–75 (2008).

62.   Guo, L. *et al.* Scavenger receptor BI protects against septic death through its role in modulating inflammatory response. *J. Biol. Chem.* **284**, 19826–34 (2009).

63.   Vishnyakova, T. G. *et al.* Binding and internalization of lipopolysaccharide by Cla-1, a human orthologue of rodent scavenger receptor B1. *J. Biol. Chem.* **278**, 22771–80 (2003).

64.   Guo, L. *et al.* High density lipoprotein protects against polymicrobe-induced sepsis in mice. *J. Biol. Chem.* **288**, 17947–53 (2013).

65.   Anderson, R. G. W. & Jacobson, K. A role for lipid shells in targeting proteins to caveolae, rafts, and other lipid domains. *Science* **296**, 1821–5 (2002).

66.   Anchisi, L., Dessì, S., Pani, A. & Mandas, A. Cholesterol homeostasis: a key to prevent or slow down neurodegeneration. *Front. Physiol.* **3**, 486 (2012).

67.   Triantafilou, M., Miyake, K., Golenbock, D. T. & Triantafilou, K. Mediators of innate immune recognition of bacteria concentrate in lipid rafts and facilitate lipopolysaccharide-induced cell activation. *J. Cell Sci.* **115**, 2603–11 (2002).

68.   Gilchrist, M. *et al.* Systems biology approaches identify ATF3 as a negative regulator of Toll-like receptor 4. *Nature* **441**, 173–178 (2006).

69.   Whitmore, M. M. *et al.* Negative regulation of TLR-signaling pathways by activating

transcription factor-3. *J. Immunol.* **179**, 3622–30 (2007).

70. Kwon, J.-W. *et al.* Activating transcription factor 3 represses inflammatory responses by binding to the p65 subunit of NF-κB. *Sci. Rep.* **5**, 14470 (2015).

71. Singer, M. *et al.* The Third International Consensus Definitions for Sepsis and Septic Shock (Sepsis-3). *JAMA* **315**, 801–810 (2016).

72. Kim, H. M. *et al.* Crystal structure of the TLR4-MD-2 complex with bound endotoxin antagonist Eritoran. *Cell* **130**, 906–17 (2007).

73. Visintin, A., Halmen, K. A., Latz, E., Monks, B. G. & Golenbock, D. T. Pharmacological inhibition of endotoxin responses is achieved by targeting the TLR4 coreceptor, MD-2. *J. Immunol.* **175**, 6465–72 (2005).

74. Angus, D. & Poll, T. Van Der. Severe sepsis and septic shock. *N. Engl. J. Med.* **369**, 840–51 (2013).

75. Martin, G. S., Mannino, D. M. & Moss, M. The effect of age on the development and outcome of adult sepsis. *Crit. Care Med.* **34**, 15–21 (2006).

76. Torio, C. M. & Andrews, R. M. National Inpatient Hospital Costs: The Most Expensive Conditions by Payer, 2011.

77. Adhikari, N. K. J., Fowler, R. A., Bhagwanjee, S. & Rubenfeld, G. D. Critical care and the global burden of critical illness in adults. *Lancet (London, England)* **376**, 1339–46 (2010).

78. Rezende, E. *et al.* Epidemiology of severe sepsis in the emergency department and difficulties in the initial assistance. *Clin. (São Paulo, Brazil)* **63**, 457–64 (2008).

79. Mayr, F. B. *et al.* Infection rate and acute organ dysfunction risk as explanations for racial differences in severe sepsis. *JAMA* **303**, 2495–503 (2010).

80. Cohen, J., Opal, S. & Calandra, T. Sepsis studies need new direction. *Lancet. Infect. Dis.* **12**, 503–5 (2012).

81. Hotchkiss, R. S. *et al.* Depletion of dendritic cells, but not macrophages, in patients with sepsis. *J. Immunol.* **168**, 2493–500 (2002).

82. Angus, D. C. *et al.* Epidemiology of severe sepsis in the United States: analysis of incidence, outcome, and associated costs of care. *Crit. Care Med.* **29**, 1303–1310 (2001).

83. Lagu, T. *et al.* Hospitalizations, costs, and outcomes of severe sepsis in the United States 2003 to 2007. *Crit. Care Med.* **40**, 754–61 (2012).

84. Ranieri, V. M. *et al.* Drotrecogin alfa (activated) in adults with septic shock. *N. Engl. J. Med.* **366**, 2055–64 (2012).

85. Vincent, J.-L. *et al.* International study of the prevalence and outcomes of infection in

intensive care units. *JAMA* **302**, 2323–9 (2009).

86. Opal, S. M. *et al.* Systemic host responses in severe sepsis analyzed by causative microorganism and treatment effects of drotrecogin alfa (activated). *Clin. Infect. Dis.* **37**, 50–8 (2003).

87. Fink, M. P. & Warren, H. S. Strategies to improve drug development for sepsis. *Nat. Rev. Drug Discov.* **13**, 741–58 (2014).

88. Wiersinga, W. J., Leopold, S. J., Cranendonk, D. R. & van der Poll, T. Host innate immune responses to sepsis. *Virulence* **5**, 36–44 (2014).

89. Schroder, K. & Tschopp, J. The inflammasomes. *Cell* **140**, 821–32 (2010).

90. Kawai, T. & Akira, S. The role of pattern-recognition receptors in innate immunity: update on Toll-like receptors. *Nat. Immunol.* **11**, 373–84 (2010).

91. Lamkanfi, M. Emerging inflammasome effector mechanisms. *Nat. Rev. Immunol.* **11**, 213–20 (2011).

92. Vogl, T. *et al.* Mrp8 and Mrp14 are endogenous activators of Toll-like receptor 4, promoting lethal, endotoxin-induced shock. *Nat. Med.* **13**, 1042–9 (2007).

93. Bianchi, M. E. DAMPs, PAMPs and alarmins: all we need to know about danger. *J. Leukoc. Biol.* **81**, 1–5 (2007).

94. Schumann, R. R. *et al.* Structure and function of lipopolysaccharide binding protein. *Science* **249**, 1429–31 (1990).

95. Wright, S. D., Ramos, R. A., Tobias, P. S., Ulevitch, R. J. & Mathison, J. C. CD14, a receptor for complexes of lipopolysaccharide (LPS) and LPS binding protein. *Science* **249**, 1431–3 (1990).

96. Lu, Y.-C., Yeh, W.-C. & Ohashi, P. S. LPS/TLR4 signal transduction pathway. *Cytokine* **42**, 145–51 (2008).

97. van der Poll, T. & Opal, S. M. Host-pathogen interactions in sepsis. *Lancet. Infect. Dis.* **8**, 32–43 (2008).

98. Russell, J. A. Management of sepsis. *N. Engl. J. Med.* **355**, 1699–713 (2006).

99. Braude, A. I., Ziegler, E. J., Douglas, H. & McCutchan, J. A. Antibody to cell wall glycolipid of Gram-negative bacteria: induction of immunity to bacteremia and endotoxemia. *J. Infect. Dis.* **136 Suppl**, S167-73 (1977).

100. Ziegler, E. J. *et al.* Treatment of gram-negative bacteremia and shock with human antiserum to a mutant Escherichia coli. *N. Engl. J. Med.* **307**, 1225–30 (1982).

101. McCloskey, R. V, Straube, R. C., Sanders, C., Smith, S. M. & Smith, C. R. Treatment of

septic shock with human monoclonal antibody HA-1A. A randomized, double-blind, placebo-controlled trial. CHESS Trial Study Group. *Ann. Intern. Med.* **121**, 1–5 (1994).

102. Cohen, J. Adjunctive therapy in sepsis: a critical analysis of the clinical trial programme. *Br. Med. Bull.* **55**, 212–25 (1999).

103. Warren, H. *et al.* Assessment of ability of murine and human anti-lipid A monoclonal antibodies to bind and neutralize lipopolysaccharide. *J. Exp. Med.* **177**, 89–97 (1993).

104. Van Amersfoort, E. S., Van Berkel, T. J. C. & Kuiper, J. Receptors, Mediators, and Mechanisms Involved in Bacterial Sepsis and Septic Shock. *Clin. Microbiol. Rev.* **16**, 379–414 (2003).

105. Mullarkey, M. *et al.* Inhibition of endotoxin response by e5564, a novel Toll-like receptor 4-directed endotoxin antagonist. *J. Pharmacol. Exp. Ther.* **304**, 1093–102 (2003).

106. Ii, M. *et al.* A novel cyclohexene derivative, ethyl (6R)-6-[N-(2-Chloro-4-fluorophenyl)sulfamoyl]cyclohex-1-ene-1-carboxylate (TAK-242), selectively inhibits toll-like receptor 4-mediated cytokine production through suppression of intracellular signaling. *Mol. Pharmacol.* **69**, 1288–95 (2006).

107. Panacek, E. A. *et al.* Efficacy and safety of the monoclonal anti-tumor necrosis factor antibody F(ab')2 fragment afelimomab in patients with severe sepsis and elevated interleukin-6 levels. *Crit. Care Med.* **32**, 2173–82 (2004).

108. Fisher, C. J. *et al.* Initial evaluation of human recombinant interleukin-1 receptor antagonist in the treatment of sepsis syndrome: a randomized, open-label, placebo-controlled multicenter trial. *Crit. Care Med.* **22**, 12–21 (1994).

109. Opal, S. M. *et al.* Confirmatory interleukin-1 receptor antagonist trial in severe sepsis: a phase III, randomized, double-blind, placebo-controlled, multicenter trial. The Interleukin-1 Receptor Antagonist Sepsis Investigator Group. *Crit. Care Med.* **25**, 1115–24 (1997).

110. Fisher, C. J. *et al.* Recombinant human interleukin 1 receptor antagonist in the treatment of patients with sepsis syndrome. Results from a randomized, double-blind, placebo-controlled trial. Phase III rhIL-1ra Sepsis Syndrome Study Group. *JAMA* **271**, 1836–43 (1994).

111. Bernard, G. R. *et al.* Efficacy and safety of recombinant human activated protein C for severe sepsis. *N. Engl. J. Med.* **344**, 699–709 (2001).

112. Abraham, E. *et al.* Drotrecogin alfa (activated) for adults with severe sepsis and a low risk of death. *N. Engl. J. Med.* **353**, 1332–41 (2005).

113. Nadel, S. *et al.* Drotrecogin alfa (activated) in children with severe sepsis: a multicentre phase III randomised controlled trial. *Lancet (London, England)* **369**, 836–43 (2007).

114. López, A. *et al.* Multiple-center, randomized, placebo-controlled, double-blind study of the nitric oxide synthase inhibitor 546C88: effect on survival in patients with septic shock. *Crit.*

Care Med. **32**, 21–30 (2004).

115. Dellinger, R. P. *et al.* Surviving sepsis campaign: international guidelines for management of severe sepsis and septic shock: 2012. *Crit. Care Med.* **41**, 580–637 (2013).

116. Alvarez, C. & Ramos, A. Lipids, lipoproteins, and apoproteins in serum during infection. *Clin. Chem.* **32**, 142–5 (1986).

117. Sammalkorpi, K., Valtonen, V., Kerttula, Y., Nikkilä, E. & Taskinen, M. R. Changes in serum lipoprotein pattern induced by acute infections. *Metabolism.* **37**, 859–65 (1988).

118. Khosla, S. N., Goyle, N. & Seth, R. K. Lipid profile in enteric fever. *J. Assoc. Physicians India* **39**, 260–2 (1991).

119. Feingold, K. R. *et al.* Effect of endotoxin on cholesterol biosynthesis and distribution in serum lipoproteins in Syrian hamsters. *J. Lipid Res.* **34**, 2147–58 (1993).

120. Gordon, B. R. *et al.* Low lipid concentrations in critical illness: implications for preventing and treating endotoxemia. *Crit. Care Med.* **24**, 584–9 (1996).

121. Cabana, V. G., Siegel, J. N. & Sabesin, S. M. Effects of the acute phase response on the concentration and density distribution of plasma lipids and apolipoproteins. *J. Lipid Res.* **30**, 39–49 (1989).

122. Menschikowski, M., Hagelgans, A. & Siegert, G. Secretory phospholipase A2 of group IIA: is it an offensive or a defensive player during atherosclerosis and other inflammatory diseases? *Prostaglandins Other Lipid Mediat.* **79**, 1–33 (2006).

123. Pruzanski, W., de Beer, F. C., de Beer, M. C., Stefanski, E. & Vadas, P. Serum amyloid A protein enhances the activity of secretory non-pancreatic phospholipase A2. *Biochem. J.* **309 (Pt 2**, 461–4 (1995).

124. Ettinger, W. H. *et al.* Cytokines decrease apolipoprotein accumulation in medium from Hep G2 cells. *Arterioscler. Thromb.* **14**, 8–13 (1994).

125. Barlage, S. *et al.* ApoE-containing high density lipoproteins and phospholipid transfer protein activity increase in patients with a systemic inflammatory response. *J. Lipid Res.* **42**, 281–90 (2001).

126. Navab, M. *et al.* Human apolipoprotein A-I and A-I mimetic peptides: potential for atherosclerosis reversal. *Curr. Opin. Lipidol.* **15**, 645–9 (2004).

127. Khan, M., Drake, S., Crockatt, J. & Dasseux, J. Single-dose intravenous infusion of ETC-642, a 22-Mer ApoA-I analogue and phospholipids complex, elevates HDL-C in atherosclerosis patients. *Circulation* **108**, 563–564 (2003).

128. Navab, M. *et al.* Apolipoprotein A-I mimetic peptides. *Arterioscler. Thromb. Vasc. Biol.* **25**, 1325–31 (2005).

129. Navab, M., Reddy, S. T., Van Lenten, B. J. & Fogelman, A. M. HDL and cardiovascular disease: atherogenic and atheroprotective mechanisms. *Nat. Rev. Cardiol.* **8**, 222–32 (2011).

130. Sethi, A. A. *et al.* Asymmetry in the lipid affinity of bihelical amphipathic peptides. A structural determinant for the specificity of ABCA1-dependent cholesterol efflux by peptides. *J. Biol. Chem.* **283**, 32273–82 (2008).

131. Amar, M. J. A. *et al.* 5A apolipoprotein mimetic peptide promotes cholesterol efflux and reduces atherosclerosis in mice. *J. Pharmacol. Exp. Ther.* **334**, 634–41 (2010).

132. Chen, X. *et al.* An apoA-I mimetic peptide increases LCAT activity in mice through increasing HDL concentration. *Int. J. Biol. Sci.* **5**, 489–99 (2009).

133. Van Lenten, B. J. *et al.* Influenza infection promotes macrophage traffic into arteries of mice that is prevented by D-4F, an apolipoprotein A-I mimetic peptide. *Circulation* **106**, 1127–1132 (2002).

134. Gupta, H. *et al.* Inhibition of lipopolysaccharide-induced inflammatory responses by an apolipoprotein AI mimetic peptide. *Circ. Res.* **97**, 236–243 (2005).

135. Di Bartolo, B. A. *et al.* The apolipoprotein A-I mimetic peptide ETC-642 exhibits anti-inflammatory properties that are comparable to high density lipoproteins. *Atherosclerosis* **217**, 395–400 (2011).

136. Bloedon, L. T. *et al.* Safety, pharmacokinetics, and pharmacodynamics of oral apoA-I mimetic peptide D-4F in high-risk cardiovascular patients. *J. Lipid Res.* **49**, 1344–52 (2008).

137. Watson, C. E. *et al.* Treatment of patients with cardiovascular disease with L-4F, an apo-A1 mimetic, did not improve select biomarkers of HDL function. *J. Lipid Res.* **52**, 361–73 (2011).

138. Kos Reports on Promising Data Presented at AHA: New Compound Reverse-D4F, a Novel Apo A-I Mimetic Peptide, May Reduce the Progression of Atherosclerosis. Available at: http://www.businesswire.com/news/home/20051114005406/en/Kos-Reports-Promising-Data-Presented-AHA-Compound#.VF0-H_nF9HV.

139. Wool, G. D., Reardon, C. A. & Getz, G. S. Apolipoprotein A-I mimetic peptide helix number and helix linker influence potentially anti-atherogenic properties. *J. Lipid Res.* **49**, 1268–83 (2008).

140. Bielicki, J. K. *et al.* A new HDL mimetic peptide that stimulates cellular cholesterol efflux with high efficiency greatly reduces atherosclerosis in mice. *J. Lipid Res.* **51**, 1496–503 (2010).

141. Jean-Louis Dasseux. Peptide/lipid complex formation by co-lyophilization. (2001).

142. Li, Y., Dong, J.-B. Bin & Wu, M.-P. P. Human ApoA-I overexpression diminishes LPS-induced systemic inflammation and multiple organ damage in mice. *Eur. J. Pharmacol.* **590**,

417–422 (2008).

143. Khovidhunkit, W. *et al.* Effects of infection and inflammation on lipid and lipoprotein metabolism: mechanisms and consequences to the host. *J. Lipid Res.* **45**, 1169–96 (2004).

144. Pajkrt, D. *et al.* Antiinflammatory effects of reconstituted high-density lipoprotein during human endotoxemia. *J. Exp. Med.* **184**, 1601–8 (1996).

145. Parker, T. S. *et al.* Reconstituted high-density lipoprotein neutralizes gram-negative bacterial lipopolysaccharides in human whole blood. *Infect. Immun.* **63**, 253–258 (1995).

146. Viswambharan, H. *et al.* Reconstituted high-density lipoprotein inhibits thrombin-induced endothelial tissue factor expression through inhibition of RhoA and stimulation of phosphatidylinositol 3-kinase but not Akt/endothelial nitric oxide synthase. *Circ. Res.* **94**, 918–25 (2004).

147. Pajkrt, D. *et al.* Differential effects of reconstituted high-density lipoprotein on coagulation, fibrinolysis and platelet activation during human endotoxemia. *Thromb. Haemost.* **77**, 303–7 (1997).

148. Nicholls, S. J. *et al.* Impact of short-term administration of high-density lipoproteins and atorvastatin on atherosclerosis in rabbits. *Arterioscler. Thromb. Vasc. Biol.* **25**, 2416–21 (2005).

149. McDonald, M. C. *et al.* Reconstituted high-density lipoprotein attenuates organ injury and adhesion molecule expression in a rodent model of endotoxic shock. *Shock* **20**, 551–7 (2003).

150. Cockerill, G. W. *et al.* High density lipoproteins reduce organ injury and organ dysfunction in a rat model of hemorrhagic shock. *FASEB J.* **15**, 1941–52 (2001).

151. Thiemermann, C. *et al.* High density lipoprotein (HDL) reduces renal ischemia/reperfusion injury. *J. Am. Soc. Nephrol.* **14**, 1833–43 (2003).

152. Calabresi, L. *et al.* High-density lipoproteins protect isolated rat hearts from ischemia-reperfusion injury by reducing cardiac tumor necrosis factor-alpha content and enhancing prostaglandin release. *Circ. Res.* **92**, 330–7 (2003).

153. Schwendeman, A. *et al.* The effect of phospholipid composition of reconstituted HDL on its cholesterol efflux and anti-inflammatory properties. *J. Lipid Res.* **56**, 1727–37 (2015).

154. Morin, E. E., Guo, L., Schwendeman, A. & Li, X. A. HDL in sepsis - risk factor and therapeutic approach. *Front. Pharmacol.* **6**, 1–9 (2015).

155. Dai, L. *et al.* The apolipoprotein A-I mimetic peptide 4F prevents defects in vascular function in endotoxemic rats. *J. Lipid Res.* **51**, 2695–705 (2010).

156. Zhang, Z. *et al.* Apolipoprotein A-I mimetic peptide treatment inhibits inflammatory

responses and improves survival in septic rats. *Am. J. Physiol. Heart Circ. Physiol.* **297**, H866–H873 (2009).

157.   Moreira, R. S. *et al.* Apolipoprotein A-I mimetic peptide 4F attenuates kidney injury, heart injury, and endothelial dysfunction in sepsis. *Am. J. Physiol. Regul. Integr. Comp. Physiol.* **307**, R514-24 (2014).

158.   Imai, T., Fujita, T. & Yamazaki, Y. Beneficial effects of apolipoprotein A-I on endotoxemia. *Surg. Today* **33**, 684–687 (2003).

159.   Yan, Y. jie, Li, Y., Lou, B. & Wu, M. ping. Beneficial effects of ApoA-I on LPS-induced acute lung injury and endotoxemia in mice. *Life Sci.* **79**, 210–215 (2006).

160.   Zhang, X., Wang, L. & Chen, B. Recombinant HDL (Milano) protects endotoxin-challenged rats from multiple organ injury and dysfunction. *Biol. Chem.* **396**, 53–60 (2015).

161.   Hubsch, A. P., Powell, F. S., Lerch, P. G. & Doran, J. E. A reconstituted, apolipoprotein A-I containing lipoprotein reduces tumor necrosis factor release and attenuates shock in endotoxemic rabbits. *Circ. Shock* **40**, 14–23 (1993).

162.   Quezado, Z. M. *et al.* Therapeutic trial of reconstituted human high-density lipoprotein in a canine model of gram-negative septic shock. *J. Pharmacol. Exp. Ther.* **272**, 604–11 (1995).

163.   AP, H., AT, C. & JE, D. Protective effects of reconstituted high-density lipoprotein in rabbit gram-negative bacteremia models. *J. Lab. Clin. Med.* **126**, 548–558 (1995).

164.   Casas, A. T., Hubsch, A. P., Rogers, B. C. & Doran, J. E. Reconstituted high-density lipoprotein reduces LPS-stimulated TNF alpha. *J. Surg. Res.* **59**, 544–52 (1995).

165.   Darabi, M., Guillas-Baudouin, I., Le Goff, W., Chapman, M. J. & Kontush, A. Therapeutic applications of reconstituted HDL: When structure meets function. *Pharmacol. Ther.* **157**, 28–42 (2016).

166.   Miles, J. *et al.* P105 Single-dose Tolerability, Pharmacokinetics, and Cholesterol Mobilization in Hdl-c Fraction Following Intravenous Administration of Etc-642, a 22-mer Apoa-i Analogue and Phospholipids Complex, in Atherosclerosis Patients. *Arterioscler. Thromb. Vasc. Biol. J. Am. Hear. Assoc.* **24**, e-19 (2004).

167.   Thoolen, B. *et al.* Proliferative and Nonproliferative Lesions of the Rat and Mouse Hepatobiliary System. *Toxicol. Pathol.* **38**, 5S-81S (2010).

168.   Giebeler, A. *et al.* Deficiency of Formyl Peptide Receptor 1 and 2 Is Associated with Increased Inflammation and Enhanced Liver Injury after LPS-Stimulation. *PLoS One* **9**, e100522 (2014).

169.   Hamesch, K., Borkham-Kamphorst, E., Strnad, P. & Weiskirchen, R. Lipopolysaccharide-induced inflammatory liver injury in mice. *Lab. Anim.* **49**, 37–46 (2015).

170. de Souza Xavier Costa, N. *et al.* Early and late pulmonary effects of nebulized LPS in mice: An acute lung injury model. *PLoS One* **12**, e0185474 (2017).

171. Kim, Y.-H., Yoon, D.-W., Kim, J.-H., Lee, J.-H. & Lim, C.-H. Effect of remote ischemic post-conditioning on systemic inflammatory response and survival rate in lipopolysaccharide-induced systemic inflammation model. *J. Inflamm.* **11**, 16 (2014).

172. Tang, J. *et al.* Influence of route of administration and lipidation of apolipoprotein A-I peptide on pharmacokinetics and cholesterol mobilization. *J. Lipid Res.* **58**, 124–136 (2016).

173. Li, D. *et al.* Effect of Synthetic High Density Lipoproteins Modification with Polyethylene Glycol on Pharmacokinetics and Pharmacodynamics. *Mol. Pharm.* **15**, 83–96 (2018).

174. Boulgaropoulos, B., Arsov, Z., Laggner, P. & Pabst, G. Stable and unstable lipid domains in ceramide-containing membranes. *Biophys. J.* **100**, 2160–8 (2011).

175. Rowe, E. S. Lipid chain length and temperature dependence of ethanol-phosphatidylcholine interactions. *Biochemistry* **22**, 3299–3305 (1983).

176. Whitmore, M. M. *et al.* Negative Regulation of TLR-Signaling Pathways by Activating Transcription Factor-3. *J. Immunol.* **179**, 3622–3630 (2007).

177. Gilchrist, M. *et al.* Systems biology approaches identify ATF3 as a negative regulator of Toll-like receptor 4. *Nature* **441**, 173–178 (2006).

178. Litman, B. J., Lewis, E. N. & Levin, I. W. Packing characteristics of highly unsaturated bilayer lipids: Raman spectroscopic studies of multilamellar phosphatidylcholine dispersions. *Biochemistry* **30**, 313–319 (1991).

179. Patel, H. *et al.* Characterization of apolipoprotein A-I peptide phospholipid interaction and its effect on HDL nanodisc assembly. *Int. J. Nanomedicine* **14**, 3069–3086 (2019).

180. Bonnefont-Rousselot, D. *et al.* Physicochemical changes in human high-density lipoproteins (HDL) oxidized by gamma radiolysis-generated oxyradicals. Effect on their cholesterol effluxing capacity. *Biochim. Biophys. Acta* **1255**, 23–30 (1995).

181. Girona, J., LaVille, A. E., Solà, R., Motta, C. & Masana, L. HDL derived from the different phases of conjugated diene formation reduces membrane fluidity and contributes to a decrease in free cholesterol efflux from human THP-1 macrophages. *Biochim. Biophys. Acta - Mol. Cell Biol. Lipids* **1633**, 143–148 (2003).

182. Ramstedt, B. & Slotte, J. P. Interaction of cholesterol with sphingomyelins and acyl-chain-matched phosphatidylcholines: a comparative study of the effect of the chain length. *Biophys. J.* **76**, 908–15 (1999).

183. Ohvo-Rekilä, H., Ramstedt, B., Leppimäki, P. & Peter Slotte, J. Cholesterol interactions with phospholipids in membranes. *Prog. Lipid Res.* **41**, 66–97 (2002).

184. Murphy, A. J. *et al.* High-Density Lipoprotein Reduces the Human Monocyte Inflammatory Response. *Arterioscler. Thromb. Vasc. Biol.* **28**, 2071–2077 (2008).

185. Zhu, X. *et al.* Increased cellular free cholesterol in macrophage-specific Abca1 knock-out mice enhances pro-inflammatory response of macrophages. *J. Biol. Chem.* **283**, 22930–22941 (2008).

186. Didichenko, S. A. *et al.* Enhanced HDL Functionality in Small HDL Species Produced Upon Remodeling of HDL by Reconstituted HDL, CSL112. *Circ. Res.* **119**, 751–763 (2016).

187. Fawaz, M. V. *et al.* Phospholipid component defines pharmacokinetic and pharmacodynamic properties of synthetic high-density lipoproteins. *J. Pharmacol. Exp. Ther.* **In press**, (2019).

188. Schwendeman, A. *et al.* The effect of phospholipid composition of reconstituted HDL on its cholesterol efflux and anti-inflammatory properties. *J. Lipid Res.* **56**, 1727–37 (2015).

189. Wang, Y., Zhu, X., Wu, G., Shen, L. & Chen, B. Effect of lipid-bound apoA-I cysteine mutants on lipopolysaccharide-induced endotoxemia in mice. *J. Lipid Res.* **49**, 1640–5 (2008).

190. Tardif, J.-C. *et al.* Effects of reconstituted high-density lipoprotein infusions on coronary atherosclerosis: a randomized controlled trial. *JAMA* **297**, 1675–82 (2007).

191. Nissen, S. E. *et al.* Effect of Recombinant ApoA-I Milano on Coronary Atherosclerosis in Patients With Acute Coronary Syndromes. *JAMA* **290**, 2292 (2003).

192. Tricoci, P. *et al.* Infusion of Reconstituted High-Density Lipoprotein, CSL112, in Patients With Atherosclerosis: Safety and Pharmacokinetic Results From a Phase 2a Randomized Clinical Trial. *J. Am. Heart Assoc.* **4**, e002171 (2015).

193. Duffy, D. Identifier: NCT03473223, Study to Investigate CSL112 in Subjects With Acute Coronary Syndrome (AEGIS-II); March 21, 2018. (2018). Available at: https://clinicaltrials.gov/ct2/show/NCT03473223. (Accessed: 17th December 2018)

194. Nicholls, S. J. *et al.* Effect of Serial Infusions of CER-001, a Pre-β High-Density Lipoprotein Mimetic, on Coronary Atherosclerosis in Patients Following Acute Coronary Syndromes in the CER-001 Atherosclerosis Regression Acute Coronary Syndrome Trial. *JAMA Cardiol.* **3**, 815 (2018).

195. Andrews, J. *et al.* Effect of serial infusions of reconstituted high-density lipoprotein (CER-001) on coronary atherosclerosis: rationale and design of the CARAT study. *Cardiovasc. Diagn. Ther.* **7**, 45–51 (2017).

196. Sparks, D. L., Frank, P. G. & Neville, T. A. Effect of the surface lipid composition of reconstituted LPA-I on apolipoprotein A-I structure and lecithin: cholesterol acyltransferase activity. *Biochim. Biophys. Acta* **1390**, 160–72 (1998).

197. Bolin, D. J. & Jonas, A. Sphingomyelin inhibits the lecithin-cholesterol acyltransferase reaction with reconstituted high density lipoproteins by decreasing enzyme binding. *J. Biol. Chem.* **271**, 19152–8 (1996).

198. Navab, M. *et al.* D-4F and Statins Synergize to Render HDL Antiinflammatory in Mice and Monkeys and Cause Lesion Regression in Old Apolipoprotein E–Null Mice. *Arterioscler. Thromb. Vasc. Biol.* **25**, 1426–1432 (2005).

199. Dasseux, J.-L. *et al.* Apolipoprotein AI agonists and their use to treat dyslipidemic disorders. (1999).

200. Remaley, A. T. *et al.* Apolipoprotein Specificity for Lipid Efflux by the Human ABCAI Transporter. *Biochem. Biophys. Res. Commun.* **280**, 818–823 (2001).

201. Vecoli, C. *et al.* Apolipoprotein A-I mimetic peptide L-4F prevents myocardial and coronary dysfunction in diabetic mice. *J. Cell. Biochem.* **112**, 2616–2626 (2011).

202. Navab, M., Anantharamaiah, G., Reddy, S. T. & Fogelman, A. M. Apolipoprotein A-I mimetic peptides and their role in atherosclerosis prevention. *Nat. Clin. Pract. Cardiovasc. Med.* **3**, 540–547 (2006).

203. Assmann, G., Schmitz, G., Donath, N. & Lekim, D. Phosphatidylcholine Substrate Specificity of Lecithin: Cholesterol Acyltransferase. *Scand. J. Clin. Lab. Invest.* **38**, 16–20 (1978).

204. Subbaiah, P. V, Liu, M., Bolan, P. J. & Paltauf, F. Altered positional specificity of human plasma lecithin-cholesterol acyltransferase in the presence of sn-2 arachidonoyl phosphatidyl cholines. Mechanism of formation of saturated cholesteryl esters. *Biochim. Biophys. Acta* **1128**, 83–92 (1992).

205. Small, D. . *Handbook of lipid research. The Physical Chemistry.* (1986).

206. Parks, J. S. & Gebre, A. K. Long-chain polyunsaturated fatty acids in the sn-2 position of phosphatidylcholine decrease the stability of recombinant high density lipoprotein apolipoprotein A-I and the activation energy of the lecithin:cholesterol acyltransferase reaction. *J. Lipid Res.* **38**, 266–75 (1997).

207. Sreerama, N. & Woody, R. W. Estimation of Protein Secondary Structure from Circular Dichroism Spectra: Comparison of CONTIN, SELCON, and CDSSTR Methods with an Expanded Reference Set. *Anal. Biochem.* **287**, 252–260 (2000).

208. Reißer, S., Strandberg, E., Steinbrecher, T. & Ulrich, A. S. 3D Hydrophobic Moment Vectors as a Tool to Characterize the Surface Polarity of Amphiphilic Peptides. *Biophys. J.* **106**, 2385–2394 (2014).

209. Lomize, A. L., Lomize, M. A., Krolicki, S. R. & Pogozheva, I. D. Membranome: a database for proteome-wide analysis of single-pass membrane proteins. *Nucleic Acids Res.* **45**, D250–D255 (2017).

210. Lomize, M. A., Pogozheva, I. D., Joo, H., Mosberg, H. I. & Lomize, A. L. OPM database and PPM web server: resources for positioning of proteins in membranes. *Nucleic Acids Res.* **40**, D370–D376 (2012).

211. Remaley, A. T. *et al.* Synthetic amphipathic helical peptides promote lipid efflux from cells by an ABCA1-dependent and an ABCA1-independent pathway. *J. Lipid Res.* **44**, 828–36 (2003).

212. Homan, R., Esmaeil, N., Mendelsohn, L. & Kato, G. J. A fluorescence method to detect and quantitate sterol esterification by lecithin:cholesterol acyltransferase. *Anal. Biochem.* **441**, 80–86 (2013).

213. Wang, N., Lan, D., Chen, W., Matsuura, F. & Tall, A. R. ATP-binding cassette transporters G1 and G4 mediate cellular cholesterol efflux to high-density lipoproteins. *Proc. Natl. Acad. Sci.* **101**, 9774–9779 (2004).

214. Krieger, M. Charting the fate of the "good cholesterol": identification and characterization of the high-density lipoprotein receptor SR-BI. *Annu. Rev. Biochem.* **68**, 523–58 (1999).

215. Asztalos, B. F. *et al.* Role of LCAT in HDL remodeling: investigation of LCAT deficiency states. *J. Lipid Res.* **48**, 592–9 (2007).

216. Soutar, A. K. *et al.* Effect of the human plasma apolipoproteins and phosphatidylcholine acyl donor on the activity of lecithin: cholesterol acyltransferase. *Biochemistry* **14**, 3057–64 (1975).

217. Sorci-Thomas, M., Kearns, M. W. & Lee, J. P. Apolipoprotein A-I domains involved in lecithin-cholesterol acyltransferase activation. Structure:function relationships. *J. Biol. Chem.* **268**, 21403–9 (1993).

218. Anantharamaiah, G. M., Venkatachalapathi, Y. V, Brouillette, C. G. & Segrest, J. P. Use of synthetic peptide analogues to localize lecithin:cholesterol acyltransferase activating domain in apolipoprotein A-I. *Arterioscler. An Off. J. Am. Hear. Assoc. Inc.* **10**, 95–105 (1990).

219. Datta, G. *et al.* Effects of increasing hydrophobicity on the physical-chemical and biological properties of a class A amphipathic helical peptide. *J. Lipid Res.* **42**, 1096–104 (2001).

220. Dasseux, J. *et al.* Multimeric Apoa-I agonist compounds. (2004).

221. Xu, B., Gillard, B. K., Gotto, A. M., Rosales, C. & Pownall, H. J. ABCA1-Derived Nascent High-Density Lipoprotein–Apolipoprotein AI and Lipids Metabolically Segregate. *Arterioscler. Thromb. Vasc. Biol.* **37**, 2260–2270 (2017).

222. Didichenko, S. A. *et al.* Enhanced HDL Functionality in Small HDL Species Produced Upon Remodeling of HDL by Reconstituted HDL, CSL112. *Circ. Res.* **119**, 751–763 (2016).

223. Keyserling, C. H. *et al.* Abstract 15525: CER-001, a Synthetic HDL-Mimetic, Safely Mobilizes Cholesterol in Healthy Dyslipidemic Volunteers. *Circulation* **124**, (2011).

224. Tardy, C. *et al.* CER-001, a HDL-mimetic, stimulates the reverse lipid transport and atherosclerosis regression in high cholesterol diet-fed LDL-receptor deficient mice. *Atherosclerosis* **232**, 110–118 (2014).

225. Turner, S. *et al.* Measurement of Reverse Cholesterol Transport Pathways in Humans: In Vivo Rates of Free Cholesterol Efflux, Esterification, and Excretion. *J. Am. Heart Assoc.* **1**, e001826 (2012).

226. Ditiatkovski, M., Palsson, J., Chin-Dusting, J., Remaley, A. T. & Sviridov, D. Apolipoprotein A-I Mimetic Peptides: Discordance Between In Vitro and In Vivo Properties-Brief Report. *Arterioscler. Thromb. Vasc. Biol.* **37**, 1301–1306 (2017).

227. Heidenreich, P. A. *et al.* Forecasting The Future of Cardiovascular Disease in the United States: A Policy Statement From the American Heart Association. *Circulation* **123**, 933–944 (2011).

228. Moore, K. J., Sheedy, F. J. & Fisher, E. A. Macrophages in atherosclerosis: a dynamic balance. *Nat. Rev. Immunol.* **13**, 709–721 (2013).

229. van der Wal, A. C. & Becker, A. E. Atherosclerotic plaque rupture--pathologic basis of plaque stability and instability. *Cardiovasc. Res.* **41**, 334–44 (1999).

230. IBANEZ, B., VILAHUR, G. & BADIMON, J. J. Plaque progression and regression in atherothrombosis. *J. Thromb. Haemost.* **5**, 292–299 (2007).

231. Jamkhande, P. G. *et al.* Therapeutic approaches to drug targets in atherosclerosis. *Saudi Pharm. J.* **22**, 179–190 (2014).

232. Bittencourt, M. S. & Cerci, R. J. Statin effects on atherosclerotic plaques: regression or healing? *BMC Med.* **13**, (2015).

233. Kingwell, B. A., Chapman, M. J., Kontush, A. & Miller, N. E. HDL-targeted therapies: progress, failures and future. *Nat. Rev. Drug Discov.* **13**, 445–464 (2014).

234. Lewis, G. F. & Rader, D. J. New Insights Into the Regulation of HDL Metabolism and Reverse Cholesterol Transport. *Circ. Res.* **96**, 1221–1232 (2005).

235. Phillips, M. C. Molecular Mechanisms of Cellular Cholesterol Efflux. *J. Biol. Chem.* **289**, 24020–24029 (2014).

236. Hutchins, P. M. & Heinecke, J. W. Cholesterol efflux capacity, macrophage reverse cholesterol transport and cardioprotective HDL. *Curr. Opin. Lipidol.* **26**, 388–393 (2015).

237. Gille, A. *et al.* CSL112 (Apolipoprotein A-I [Human]) Enhances Cholesterol Efflux Similarly in Healthy Individuals and Stable Atherosclerotic Disease Patients. *Arterioscler.*

Thromb. Vasc. Biol. **38**, 953–963 (2018).

238.	Tardif, J.-C. *et al.* Effects of the high-density lipoprotein mimetic agent CER-001 on coronary atherosclerosis in patients with acute coronary syndromes: a randomized trial. *Eur. Heart J.* **35**, 3277–3286 (2014).

239.	CSL Behring Advances to Phase 3 Cardiovascular Outcomes Trial for CSL112, its Novel Apolipoprotein A-I (Human) Infusion Therapy. (2018). Available at: http://markets.businessinsider.com/news/stocks/csl-behring-advances-to-phase-3-cardiovascular-outcomes-trial-for-csl112-its-novel-apolipoprotein-a-i-human-infusion-therapy-1002240360.

240.	Kotov, N. A. Inorganic Nanoparticles as Protein Mimics. *Science (80-.).* **330**, 188–189 (2010).

241.	Thaxton, C. S., Daniel, W. L., Giljohann, D. A., Thomas, A. D. & Mirkin, C. A. Templated Spherical High Density Lipoprotein Nanoparticles. *J. Am. Chem. Soc.* **131**, 1384–1385 (2009).

242.	Duivenvoorden, R. *et al.* A statin-loaded reconstituted high-density lipoprotein nanoparticle inhibits atherosclerotic plaque inflammation. *Nat. Commun.* **5**, (2014).

243.	Sanchez-Gaytan, B. L. *et al.* HDL-Mimetic PLGA Nanoparticle To Target Atherosclerosis Plaque Macrophages. *Bioconjug. Chem.* **26**, 443–451 (2015).

244.	McMahon, K. M. *et al.* Biomimetic High Density Lipoprotein Nanoparticles For Nucleic Acid Delivery. *Nano Lett.* **11**, 1208–1214 (2011).

245.	Luthi, A. J. *et al.* Tailoring of biomimetic high-density lipoprotein nanostructures changes cholesterol binding and efflux. *ACS Nano* **6**, 276–285 (2012).

246.	Marrache, S. & Dhar, S. Biodegradable synthetic high-density lipoprotein nanoparticles for atherosclerosis. *Proc. Natl. Acad. Sci.* **110**, 9445–9450 (2013).

247.	Luthi, A. J. *et al.* Robust passive and active efflux of cellular cholesterol to a designer functional mimic of high density lipoprotein. *J. Lipid Res.* **56**, 972–985 (2015).

248.	Linsel-Nitschke, P. & Tall, A. R. HDL as a target in the treatment of atherosclerotic cardiovascular disease. *Nat. Rev. Drug Discov.* **4**, 193–205 (2005).

249.	Tessaro, F. H. G., Ayala, T. S., Nolasco, E. L., Bella, L. M. & Martins, J. O. Insulin Influences LPS-Induced TNF-alpha and IL-6 Release Through Distinct Pathways in Mouse Macrophages from Different Compartments. *Cell Physiol Biochem* **42**, 2093–2104 (2017).

250.	Wang, S.-H., Yuan, S.-G., Peng, D.-Q. & Zhao, S.-P. High-density lipoprotein affects antigen presentation by interfering with lipid raft: a promising anti-atherogenic strategy. *Clin. Exp. Immunol.* **160**, 137–142 (2010).

251. Kudgus, R. A. *et al.* Tuning pharmacokinetics and biodistribution of a targeted drug delivery system through incorporation of a passive targeting component. *Sci. Rep.* **4**, (2014).

252. Li, Q. *et al.* Regulation of Macrophage Apoptosis and Atherosclerosis by Lipid-Induced PKCdelta Isoform Activation. *Circ. Res.* **121**, 1153–1167 (2017).

253. Menu, P. *et al.* Atherosclerosis in ApoE-deficient mice progresses independently of the NLRP3 inflammasome. *Cell Death Dis.* **2**, e137–e137 (2011).

254. Ye, D. *et al.* The Dynamics of Macrophage Infiltration into the Arterial Wall during Atherosclerotic Lesion Development in Low-Density Lipoprotein Receptor Knockout Mice. *Am. J. Pathol.* **178**, 413–422 (2011).

255. Jean-Louis Dasseux, Anna Shenderova Schwendeman & Zhu, L. Apolipoprotein A-I mimics. (2013).

256. Kosmas, C. E., DeJesus, E., Rosario, D. & Vittorio, T. J. *CETP Inhibition: Past Failures and Future Hopes*. **10**, 37–42 (Libertas Academica Ltd., 2016).

257. Tall, A. R. & Rader, D. J. Trials and Tribulations of CETP Inhibitors. *Circulation Research* **122**, 106–112 (2018).

258. McMahon, M. *et al.* Proinflammatory high-density lipoprotein as a biomarker for atherosclerosis in patients with systemic lupus erythematosus and rheumatoid arthritis. *Arthritis Rheum.* **54**, 2541–2549 (2006).

259. Wu, B. J. *et al.* Inhibition of arthritis in the Lewis rat by apolipoprotein A-I and reconstituted high-density lipoproteins. *Arterioscler. Thromb. Vasc. Biol.* **34**, 543–51 (2014).

260. Doggrell, S. A. ETC-588 (Pfizer). *Curr Opin Investig Drugs* **5**, 993–999 (2004).

261. Dellinger, R. P. *et al.* Efficacy and safety of a phospholipid emulsion (GR270773) in Gram-negative severe sepsis: results of a phase II multicenter, randomized, placebo-controlled, dose-finding clinical trial. *Crit Care Med* **37**, 2929–2938 (2009).